TOWARDS PHOTOACOUSTIC MAMMOGRAPHY

Aleksey Kharin

The research described in this thesis was carried out at the Biophysical Engineering Group, within the Faculty of Science and Technology of the University of Twente, Enschede, the Netherlands

The work was supported financially by the BioMedical Technology Institute (BMTI) of the University of Twente, and the European Commission through the projects OPTIMAMM (contract QLG1-CT-2000-00690; coordinator H. H. Rinneberg).

ISBN 90-365-2207-2

TOWARDS PHOTOACOUSTIC MAMMOGRAPHY

PROEFSCHRIFT

ter verkrijging van
de graad van doctor aan de Universiteit Twente,
op gezag van de rector magnificus,
prof. dr. W.H.M. Zijm,
volgens besluit van het College voor Promoties
in het openbaar te verdedigen
op donderdag 12 mei 2005 om 16.45 uur.

door

Aleksey Anatolievich Kharin
geboren op 28 mei 1976
te Archangelsk, Sovjet Unie

Dit proefschrift is goedgekeurd door:

prof. dr. A.G.J.M. van Leeuwen (de promotor) en
dr. ir. W. Steenbergen (de assistent promotor)

Summary

The enormous burden of breast cancer on society and the drawbacks of the existing mammography techniques are strong stimuli for the quest and development of new modalities for breast cancer detection.

Among alternative techniques for breast cancer detection, imaging modalities utilizing visible and near infrared light are of special interest. The reasons for this are the low cost of these techniques and the harmless nature of non-ionizing radiation. Besides, these techniques hold a potential for detection, localization, and diagnosis of cancer. The last feature is not shared by any other modality.

The poor spatial resolution resulting from high optical scattering of human soft tissue is the main drawback of optical imaging. This limits the range of application of these techniques.

This research deals with developing the photoacoustic imaging technique for breast cancer detection. Photoacoustics brings together the strong aspects of ultrasound and optical imaging. Medical imaging with photoacoustics is relatively new, and promising for a lot of applications, one of which is breast cancer detection.

Several steps undertaken in the development of the prototype of an instrument for breast cancer detection utilizing the photoacoustic (PA) effect are described in this thesis.

The introductory chapter 1 explains the motivation for this work. General information about the disease is presented. Chapter 1 also contains an overview of conventional techniques for breast cancer detection. Alternative techniques in development are also briefly presented. The second part of chapter 1 introduces the PA technique for medical imaging. Important aspects of this technique are considered. The chapter is concluded by the purpose of this work.

In chapter 2 a solid phantom based on the poly(vinyl alcohol) hydrogel, for PA technique laboratory testing is described. This is the only available rigid phantom mimicking both optical and acoustical properties of breast tissue.

The first part of chapter 3 contains the characterization of the ultrasound detector matrix to be used in the first clinical prototype of the PA mammograph (PAM) . The image resolution provided by this matrix in combination with the used image reconstruction algorithm used is presented. Based on the measured detector sensitivity the maximum achievable imaging depth is estimated. In the second part of chapter 3 the application of the wavelet transform for PA signal denoising is considered. Results of wavelet denoising of measured PA signals are presented and discussed.

Chapter 4 presents the first clinical PAM prototype that we have developed. Several design and mechanical aspects are described. The PAM prototype performance is presented for imaging optical absorption inhomogeneities inside the solid phantom and volunteer human tissue.

A comparison of two image reconstruction algorithms operating in the time and frequency domain is presented in chapter 5. The performances of both algorithms in the reconstruction of images from ideal and noisy simulated signals and measured signals are considered. Based on the results the frequency domain algorithm is favored for the image reconstruction in the PAM prototype.

The results and conclusions obtained from this work are summarized in chapter six. The purpose and outcome of the volunteer measurements are also presented. Finally some prospects for future work are given.

Contents

Chapter 1

Introduction

1.1 Motivation

Breast cancer is the second leading cause of cancer deaths in women (after lung cancer) and is worldwide the most common cancer among women. According to the American Cancer Society, over 190,000 new invasive cases of breast cancer are detected in the US each year, with approximately 40,000 resulting in death. In the Netherlands, in 1998, of the 32,000 invasive tumors discovered in females, 10,400 (i.e. 32.4 % of all cases), were cases involving breast cancer (Visser *et al.* , 2002). In 2000, these were 11,232 cases of breast cancer from 33,447 invasive cases (Visser *et al.* , 2003). According to the World Health Organization, worldwide more than 1.2 million people will be diagnosed with breast cancer this year. In the Netherlands, breast cancer dominates other cancers in females in all the 15-year age groups from 30 upwards: 30-44, 45-59, 60-74 and 75+ years. Based on the present incidence rates in the Netherlands, about 1 in 9 women would develop breast cancer; 1 in 22 dies from the disease. The Netherlands has among the highest rates of breast cancer in the world (only North America and Uruguay have a higher rate (Visser *et al.* , 2002)) and the highest in Europe.

It is well documented that early detection is the key to surviving breast cancer. Therefore, hospitals and health centers are focusing on the development and utilization of better technologies for early detection of breast cancer. Early detection implies uncovering the condition of the tumor before it reaches a metastatic state, in order to administer early treatments, that are less invasive and more effective.

1.1.1 Breast cancer

Cancer is a group of related diseases that begin in cells, the body's basic unit of life. The cancerous cell is a mutated cell which does not perform its original function anymore. Such a cell is self-sufficient in growth signals, and therefore keeps uncontrollably deviding.

As a result of uncontrolled dividing, in most types of cancer, cells form a lump or mass called a *tumor*, and are named after the part of body or type of cell where the tumor originated.

Breast cancer begins in breast tissue, which is made up of glands for milk production, called *lobules*, and the *ducts* that connect lobules to the nipple (see figure 1.1). The remainder of the breast is made up of fatty, connective and lymphatic tissue.

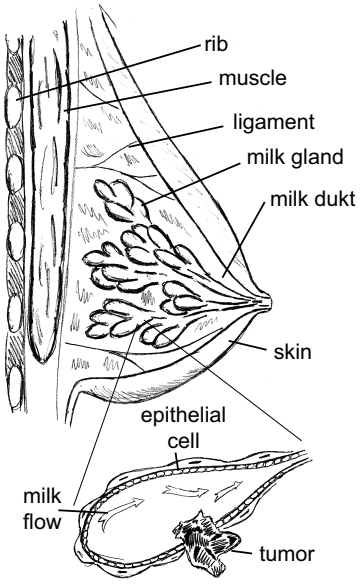

Figure 1.1: Female breast and most probable location of a benign cancer

Breast tumors can be classified in many different ways, based on what the pathologist sees under the microscope. Not all of the identifiable differences affect the way the tumor behaves - and therefore many of these features are not important to the patient treatment and to the future. There is one basic aspect that does make a difference whether the tumor is invasive or not.

With this criterion the breast tumors can be divided in three groups (ACS, 2004):

- *Benign* or noninvasive tumors. These are most types of tumors that occur in the breast. Although these tumors are abnormal, they do not uncontrollably grow or spread, and are not life-threatening.

- *In situ* tumors. These are cancerous tumors but are not yet spread beyond the area where they began. In situ breast cancer is confined in ducts or lobules.

- *Malignant* or invasive tumors. These are invasive and infiltrating breast tumors. These cancers start in the lobules or ducts of the

breast but have broken through the duct or gland walls to invade the surrounding fatty tissue of the breast.

Every breast cancer is different, but many follow a fairly standard course. How each is treated depends on how early it is discovered, how aggressively it is spreading and how it responds to hormone treatments and others drugs (ACS, 2004).

1.1.2 Angiogenesis

At some growing stage, almost all malignant tumors show the formation of new blood vessels. This property makes them, in principle, detectable. Let's consider a potentially cancerous cell. The cell has progressed through a series of mutations, become independent of growth signals from the body and capable of limitless replication. Are these neoplastic properties sufficient for such a cell to expand into a population that is symptomatic, or lethal? Current evidence argues that the answer may be "no" (Folkman, 2000). These neoplastic properties may only be necessary but not sufficient for the cancer cell to be lethal. In order to develop to a metastatic or a lethal phenotype, a tumor must first recruit and sustain its own private blood supply, a process called tumor *angiogenesis*.

Approximately 95% of all human cancers are carcinomas that originate as a microscopic *in situ* lesion which is not usually angiogenic at the outset. As was mentioned before (see paragraph 1.1.1) this is not yet a cancerous stage and the tumor can stay in this phase from months to years[1]. Switching to a malignant phenotype is discrete and is followed by neovascularization around the tumor site. Usually, only when neovascularization has been developed, the tumor break through the membrane separating different tissues, corrupting vessels and then growing and invading surrounding tissue using this extra blood supply. Tumors which are unable to induce angiogenesis remain dormant at a microscopic *in situ* size (Folkman, 2000).

Animal studies showed that the size limit for experimental tumors when angiogenesis was absent is between approximately 0.2 mm (Holmgren *et al.* , 1995) and 2 mm (Fang *et al.* , 2000) diameter. Most human breast tumors that are detected by, for example, a positive mammogram, have a size from 2-5 mm, and by that time angiogenesis has already occurred. Although no systematic study of angiogenesis on small breast lesions has been made, we

[1]May be it can stay even forever. Many oncologists believe that in situ tumors are not true cancer but an indicator of increased risk

may expect that the maximum size of malignant nonangiogenic tumors is not larger then 2 mm.

It is worth emphasizing that angiogenesis is not an absolute evidence for but a strong indication of malignancy of a tumor. In general, it can be detected by some of the techniques which are to be reviewed in the next section. For Doppler sonography, diaphanography, contrast-enhanced magnetic resonance imaging (MRI), and computerized tomography (CT), the visualization of a tumor depends essentially on the enhanced vascularity of the lesion. The nonangiogenic lesions are usually very difficult to detect unless they have microcalcifications which make them detectable by X-ray or when they are located on external surfaces such as skin or oral mucosa.

1.2 Breast imaging techniques

Breast imaging technologies are being developed with three distinct goals in mind: (1) to identify abnormal tissue, (2) to localize the abnormalities within the breast to facilitate further examination or treatment, and (3) to characterize the abnormalities. An ideal imaging modality would accomplish all three goals, but in reality most technologies cannot achieve this, so developers tend to focus on optimizing one goal at a time.

Imaging methods are used to map structural differences in tumors, such as microcalcifications, tissue masses, angiogenesis, asymmetry, and architectural distortion. Some recently developed techniques can provide information about the biological or functional differences between tumors and normal tissues.

The understanding of strengths and weaknesses of existing techniques helps to find ways either to improve existing methods or to develop a new technique for better cancer detection. In this section, the different imaging modalities (see table 1.1) are briefly described. Nowadays, only four of them are available and used routinely in the clinic.

1.2.1 X-ray mammography

In order to perform this test a breast is exposed to an X-ray beam whose transmission is measured (see figure 1.2). The breast is rather strongly compressed between an X-ray sensitive screen and a transparent plate. Purposes of compression are to: (1) obtain a uniform thickness, (2) reduce the total thickness in order to be able to operate in the range of lower photons energy but higher contrast between tissues (Kane, 2003), to get a clear image and

(3) reduce overlapping of the different inner breast tissues to increase clarity of the image.

X-ray mammography is the primary imaging modality for breast cancer screening and diagnosis. The technique was first pioneered by Warren (Warren, 1930) but it is being widely used only for the last 30 years.

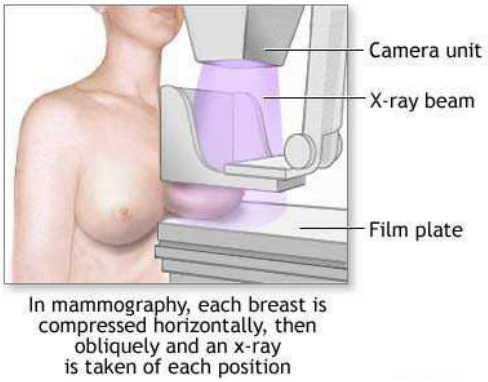

Figure 1.2: Taking of X-ray mammogram

The identification of a lesion relies on the imaging of radiographic density changes caused by the lesion and associated changes in breast architecture, vascularity or skin contour. Radiographically, benign lesions are usually less dense than those that are malignant, and in general they have smooth outlines whereas malignant lesions have irregular outlines. When the breast is glandular it is more difficult to image breast architecture than when the breast contains large amounts of fat. The breast might be so radiographically dense that breast structure cannot be imaged with sufficient clarity to identify a discrete mass. In the fatty breast the tumor may be clearly visible, as well as changes in vascularity and skin contour; the larger tumor in the dense breast can be seen less clearly but may be identifiable by small calcifications. *In vivo* radiographic studies on the incidence of calcifications show that they can be detected in 40-50% of malignant tumours and in about 20% of benign tumours, and histological sections show even higher percentages.

Several randomized controlled studies have been undertaken in four countries to assess the value of screening mammography (reviewed by Moss (Moss, 1999) and Jatoi (Jatoi, 1999)). Most of them demonstrated a clear benefit of screening mammography for women over age 50, but the results for women younger then age 50 are still controversial.

The sensitivity[2] of this technique has been quoted as between 83-95% (Sabel & Aichinger, 1996),(Mushlin *et al.* , 1998). The specificity[3] has been quoted as being between 90-98%(Mushlin *et al.* , 1998). However the positive predictive value (PPV) which includes the prevalence of the disease is quite

[2]ratio of correctly identified tumors to total number of investigated subjects with tumors

[3]ratio of correctly identified absence of tumor to total number of investigated subjects without tumor

poor. This is quoted as between 10-50% (Sabel & Aichinger, 1996).

Nowadays, the film-screen mammography (FSM) is being gradually replaced by full-field digital mammography (FFDM) which is identical except for the electronic detector that captures and facilitates display of the X-ray signals on a computer or laser-printed film. Although the resolution of the new FFDM instruments is not higher than the traditional FSM technique, additional data processing may help to find tumor marks with higher accuracy.

With all its advantages X-ray mammography does have some drawbacks. Notable among these are:

- the use of ionizing radiation with its associated potential carcinogenic risks, especially in the case of screening asymptomatic women;
- the high rate of false positives especially at the time directly after menopause when mamma glandular tissues have not completely disappeared. These can be seen on X-ray mammogram as regions of irregular size and shape;
- X-ray mammography also suffers from poor interpretation and reduced accuracy in the case of younger women or women with breasts possessing high amounts of radiodense glandular tissue.

1.2.2 Ultrasound imaging

Ultrasound imaging utilizes high-frequency sound waves which reflect at boundaries between tissue with different acoustic impedance, which is the product of sound velocity and material density. The time interval of arrival of these reflections is proportional to the depth of boundaries. Thus, ultrasound can map acoustic tissue boundaries. Traditionally it is used as an adjunct to X-ray mammography in the identification and differentiation of cysts or solid masses. Ultrasound imaging of the breast may also help radiologists to evaluate some lumps that can be felt but that are difficult to see on a X-ray mammogram, especially in dense breast.

Evaluation of the ultrasound technique in distinguishing malignant from benign tumors (Ziewacz *et al.* , 1999) has shown the accuracy of benign condition detection to be 99.5%. Another study (Duijm *et al.* , 1997) of ultrasonography combined with standard X-ray mammography found that such a combined use of techniques has a sensitivity of 92% and a specificity of 98%. Ultrasound could detect some earlier-stage, clinically occult tumors that were missed by screening mammography. Thus, there may be a future

role of ultrasound in the screening of younger women with dense breast and high risk factors. More study is needed to assess these possibilities.

1.2.3 Magnetic Resonance Imaging (MRI)

Magnetic resonance images are created by recording the signals generated after radiofrequency excitation of hydrogen nuclei (or other elements) in tissue exposed to a strong static magnetic field. The signals have characteristics that vary according to the tissue type (fat, muscle, fibrotic tissue, etc.) The method has minimal hazards from magnetic field effects and does not use ionizing radiation. The first MRI results of the human breast were disappointing, but subsequent use of an intravenous gadolinium based contrast agent offered a clear advance (Basset, 2000).

The sensitivity of contrast-enhanced MRI for the detection of suspicious lesions ranges between 88 and 100% (Helbich, 2000). However the specificity of the contrast-enhanced MRI has been quoted as rather variable, ranging from 37 to 100% (Helbich, 2000). This is mainly because of considerable exceptions and overlaps in contrast agent uptake and kinetics between benign and malignant tumors.

MR imaging of the breast is not recommended as a routine test for the differentiation of benign and malignant lesions. However, breast MRI can be used to assist in differential diagnosis of questionable lesions. MRI is also an expensive modality and the technique is not readily available for routine breast imaging.

1.2.4 Alternative techniques

The leading position of breast cancer incidence and the drawbacks of conventional mammography techniques are strong stimuli for efforts in pushing forward the current state of the art in detection and diagnosis and for the quest and development of new modalities that can address the limitation of the conventional breast cancer detection technologies. Table 1.1 summarizes conventional breast imaging technologies presented above and a number of new, most promising, techniques in the development stage (see table 1.1 “Alternative techniques”).

Technology	Description	Tumor contrast feature	Used routinely	Role suggested by preclinical data	Role suggested by clinical data	Relevant research references
Conventional techniques						
Film-screen X-ray mammography	Forms radiodensity map of the breast from intensity of transmitted X-ray beam measured using light/X-ray-sensitive film.	Microcalcification, radio-density changes	Screening, diagnosis			(Sabel & Aichinger, 1996),(Mushlin *et al.* , 1998)
Full-field digital X-ray mammography	Digital version of X-ray technique.	Microcalcification, radio-density changes	Screening, diagnosis			
Ultrasound	Forms images by reflection of megahertz frequency sound waves.	Acoustic impedance difference	Diagnosis	Screening		
Magnetic Resonance Imaging	Forms image using radio emission from nuclear spins.	Contrast agent uptake		Diagnosis	Screening	(Helbich, 2000)
Alternative techniques						
Scintimammography	Sense tumor from Gamma-ray emission of radioactive pharmaceutical.	Contrast agent uptake		Diagnosis	Screening	(Allen *et al.* , 1999), (Edel & Eisen, 1999), (Stuntz *et al.* , 1999)
Thermography	Seeks tumors by enhanced infrared radiation	Increased temperature caused by increased metabolic activity	Screening			(Foster, 1998)
Electrical Impedance Imaging	Maps the breast's impedance with low-voltage signals	Change of average impedance of the tumor site		Diagnosis	Screening	(Kleiner, 1999),
Optical imaging	Localizes tumor by measuring scattered and transmitted near-infrared light	Increased light scattering and absorption		Diagnosis	Screening	(Pogue *et al.* , 2001), (McBride *et al.* , 2001), (Suzuki *et al.* , 1996), (Fantini *et al.* , 1997)

continued on next page

continued from previous page

Technology	**Description**	**Tumor contrast feature**	**Used routinely**	**Role suggested by preclinical data**	**Role suggested by clinical data**	**Relevant research references**
Electrical potential measurement	Identifies tumor by measuring of potentials at array of detectors on skin	Electrical gradient caused by rapid tissue proliferation		Diagnosis	Screening	(Faupel *et al.* , 1997), (Cuzick *et al.* , 1998)
Positron emission tomography	Forms images using emission from annihilation of positrons from radioactive pharmaceuticals	increased metabolic activity		Screening, diagnosis		(Phelps, 2000), (Stuntz *et al.* , 1999),(Edel & Eisen, 1999)
Elastography	Uses ultrasound or MRI to infer the mechanical properties of tissue	Difference of tissue elasticity		Screening, diagnosis		(Gao *et al.* , 1996), (Sarvazyan, 1995), (Plewes *et al.* , 2000), (Lorenzen *et al.* , 2002)
Magnetic resonance spectroscopy	Analyzes tissues's chemical makeup using radio emission from nuclear spin	Increased water content		Screening, diagnosis		(Merchant, 1994), (Mountford *et al.* , 2000)
Thermoacoustic and photoacoustic computed imaging	Generates short sound pulses within breast using radio-frequency or near-infrared light energy and construct a 3-D image from them	increased blood or water concentration		Screening, diagnosis		(Kruger *et al.* , 1999a), (Oraevsky *et al.* , 1998) (Hoelen *et al.* , 1998)
Microwave imaging	View breast using scattered microwaves	Increased water content	data not available yet			(Fear *et al.* , 2002), (Bertero *et al.* , 2000), (Meaney *et al.* , 2000)
Hall-effect imaging	Picks up the sonic vibrations of charged particles exposed to a magnetic field	difference of tissue conductivity	data not available yet			(Wen *et al.* , 1998)
Magnetomammography	Senses magnetic contrast agents collected in tumor	Contrast agent uptake	data not available yet			(Clarke, 1994)

Table 1.1: Methods for imaging the breast

At present, X-ray mammography is the only technology sufficiently well developed for screening of the general population for breast cancer. It therefore serves as a "gold standard" with which new technology will be compared. However, this standard is imperfect. There are many ways to improve sensitivity and specificity of this method, and to make it more patient friendly, but in case of the absence of calcifications and pure radiographic contrast between tumor and healthy tissues X-ray mammography is not applicable. This usually happens with younger women. Efforts have been made to identify alternative or complementary screening approaches for younger women at high risk. Magnetic resonance imaging and ultrasound have been studied more extensively in this regards. Most of the imaging technologies for breast cancer detection mentioned in this chapter are being developed as diagnostic adjuncts to X-ray mammography and cannot be considered in isolation, as in screening programs.

1.2.5 Optical mammography and spectroscopy

Among the alternative techniques presented in table 1.1 optical imaging using near-infrared light (NIR) has attracted considerable interest (Pogue *et al.* , 1997), (Ntziachristos & Chance, 1998), (Grosenick *et al.* , 2003). Lesion detection and localization are possible due to the presence of optical absorption contrast between tumors and healthy tissue (Tromberg *et al.* , 2000), (Suzuki *et al.* , 1996), (Pogue *et al.* , 1997) This is due to an increased hemoglobin concentration as a result of angiogenesis (Folkman, 2000). The hemoglobin oxygen saturation of suspicious sites can be reconstructed by spectroscopic analysis and can additionally serve as a criterion for diagnosing malignancy (Tromberg *et al.* , 2000), (Pogue *et al.* , 2001).

Optical imaging techniques involve the detection of photons that propagate through the breast, and using light propagation models reconstruct the optical properties of the illuminated tissue. By varying the wavelength of the optical source the spectroscopic dependance of optical properties can be obtained.
An early transillumination system for breast lesion detection showed low sensitivity and specificity (Moskowitz *et al.* , 1989) but recent technical and mathematical innovation have renewed interest into this technique (Grosenick *et al.* , 1999). The optical imaging techniques can be split in continuous wave (CW) (Colak *et al.* , 1999), time-domain (Grosenick *et al.* , 1999) and frequency-domain (Fantini *et al.* , 1997) groups, where each one has its own strengths and weaknesses.

Optical imaging is popular because the technique is relatively inexpen-

sive, and the non-ionizing nature of NIR light makes it risk-free. However, light propagating in biological tissue is highly scattered, resulting in poor resolution. Improving spatial resolution and discriminating between absorption and scattering remain the biggest challenges that are faced by optical imaging.

Optical mammography has not shown the potential to be a stand alone imaging modality, mainly because of its low specificity and sensitivity. Nevertheless, it may supplement existing breast imaging techniques by characterizing lesions in suspicious cases, resulting in a reduction of the number of unnecessary biopsies.

1.2.6 Thermo/Photo-acoustics

Thermoacoustics exposes the breast to short pulses of externally applied electromagnetic energy. Differential absorption induces differential heating of the tissue followed by rapid thermal expansion. This generates sound waves that are detected by acoustic transducers positioned around the breast (Kruger *et al.* , 1999a). Tissues that absorb more energy expand more and produce higher amplitude sound waves. The time-of-flight, amplitude and duration of acoustic pulses recorded on the tissue surface possess information regarding the location, absorption and dimensions of the source, thereby permitting a three-dimensional reconstruction of the absorber.

When the incident electromagnetic energy is visible or NIR light, the term "photoacoustics" is used instead of thermoacoustics (Hoelen *et al.* , 1998).

Photoacoustics combines the advantages of two techniques. Firstly like optical mammography, photoacoustics probes the optical contrast of the tumor site with respect to surrounding tissue (Pogue *et al.* , 2001), (McBride *et al.* , 2001), (Suzuki *et al.* , 1996); second, like ultrasound, all information about optical absorption inhomogeneities is carried to the breast surface by ultrasound waves which have low attenuation and scattering in soft tissue.

One major limitation of traditional X-ray mammography is that it creates a two-dimensional projection of the breast. Therefore two or more projections are needed to localize the lesion precisely. In contrast, photoacoustics retain three-dimensional structural information. Three-dimensional images are, however, potentially more difficult to display and analyze, and therefore, the time and cost required for image retrieval and analysis are potentially greater then for X-ray mammography.

1.3 Introduction to photoacoustic imaging

1.3.1 Generation of PA signals

Light travelling through turbid media

Since in a turbid medium like tissue, light is scattered and absorbed, the medium is characterized by scattering and absorption coefficients (μ_s and μ_a). These are average inverse distances between two scattering or two absorbing events, respectively.

When a collimated beam light is incident on a turbid medium, the radiance inside the medium can be divided into two parts: the coherent intensity I_c that is the incident intensity attenuated due to scattering and absorption, and the diffuse intensity I_d that consists of light that has been scattered one or more times

$$I(r) = I_c(z) + I_d(z) \tag{1.1}$$

The coherent intensity I_c is found from the initial intensity at the tissue surface I_0 which is attenuated due to absorption and scattering inside the medium according to

$$I_c(z) = I_0 \exp(-\mu_t z) \tag{1.2}$$

where z is the depth under the tissue surface and μ_t is the total attenuation coefficient found as the sum of absorption and scattering coefficients i.e. $\mu_t = \mu_a + \mu_s$. Due to scattering, part of the coherent intensity is transferred to the diffuse intensity, which has the following decay dependence for a point source in an infinite homogeneous medium

$$I_d(r) \propto \frac{1}{r} \exp(-\mu_{eff}\ r) \tag{1.3}$$

In the above relation, μ_{eff} is the effective attenuation coefficient defined as

$$\mu_{eff} = \sqrt{3\mu_a\mu_{tr}} = \sqrt{3\mu_a(\mu_a + \mu_s')} \tag{1.4}$$

where μ_{tr} is the transport attenuation coefficient, $\mu_{tr} = \mu_s' + \mu_a$, and μ_s' is the reduced scattering coefficient, $\mu_s' = \mu_s(1-g)$. The parameter g is the average cosine of the optical scattering angle. Since the forward scattering predominates in soft tissue (Tuchin, 2000) parameter g is close to unity. Therefore attenuation of the diffuse intensity is significantly less than that of the coherent intensity.

For light incident on tissue with a plane geometry (broad beam), the energy fluence rate as a function of depth z asymptotically reaches the dependence (Profio, 1989)

$$F(z) = C \times \exp(-\mu_{eff}\ z) \tag{1.5}$$

where the constant C is proportional to the light energy fluence at the surface.
The asymptotical solution (equation 1.5) is applicable for estimation of the light energy distribution at depths much larger than the diffusion length defined as $1/\mu_{eff}$.

Conversion of light energy into acoustic energy

Photoacoustic signal generation is the result of the photothermal effect. Out of several possible mechanisms (Sigrist, 1986), (Daviest *et al.* , 1993) the thermal expansion is particularly interesting for application in medical diagnosis because it is a nondestructive and noninvasive technique. This generation mechanism is present for all optical intensities and has the highest light-to-sound conversion efficiency among mechanisms occurring below the vaporization threshold.

Absorption of laser radiation in a medium followed by a fast nonradiative relaxation of the excited states converts laser energy into heat. Subsequently, thermal expansion of the tissue under conditions of temporal pressure and thermal confinement causes a pressure rise, ΔP, in the irradiated volume (Gusev & Karabutov, 1993):

$$\Delta P = \Gamma \mu_a F(z) \tag{1.6}$$

where Γ is the thermo-acoustic efficiency, μ_a is the local absorption coefficient and $F(z)$ is the local energy fluence at depth z, that can be found from equation 1.5. The condition of temporal pressure and thermal confinement means that pressure and temperature relaxation during the time scale of the laser pulse is negligible.

The theory of photoacoustic wave generation (Hoelen & de Mul, 1999), (Diebold & Sun, 1994), (Sigrist, 1986) predicts that a spherical body with Gaussian distribution of absorption exposed to a short light pulse, generates a bipolar (also called "N-shaped") pressure transient whose shape is described by the following expression:

$$P(z,t) \propto -P_{max}\left[\frac{v}{r_0}\left(t-\frac{z}{v}\right)\right]\exp\left(-\left[\frac{v}{r_0}\left(t-\frac{z}{v}\right)\right]^2\right) \tag{1.7}$$

where r_0 is the radius of the source expressed as the half width at $1/e$-of maximum amplitude of the initial pressure distribution, v is the speed of sound in the medium, z is the depth from the tissue surface to sphere center, P_{max} is the amplitude of the pressure transient, which is proportional to the amplitude of the initial pressure disturbance. The time between the maximum and minimum (equation 5.1) depends on the size of the source

sphere as $\tau_{pp} = \sqrt{2}r_0/v$.
An object of complicated geometry can be represented as a superposition of point spherical sources and using equation 5.1 the pressure transient produced can be found.

Acoustic wave propagation

The acoustic wave profile can be altered during of propagation through the tissue to the body surface. Mainly three phenomena have to be taken into account. These are the acoustic wave refraction and reflection on the interface of two media with different acoustic properties and a frequency dependence of tissue's acoustic properties.
In liquids and soft tissues only longitudinal acoustic waves are supported. From the continuity of normal velocity follows Snell's law for the angle of the incident, reflected and refracted wave:

$$\frac{\sin\theta_{incident}}{v_1} = \frac{\sin\theta_{reflected}}{v_1} = \frac{\sin\theta_{refracted}}{v_2} \tag{1.8}$$

where θ is the angle with the normal to interface and v_1 and v_2 are the speeds of sound in the first and second medium, respectively. The reflection R_A and transmission T_A coefficients for longitudinal waves are given by (Ristic, 1983):

$$\begin{aligned} T_A &= \tfrac{2Z'}{Z_2'+Z1'}; & R_A &= \tfrac{Z_2'-Z_1'}{Z_2'+Z_1'}; \\ Z_1' &= \tfrac{\rho_1 v_1}{\cos\theta_1}; & Z_2' &= \tfrac{\rho_2 v_2}{\cos\theta_2}; \end{aligned} \tag{1.9}$$

where the prime indicates the adaption of the acoustic impedance $Z = \rho v$ for oblique incidence.

The speed of sound and acoustic attenuation of most biological tissues are frequency dependent (Duck, 1990). Therefore generally pressure transients have to be considered as a superposition of continuous waves obtained from the Fourier transform.

$$P(r, f) = \mathbb{F}^+ P(r, t) \tag{1.10}$$

where $\mathbb{F}^+$ is the direct Fourier transform. Then the distribution of pressure at distance Δr is expressed as

$$P(r + \Delta r, t) = \mathbb{F}^- \left(P(r, f)\exp(-\mu_{ac}(f)\Delta r)\right) \tag{1.11}$$

in above $\mathbb{F}^-$ is the inverse fourier transform, μ_{ac} is the acoustic attenuation coefficient. The average acoustic attenuation coefficient of soft biological tissue can be estimated as following(Duck, 1990):

$$\mu_{ac} = \frac{0.012}{f} \tag{1.12}$$

where f is the frequency of ultrasound in MHz, and the acoustic attenuation coefficient μ_{ac} is measured in inverse millimeters. The numerical constant (0.012) is not dimensionless but measured in inverse millimeters per inverse time. Substitution of the frequency of 1 MHz, that corresponds to the central frequency generated by sphere with diameter of 1 mm, results in the acoustic attenuation of 0.012 mm^{-1}.

1.3.2 Detection of pressure transients

The most widely used methods of detection of acoustic waves at the surface of a sample are piezoelectric, capacitive, electromagnetic and laser interferometric (Scruby & Drain, 1990). Piezoelectric (PE) detection is favored for PA medical imaging since the sensitivity of piezoelectric detectors is 30 to 50 dB higher than in other methods. PE detection is not sensitive to skin roughness and does not require any prior surface preparation as, for instance, do capacitive detectors. However, PE detectors suffer from a nonuniform and bandlimited frequency response.

Since the PA signal frequency band central frequency is inversely proportional to the size of the signal source the central frequency of acoustic detector is defined by the size range of the target object (Oraevsky *et al.* , 1999), (Andreev *et al.* , 2003). In reality the central frequency varies from 40 MHz, for instance for imaging of blood capillaries, down to 300 kHz which corresponds to the central frequency of 10 mm diameter objects such as tumor with increased blood supply. It is not possible to build a piezoelectric detector with a uniform frequency response covering the mentioned range. Therefore the size range of target objects have to be specified dependent on the application considered.

Generally the thickness of the active element and the difference of its acoustic impedance with the front and backing medium defines the frequency response of an ultrasound transducer. The acoustic parameters of the front medium are given. Then, one way to make a broad band (short pulse) transducer is to attach a backing material to the back side of the piezoelectric with an acoustic impedance close to that of the piezoelectric. The backing material chosen should ideally not only closely match the piezoelectric acoustic impedance but also be very absorptive or "lossy" so that no energy is left to be reflected from the non-piezoelectric end of the backing material and create an artifact echo (Kossoff, 1976). Another way is to use a piezomaterial with acoustic impedance close to that of the front medium. In this case the acoustic wave reflected from the back side of the detector propagates back into the tissue without oscillation within piezomaterial. Matching

the acoustic impedances of tissue and detector active material implies two advantages. At first, there is no loss of acoustic energy due to reflection at the tissue-piezomaterial interface. Secondly, the detector has a maximal viewing angle and therefore can acquire signals from objects lying far from the detection axis.

The choice of piezomaterial for utilization in wide frequency band transducers for PA medical imaging is governed by the demand of high detection efficiency, a acoustic impedance closest to tissue and good machinable properties. Polyvinylidene difluoride (PVdF) and copolymer thrifluo-diethylene films satisfy above requirements better then other widely used piezomaterials, for instance quarts and piezo-ceramics (Hoelen, 1998). Therefore these two polymer materials are mainly used in PA imaging for detection of pressure transients.

1.3.3 Image reconstruction

The arrival time, duration and amplitude of the pressure transient report about the distance from the signal source to the detector position, the size and the strength of the signal source, respectively. These parameters permit reconstruction of the source geometry from signals measured in different locations at the surface of the investigated object. A reconstruction can be performed by projection of the recorded signals back to the object space (see figure 1.3)

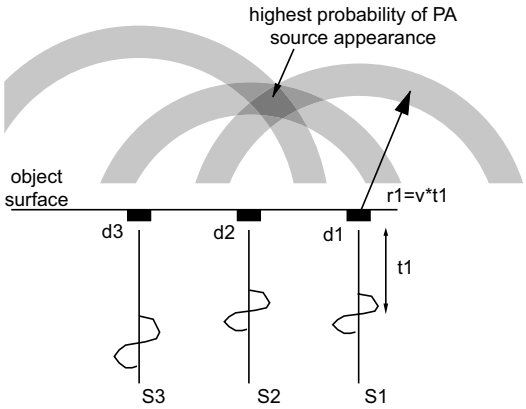

Figure 1.3: Back projection of signals measured by three detectors located at the surface of the investigated object into the object volume. The signal Si is recorded by a detector di. The pressure transient arrival time (ti) defines the radius of a sphere where PA source is located. The crossing point of several spheres has the highest probability of the PA source presence.

However this method is rather time consuming and provides a blurred

image of the body interior.

A number of algorithms have been reported in the literature for various detection geometries (Hoelen & de Mul, 2000), (Kostli *et al.* , 2001), (Xu *et al.* , 2002), (Andreev *et al.* , 2001), (Xu *et al.* , 2003), (Kruger *et al.* , 1999b). Although the mathematical formulation of those methods differs, all of them consider spherical pressure waves in an isotropic nondispersive acoustically homogeneous medium. Although in real tissue the speed of sound differs, the relative difference for soft tissue deviates not more the 10% from the average value i.e 1600 m/s (Duck, 1990). Such a variation can cause the same order (or less) of deviation of the sound wave geometry calculated with the assumption of the homogeneity of medium from a real geometry. However it is acceptable for an approximate calculation.

1.3.4 Wavelength of excitation radiation

The choice of wavelength of the excitation radiation for PA medical imaging is guided by a combination of factors. A high light energy is desirable, since a higher energy available at the absorber yields a higher PA signal. An imaged chromophore should also have sufficient optical absorption contrast with surrounding tissue at the chosen wavelength. This results in higher imaging depths and signal-to-noise ratios (SNR).
Since angiogenesis is the inherent feature of any malignant tumor reaching some growth stage, blood is a medium of interest for PA breast cancer detection with hemoglobin and oxyhemoglobin as the main chromophores. As

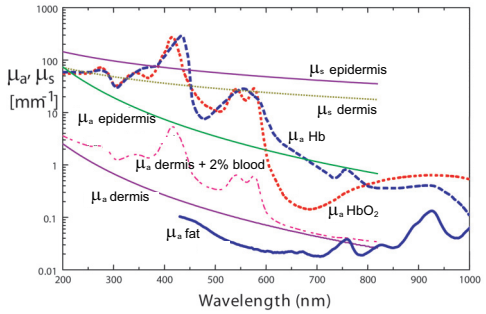

Figure 1.4: Wavelength dependence of optical absorption of blood, skin and fat, and optical scattering of skin (data is obtained from (Welch & van Gemert, 1995), (Jacques, 1996), (van Veen *et al.*, in press)

seen from figure 1.4 blood has a higher optical absorption than other constituent tissues in the wavelength range of visible and NIR light. Moreover, in the wavelength range of 650-850 nm (Spinelli *et al.* , 2004) and 1050-1100 nm (achieved by extrapolation of data from (Spinelli *et al.* , 2004)) the

breast tissues have the lowest effective attenuation coefficient. Therefore the mentioned wavelength regions for PA breast investigation will provide the largest imaging depth.

1.4 Purpose of this work

Combining the strong points of ultrasound and light imaging while avoiding their main drawbacks, photoacoustics has the potential to become a simple, inexpensive, fast, high-resolution 3-D imaging technique to detect malignant tumors at early stages. Since, abnormal increase of blood concentration is the main feature to be detected by photoacoustics, this technique should be insensitive to benign lesions which do not possess invasive potential and do not develop angiogenesis.

Although the field of PA medical imaging is still very young, the development of PA detection of breast cancer has being ongoing already (Kruger *et al.* , 1999b) (Oraevsky *et al.* , 2001). However, only a limited number of patient measurements have been reported. Currently the technique is in its development stage and no systematic clinical trials have been reported.

Besides the above mentioned advantages this technique has some limitation which make PA imaging incapable of becoming a stand alone breast cancer detection modality. This is defined by the following limitations:
- technical. These exist at this state of the art but, potentially, can be solved, for instance limited imaging depth and limited spatial resolutions;
- natural. The tumor contrast feature being detected with PA technique - angiogenesis - is not a unique signature of a tumor and therefore this is not sufficient for diagnosis.
On the other hand an opportunity to detect presence of angiogenesis in combination with information provided by conventional techniques would be a strong criterion for tumor diagnosis. Due these facts the development of PA imaging technique for breast cancer detection does not aim to supplant conventional techniques but rather to supplement them.

The purpose of the present work was to study and develop photoacoustic mammography and to perform a laboratory study of the feasibility of photoacoustic breast tumor detection. This consisted of laboratory testing of instrument parts, development of a solid phantom mimicking optical and acoustic properties of breast tissue, and design of PAM clinical prototype. Finally, the performance characteristics of the developed PAM prototype were determined from the phantom measurements, finally, initial measurements a human volunteer was performed.

Chapter 2

Poly (vinyl alcohol) gel as tissue phantoms in photoacoustic mammography

Abstract

[1]Materials for solid photoacoustic breast phantoms based on poly(vinyl alcohol) hydrogels are presented. Phantoms intended for use in photoacoustics must possess both optical and acoustic properties of tissue. To realize the optical properties of tissue, one approach was to optimize the number of freezing and thawing cycles of aqueous poly(vinyl alcohol) solutions, a procedure which increased the turbidity of the gel while rigidifying it. The second approach concentrated on forming a clear matrix of the rigid poly(vinyl alcohol) gel without any scattering, so that appropriate amounts of optical scatterers could be added extraneously at the time of formation to achieve tunability of optical properties as per requirement. The optical and acoustic properties relevant to photoacoustic studies of such samples were measured to be close to the average properties of human breast tissue. Tumor simulating gel samples of suitable absorption coefficient were created by adding appropriate quantities of dye at the time of formation; the samples were then cut into spheres. A breast phantom embedded with such 'tumors' was developed for studying the applicability of photoacoustics in mammography.

[1]The results of this chapter have been published in:
Kharine, A., Manohar, S., Seeton, R., Kolkman, R. G. M., Bolt, R. A., Steenbergen, W., & de Mul, F. F. M. 2003. Poly(vinyl alcohol) gels for use as tissue phantoms in photoacoustic mammography. *Phys. Med. Biol.*, **48**, 357–70.

2.1 Introduction

Recent years have seen many research efforts in developing optical imaging of tissue into a diagnostic modality, with a thrust in mammography, as an alternative to conventional radiological techniques. Several embodiments of optical mammographs using near-infrared light (NIR) have been showcased in this regard, which can broadly be classified into time-domain (Grosenick *et al.* , 1999), (Hebden *et al.* , 2001) and frequency-domain (Fantini *et al.* , 1997), (McBride *et al.* , 2001) techniques. These techniques have demonstrated that changes in blood flow, oxygen consumption and physiology - fundamental changes associated with tumor growth - can be detected using NIR light (Pogue *et al.* , 2001). The intrinsic non-ionizing nature of the light used furnishes a safer modality compared with x-ray mammography. Additionally, the techniques hold potential for spectrally discerning the signatures of malignant tissue vis-á-vis benign growth (Tromberg *et al.* , 2000), a capability not shared by x-ray techniques. However, there are inherent difficulties in obtaining sharp images with a high spatial resolution at higher depths, accruing from the fact that the nature of light propagation in tissue is highly scattering.

Medical ultrasonography on the other hand is a well-established clinical procedure, which is routinely employed as an indispensable adjunct to conventional x-ray mammography. Compared with light, ultrasound is scattered much less in tissue and therefore lends itself to a higher imaging resolution. Ultrasound however has limitations in sensitivity resulting in many false negatives, which discourages its use for detection (Sabel & Aichinger, 1996).

Recent developments have attempted to combine the intrinsic contrast of tumours to NIR light in optical imaging with the high resolution possible with ultrasound imaging in a variety of hybrid techniques. These include photoacoustic (PA) imaging (Hoelen *et al.* , 1998), (Oraevsky *et al.* , 2002) and references therein), ultrasound-modulated tomography (Wang & Ku, 1998), (Hisaka *et al.* , 2001), and combined ultrasound and NIR diffusive light imaging (Zhu *et al.* , 1999) . In contrast to the other techniques, photoacoustics is intrinsically composite in the sense that the ultrasound is generated internally by the absorption of pulsed laser light. In this, non-radiative deexcitation of the absorbed optical energy takes place with the release of localized heat. The local thermal expansion that results produces pressure transients. When illuminated with pulsed laser light, a tumor site by virtue of its higher absorption with respect to the healthy background tissue, due to angiogenesis (Carmeliet & Jain, 2000), will act

as a source of bipolar photoacoustic pulses (Oraevsky *et al.* , 2002) (and references therein). This ultrasound propagates with minimal distortion to the surface where it is detected using appropriate wideband detectors. The time-of-flight, amplitude, and peak-peak time of the bipolar PA pulse, possess information regarding the location, absorption and dimensions of the source, thereby permitting a reconstruction of the tumor site.

In order to validate the feasibility of these techniques, understand deficiencies such as the limits of detection, and generally to prepare the technique for the transition from laboratory to the clinic, requires the use of stable and reproducible inanimate objects – phantoms – which simulate the properties of tissue relevant to the technique. The literature abounds with descriptions of phantoms for purely optical (Pravdin *et al.* , 2002) (and references therein) and purely ultrasonic techniques (Madsen *et al.* , 1988) (and references therein), but similar reports for the hybrid techniques have been lacking. Phantoms specific to these techniques are singular in that they must possess both the optical and the acoustic attributes of human tissue.

In this chapter, we describe a material that is suitable as a breast phantom for use in photoacoustics, but equally applicable to the previously mentioned techniques as well. The phantom medium is based on poly(vinyl alcohol) (PVA). This is a polymer of considerable interest, owing to the myriad applications in the pharmaceutical and biomedical fields (Hassan & Peppas, 2000). PVA must be in the form of a rigid gel in order to be useful for most applications. An aqueous solution of PVA will in due succession congeal into a gel upon standing at room temperature, but this possesses low mechanical strength and will not be able to support its own weight. A variety of procedures have been adopted to achieve gel reinforcement by enhancing the cross linking between the polymer chains. One mechanism which avoids additives and complex procedures, is that of physical cross-linking. In this, simple freezing and thawing of an aqueous solution of PVA, results in a gel of mechanical strength which progressively increases as the number of freezing–thawing cycles (Peppas, 1975). An attendant phenomenon to this is an increasing turbidity from the clear solution state with an increasing number of these cycles. Such physically cross-linked gels were employed as couplants between ultrasound sources and body parts for the purposes of administering ultrasonic wave therapies, and have been studied for ultrasonic wave propagation (Nambu *et al.* , 1990).

One of the strategies to develop a photoacoustic phantom based on PVA was to utilize the light scattering that is concomitant to the formation of the mechanically rigid gel, and optimize the number of freezing–thawing cycles to obtain optical properties equal to tissue. A second strategy was

to obtain a rigid yet transparent gel; a host to which extraneous scatterers/absorbers could be added at the time of formation. In both cases, the acoustic properties would also have to be found admissible to suit that of tissue.

2.2 Preparation

2.2.1 Method I

PVA with a degree of hydrolysis greater than 99 %, and an average molecular weight (MW) of 85,000 - 140,000 from Sigma-Aldrich, (catalog nr. 36,314-6) was used to prepare aqueous solutions. A PVA concentration of 20 % by weight in solution was obtained by heating the appropriate amounts of PVA and demineralised water over a temperature bath at 95 ^{0}C for 2 hours. Continuous gentle stirring is required to ensure homogeneity and promote dissolution of the PVA. The solution was allowed to stand for a few hours to allow any air bubbles to migrate to the surface from where they can be skimmed off. The solution was then cast in the required molds and refrigerated at -20 ^{0}C for 12 hours. Subsequently the frozen solution was thawed at room temperature for 12 hours. This constituted one freezing–thawing cycle. It was observed that a mechanically rigid and optically turbid gel was obtained. It was also observed that the gels experienced an enhancement in strength and an increase in turbidity with subsequent freezing and thawing cycles.

It is believed that the process of freezing and thawing, in addition to formation of cross-links by hydrogen bonding between the hydroxyl groups on the PVA chains, also promotes the formation of crystallites in the amorphous matrix (Hassan & Peppas, 2000). These serve as additional cross-links to hold the three-dimensional structure together. Such partially crystallized, cross-linked PVA specimens acquire a high mechanical strength since the mechanical load can be supported along the crystallites of the three-dimensional structure. The number, size and stability of the crystallites is increased with the number of freezing and thawing cycles. One of the mechanisms explaining the origin of the turbidity has been that of phase separation in the gel. The structure of the gel may be understood to be composed of 3 distinct phases: a water phase with a low PVA concentration, an amorphous phase and a crystalline phase (Hassan & Peppas, 2000). When refrigerated, the water freezes over, with an accompanying large volume expansion. This leads to the formation of large pores; the resulting refractive index fluctuations in the medium due predominantly to the presence of these pores leads

to the observed turbidity.

2.2.2 Method II

It was demonstrated by (Hyon & Ikada, 1987) that if the freezing of the water phase in the interstitial regions between the PVA chains and crystallites was avoided, while the sample was cooled strongly, then it would be possible to obtain a transparent gel. The cooling to -20 ^{0}C is required to promote crystallite formation and is unavoidable. It was therefore, proposed to inhibit freezing by the addition of appropriate miscible organic solvents to water. It was shown particularly that dissolving PVA in a mixture of water and dimethylsulphoxide (DMSO), the latter having the effect of depressing the freezing point of the water phase to below -20 ^{0}C, yielded highly transparent and mechanically strong gels (Hyon *et al.* , 1994). Beside it an addition of DMSO shifts up boiling point to above 140 ^{0}C. The resulting gels were shown from Scanning Electron Microscope (SEM) studies to be more homogeneous, with smaller pore sizes compared with the 'freeze-thaw' turbid gels; the resulting spatial variation of refractive index in the medium is smaller, explaining the transparency. Additionally, the crystallization process which involves structural rearrangements, can continue to proceed during cooling since the solution state exists without freezing over; the strength of the gel is high.

The procedure followed for the preparation of the transparent hydrogels was based on that described by (Hyon *et al.* , 1989). PVA of the same grade described earlier, is dissolved in a 80:20 mixture of DMSO and water, to obtain a PVA solution of 15 % concentration by weight. The mixture is gently stirred while being maintained at 140 ^{0}C for 2 hours in a temperature bath. Such a high temperature is chosen to decrease the time required to dissolve the PVA. Then the solution is poured in appropriate containers and allowed to stand for a while, to allow the air bubbles that may have been trapped to migrate to the surface, before refrigerating at -20 ^{0}C for 24 hours. The resulting transparent gel samples are then immersed in water to remove the organic solvent. The water is continuously agitated and regularly recharged to promote a thorough exchange of DMSO in the gel with water, to yield the PVA hydrogels. The resulting hydrogels were seen to possess excellent transparency.

As mentioned earlier, it is proposed here to use the transparent gel as the host to which scatterer and absorber particles are to be added. The addition of the correct proportion of these media should impart to the host the required optical properties suggestive of tissue, in particular those of

breast tissue. The optical properties of breast tissue from *in vivo* measurements (Tromberg *et al.* , 2000), (Suzuki *et al.* , 1996), in the visible and NIR yield the following quantities relevant to the design of the phantom: reduced scattering coefficient ($\mu_s^{'}$) $\approx$ 0.6 - 1.3 mm^{-1}; absorption coefficient (μ_a) $\approx$ 0.005 - 0.017 mm^{-1}; mean cosine (g) of the scattering angle (θ) $\approx$ 0.9 (Cheong *et al.* , 1990).

Under simplifying assumptions that the scatterers in the non-absorbing medium are homogeneous dielectric spheres and the electromagnetic field incident on each sphere is a plane wave, single particle Mie scattering theory can be used to calculate the extinction cross-section of the added spheres. This is possible with a knowledge of the relative refractive index (m), between that of the sphere (n_s) and the host (n_0); and the aspect ratio (a) which is the ratio of the sphere's circumference ($2\pi a$) and the light wavelength (λ) in the medium, where a is the radius of the sphere. The refractive index (n_0) of the transparent gel was measured as 1.366 at 589 nm (see section 2.3.1). This is close to the value of the refractive index obtained for human tissue (Tuchin, 2000).

It is known from Mie theory that the scattering introduced by micron-sized spheres is largest if a and λ are of the same order. The reduced scattering coefficient ($\mu_s^{'}$) increases with the relative refractive index (m); anisotropy (g) is maximal when m approaches 1. It is proposed to use a wavelength of 1064 nm from an Nd:YAG laser as the source in the photoacoustic experiments, since light penetration in human tissue is large at this wavelength (Tromberg *et al.* , 2000), a feature that is crucial in mammography owing to the large amount of breast tissue that would be encountered by the light. At this wavelength, it was decided to use borosilicate glass microspheres with a radius of 1 μm, and possessing a refractive index of 1.56 at 589 nm. With this available data, Mie calculations to determine the extinction cross-section (C_{ext}) of the microspheres, were performed using a Monte Carlo package (de Mul *et al.* , 1995). The extinction cross-section is, $C_{ext} = C_{abs} + C_{scat}$, where C_{abs} and C_{scat} refer to the absorption and the scattering cross-sections respectively. With C_{abs} being nominally zero, $C_{scat} \approx C_{ext}$. The anisotropy factor (g), was also determined in the framework of Mie theory calculations. The required reduced scattering coefficient ($\mu_s^{'}$), is related to C_{scat} and the number density (N) as:

$$\mu_s^{'} = (1 - g) C_{scat} N, \tag{2.1}$$

With the required $\mu_s^{'}$ chosen to be 1 mm^{-1}, C_{scat} calculated as 4.0511 μm^2, and g calculated as 0.9, equation 2.5 allows N to be determined as 2.4 $\times 10^6$

microspheres/mm^3. The dimensions and density of the scattering particles, available from the manufacturer's data sheets, allows for the determination of the mass of scatterers to be added.

With this, suitable amounts of borosilicate glass microspheres, were added to the PVA dissolved in the mixed solvent of DMSO and water. Stirring was maintained continuously to disperse aggregations of the scatterers and to ensure homogeneity of the mix. The temperature of the solution was maintained at 140 ^{0}C for 2 hours. The same procedure with regard to the casting, refrigerating and solvent-exchange with water as detailed earlier were followed, to yield gels of the required turbidity.

2.3 Characterization

2.3.1 Optical property measurements

Total attenuation coefficient

The total attenuation coefficient (μ_t) of the samples was measured using a spectrophotometer (Shimadzu UV–3101 PC, Tokyo) using unscattered light through the sample. This was possible with the addition of an aperture stop (1 mm diameter) in the sample-side light beam path of the instrument, in combination with a microcell sample holder provided with masks of dimension (1×1) mm. The aperture stop was positioned in front of the detector exit to line up along the optical axis of the empty sample holder as the point at which maximum light transmittance was obtained. The baseline was recorded in this position. A thin slice of the sample (100–120 μm) sandwiched between 2 microscope cover slides was fixed immediately behind the empty sample holder, as shown in figure 2.1(a). By this arrangement only that portion of the incident beam which did not suffer scattering or absorption was detected (van Staveren *et al.* , 1991). The validity of the Beer-Lambert law was assumed to be applicable. The transmission of the samples was recorded between 800 nm and 1200 nm. Experiments were repeated for 3 specimens of each sample to obtain the scatter about the mean value.

Optical absorption coefficient

The absorption coefficient μ_a of the gel was studied using the setup presented in figure 2.1(a) without additional apertures. The gels were melted-down by heating in sealed vessels to around 90 ^{0}C, poured into 10 mm size cuvettes and the absorption spectrum measured. Melting ensured that the turbid gel

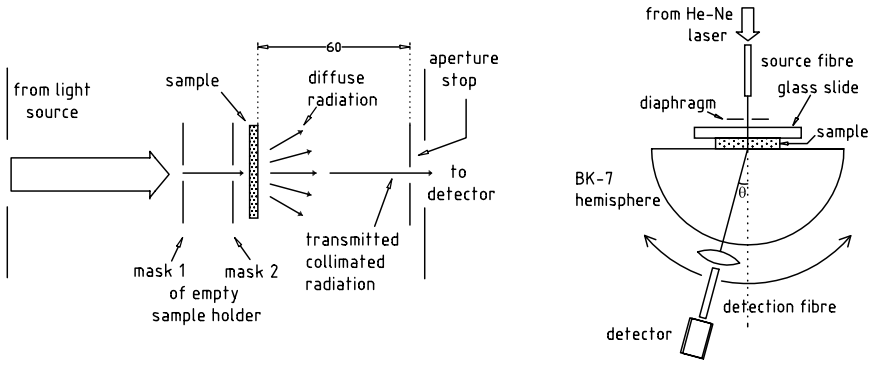

(a) (b)

Figure 2.1: (a) Schematic of modifications in sample side of spectrophotometer to determine the total attenuation coefficient $[\mu_t(\lambda)]$ by collimated transmission measurements. (b) Schematic of goniophotometer for studying scattering phase function $[p(\theta)]$ and determining anisotropy factor (g).

was no longer scattering so that the attenuation through the sample could be attributed only to absorption.

Average cosine of scattering angles

In order to predict the propagation of light in tissue, it is important to know the average angle (θ) by which photons are scattered, since this parameter along with the absorption coefficient (μ_a) will determine the penetration depth of light. The measure of this is in terms of g, the average cosine of the scattering angles or anisotropy factor, $g = \langle cos(\theta) \rangle$. For $g = 1$, all radiation travels along the forward incident direction, and for $g = 0$ scattering is entirely isotropic. Scattering in human tissue is strongly forward-directed (Cheong *et al.* , 1990) and recent human breast tissue *in vitro* measurements (Ghosh *et al.* , 2001) have yielded a value of $g = 0.86$ at 632.8 nm. The angular relationship between the incident direction of radiation and the scattered direction is the scattering phase function $p(\theta)$; this and hence g, can be experimentally determined using a goniophotometer. A schematic of the instrument used is as shown in figure 2.1(b). The angular dependence of the light scattered from a pencil beam by a thin slice (around 100 μm) of the specimen, is measured by rotating a detector in a plane around the sample. Further details regarding the instrumentation are provided in (Bolt & de Mul, 2002). The light source is a He-Ne laser operating at 632.8 nm,

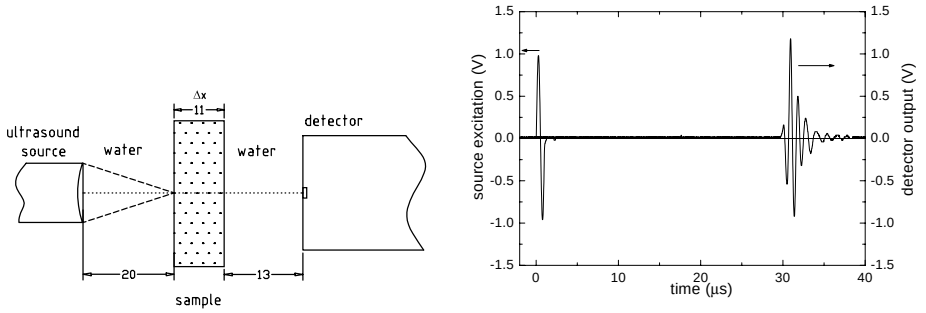

(a) (b)

Figure 2.2: (a) Schematic of insertion geometry for sound velocity (c_s) and attenuation (α_s) measurement. Dimensions in mm. (b) A typical time-of-flight trace of an ultrasound pulse in water without the sample using the 1 MHz ultrasound source.

under the assumption that g depends negligibly on the wavelength, so that the results may be extended to 1064 nm.

Refractive index

Refractive indices of the samples were measured using an Abbe refractometer (Carl Zeiss, Jena). The refractometer was calibrated using the provided test piece. The experiments were repeated for 3 specimens of each sample, and the average refractive index for the samples determined.

2.3.2 Acoustic property measurements

Acoustic velocity and attenuation coefficient

The insertion technique (Bamber, n.d.) was employed to measure the acoustic properties of the samples. This is a relative measurement method using water as the reference, in which the transmission of ultrasonic longitudinal waves through a solid specimen immersed in water are studied. The experimental configuration comprises an ultrasound source and a detector as represented schematically in figure 2.2(a). A typical reference signal measured by the detector in water without the sample, is shown in figure 2.2(b).

For the measurement of the acoustic velocity, the time shift (ΔT) in the arrival of the ultrasound pulse with and without the sample in water is

measured. With a knowledge of the velocity of sound in water (c_w) and the thickness of the sample (Δx), the velocity of sound in the sample (c_s) can be calculated as:

$$\frac{1}{c_s} = \frac{1}{c_w} - \frac{\Delta T}{\Delta x} \tag{2.2}$$

For the measurement of acoustic attenuation, the same geometry is used, with the amplitude of the acoustic pulse with and without the sample in water being measured. The attenuation (α_s) can then be calculated as:

$$\alpha_s = \alpha_w - \frac{1}{\Delta x}\{\ln A_s - \ln A_w - 2\ln(1-R)\} \tag{2.3}$$

In the above, α_i is the attenuation coefficient (cm^{-1}) with $i = s, w$ (sample, water), Δx is the thickness of the slab (cm), A_i is the amplitude of the signal received with $i = s, w$ (sample, water), R is the reflection coefficient at the water-sample interface. R depends on the relative acoustic impedances (z) of water and the sample; z itself depending on the density (ρ) and acoustic velocity (c).

A 20 % PVA solution was cast in a cuboidal mould (32×11×28) mm to undergo the freeze-thaw cycles. After every cycle the acoustic measurements were made in a Perspex tank with deionized water at 22 ^{0}C as the immersion liquid. The sample was placed in the focus of the transducer at a distance of 20 mm with the detector at a distance of 13 mm from the sample surface. The flat parallel side faces of the sample, with thickness 11 mm, provided the acoustic path during the experiments since the top surface of the gel is not smooth owing to expansion of the free surface in the mould during freezing–thawing. The Videoscan immersion series of transducers (Panametrics NDT, Waltham) with center frequencies 1.0, 2.25 and 5.0 MHz were used as ultrasound sources in the configuration described above. All the transducers had element sizes 13 mm and focal lengths 20 mm. The detector was a laboratory made PVDF based disc shaped sensor of the type described in (Hoelen & de Mul, 1999). The transducers were excited with a 1 cycle burst of a sine wave of the appropriate frequency, with a peak-peak voltage of 2 V, and repetition rate 1 KHz. The excitation was provided by a function generator (Model 33250A, Agilent Technologies, Palo Alto). The signal from the detector was monitored using an oscilloscope (TDS 220, Tektronix, Beaverton), and the data transferred to a PC via a GPIB interface.

Density

The densities of the various samples at room temperature were determined using the standard pycnometer bottle with deionised water as reference. The analytical balance (Sartorius BP 210D, Goettingen) used for making measurements is accurate to 0.0001 g. Densities were measured on 5 specimens of each sample to determine the scatter in the values obtained. The scatter in the values about the mean value was between 0.1 % and 0.5 %.

2.3.3 Measured phantom properties

The wavelength dependence of the transmission of the samples, prepared by methods I and II, are shown in figures 2.3(a) and 2.3(c). From the Beer-Lambert law, the transmission is given by:

$$\tau = \frac{I_\tau}{I_0} = \exp^{(-\mu_t d)} \tag{2.4}$$

In the above, τ is the transmission, μ_t the total attenuation coefficient (mm^{-1}) and d the sample thickness (mm); I_τ is the collimated transmission and I_0 the incident intensity. The wavelength dependence of μ_t of the samples, prepared by method I and II, are shown in figures 2.3(b) and 2.3(c) respectively. The scattering coefficient μ_s is obtained from μ_t and the absorption coefficient μ_a as:

$$\mu_t = \mu_s + \mu_a \tag{2.5}$$

Absorption coefficient of method I samples were measured from melted-down freeze-thawed gel. As can be seen in figure 2.3(e) the result curve follows the curve of water absorption but is shifted up for value of about 0.02 mm^{-1}. At 1064 nm, μ_a(method I) = 0.035 mm^{-1} and μ_a(method II) = 0.025 mm^{-1} respectively; μ_s is calculated using equations 2.4 and 2.5. The scattering coefficients of certain samples studied are presented in table 2.1, juxtaposed with values quoted for human breast tissue. It is seen that for method I samples, μ_s increases with an increasing number of freeze–thaw cycles to yield for 6–7 cycles, a value that approximates that expected of breast tissue. Beyond this, the changes in μ_s are very slight and do not justify subsequent cycling. With the measured value of g (see further) to obtain $\mu_s^{'}$, the suitability of 7 cycle freeze-thawed sample is ascertained; subsequent measurements of parameters of method I samples are confined only to these. Also, the value obtained experimentally from the sample prepared using method II matches the value of μ_s that it is designed for.

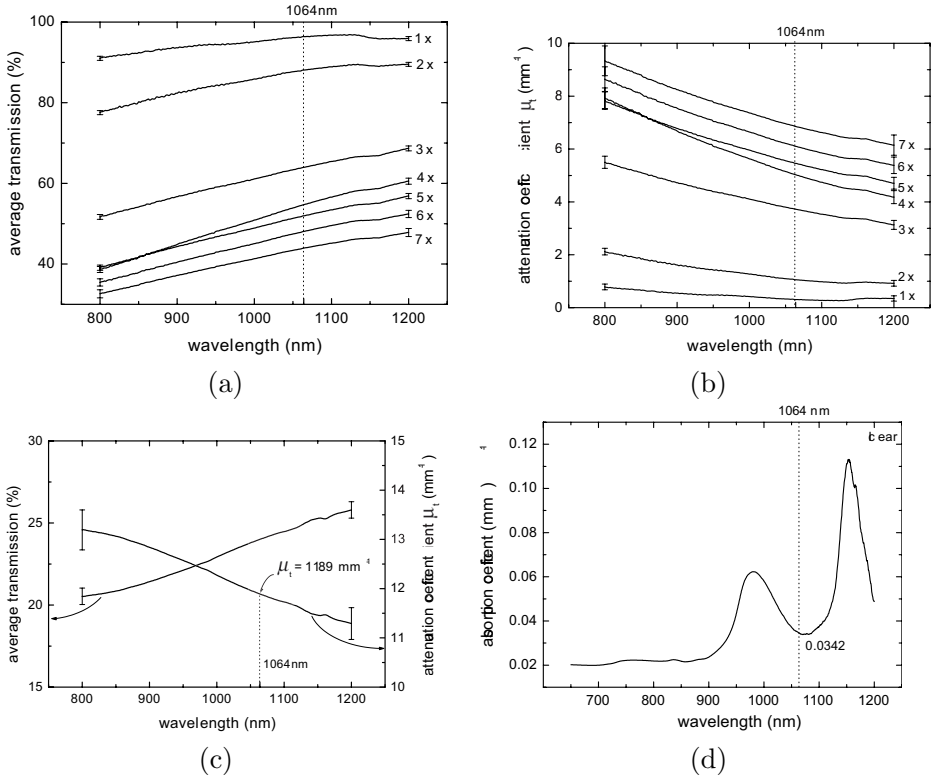

Figure 2.3: All curves are obtained as the mean value of measurements on 3 specimens of each series. The error bars are obtained as the scatter about the average value and are indicated only at the limits of each curve. (a) Wavelength dependence of mean percentage transmission for 120 μm samples prepared using freezing and thawing (method I). The number of freezing–thawing cycles are indicated against each curve. (b) Mean value of total attenuation coefficient μ_t as a function of wavelength, for 120 μm samples prepared using method I. (c) Wavelength dependence of average percentage transmission and the total attenuation coefficient μ_t for a 120 μm sample prepared using method II. (d) Absorption coefficient of melt-down clear freeze-thawed PVA gel sample prepared using method I

The measured output voltage $V(\theta_{obs})$ of the photomultiplier tube, representing collected power versus observed angle θ_{obs}, for a 100 μm thick specimen prepared by method I is shown in a semilog plot in figure 2.4(a). The strong forward directed nature of scattering is evident in the figure. At $|\theta_{obs}| = 63^o$, there is an abrupt fall in the measured output, the signature of total internal reflection occurring at the specimen-glass interface and precluding passage of light to the detector. The raw data requires processing to be available as phase function parameters, also taking into consideration certain sources of error intrinsic to the experiment geometry. The protocol followed for correcting the data is based on that described by (Jacques *et al.* , 1987). The following equations represent a consolidation of corrections to $V(\theta_{obs})$:

$$I(\theta_{exit}) = \frac{V(\theta_{obs})}{V_{dir}(1-r_1)\omega\cos(\theta_{obs})}\left[\frac{\cos(\theta_{exit})n_s^2}{\cos(\theta_{obs})n_g^2}\right]\frac{1}{[1-r(\theta_{exit})]\,(1-r_2)}, \tag{2.6}$$

$$\theta_{exit} = \sin^{-1}\left[\sin(\theta_{obs})\frac{n_s}{n_g}\right] \tag{2.7}$$

In the above, the final result in the series of corrections is $I(\theta_{exit})$, the radiant intensity of light in W sr^{-1} with θ_{exit} the true angle of exitance; V_{dir} is the direct on-axis measurement without the sample and taking into account the neutral density filters used to prevent saturation of the PMT; $(1-r_1)$ is the correction for specular reflection across the 2 interfaces between the 3 media viz. air, glass (microscope slide) and sample assuming passage of light normal to the interfaces; ω represents the solid angle of collection of the detection fibre including the lens; $\cos(\theta_{obs})$ is the correction term for Lambert's law. The term in braces corrects for the reduction in the solid angle due to refraction at the sample-glass (hemisphere) interface where n_i is the refractive index for $i = s$ or g, referring to sample or glass (hemisphere) respectively. Corrections for Fresnel reflection at the sample-glass (hemisphere) interface and specular reflection at the glass(hemisphere)-air boundary are represented by $[1-r(\theta_{exit})]$ and $(1-r_2)$ respectively. The angular dependence of the corrected radiant intensity of the scattered light is the equivalent phase function. This must be fitted to an analytical phase function which permits recovery of the parameter g. In practice it has been found that the Henyey-Greenstein (H-G) function or modifications of it, can model the scattering phase function of tissue to a good approximation, under the assumption that single scattering is present. The expression depends

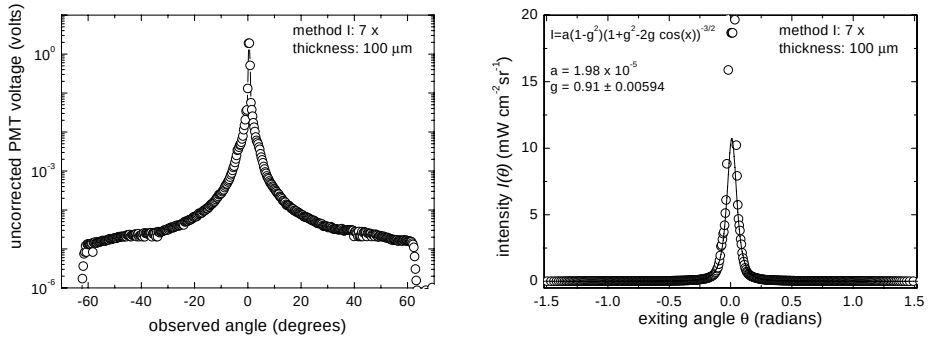

(a) (b)

Figure 2.4: (a) Semi-log plot of angular dependence of light scattering as voltage output of the photomultiplier tube in the goniophotometer setup for the 7 cycle freeze-thawed sample of method I. (b) The experimentally derived scattering phase function obtained by correcting the data obtained. The solid curve is the theoretical fit of the Henyey-Greenstein function to the data.

on g as:

$$I(\theta) = \text{scale}\left[\frac{1-g^2}{(1+g^2-2g\cos\theta)^{3/2}}\right] \tag{2.8}$$

Figure 2.4(b) shows the experimentally derived phase function, to which the H-G function, equation 2.8, is fitted. The theoretical fit is shown as the full line. The light which emanates unscattered together with the light scattered in the on-axis direction ($-1.5^0 < \theta < 1.5^0$) is masked in the fit. An average value of $g = 0.91$ was obtained for samples prepared by method I; and $g = 0.93$ for those from method II. The samples are between 100–120 μm.

Identification of θ_c, the corrected critical angle from figure 2.4(a), and with $n_g = 1.51$ (for BK-7 glass), yields the refractive index for the sample. This was corroborated with measurements using the Abbe refractometer. The results are presented in table 2.1, with a range of values quoted for soft human tissue.

Figure 2.5(a) is a representative plot which shows the time shift and the amplitude change suffered by the water-path ultrasound pulse with the insertion of the sample. The acoustic velocity (c_s) is calculated from equation 2.2, using the velocity of sound in water (c_w) at 22 ^{0}C from (Lubbers & Graaff, 1998). The acoustic attenuation coefficient (α_s) is calculated from

Table 2.1: Relevant optical properties of certain samples studied. With the suitability of the 7 cycle freeze-thawed sample ascertained from the value of $\mu_s^{'}$, subsequent measurements of parameters of method I samples were confined only to these. μ_s was measured at 1064 nm, g at 632.8 nm and n_0 at 589 nm.

Sample	Scattering coefficient μ_s (mm^{-1})	Scattering anisotropy g	Reduced scattering coefficient $\mu_s^{'}$ (mm^{-1})	Refractive index n_0
Method I				
4 cycle	5.04 ± 0.25	-	-	-
5 cycles	5.47 ± 0.23	-	-	-
6 cycles	6.11 ± 0.28	-	-	-
7 cycles	6.90 ± 0.38	0.91 ± 0.01	0.62 ± 0.1	1.360 ± 0.002
Method II	11.8 ± 0.32	0.93 ± 0.01	0.82 ± 0.1	1.366 ± 0.002
Designed	10	0.9	1	
Experiment	13.64	0.93	0.832	1.366 ± 0.002
Tissue	4.28 - 9.28 [a]	0.86 [b]	0.6 - 1.3 [c]	1.33 - 1.55 [d]

[a] Calculated from columns 3 and 4.
[b] From (Ghosh *et al.* , 2001).
[c] From (Tromberg *et al.* , 2000) and (Suzuki *et al.* , 1996).
[d] Typically quoted for soft human tissue (Tuchin, 2000).

equation 2.3, using the value for water at 22 ^{0}C from (Greenspan, 1972). Figure 2.5(b) represents a consolidation of the frequency-dependent attenuation coefficient (dB cm^{-1}) of the 7 cycle freeze-thawed gel, and the gel prepared by method II. The solid lines are power law ($a.f^m$) fits to the data. The relevant data from the acoustic studies are presented in table 2.2, along with densities measured using the pycnometric method and calculated acoustic impedances (kg m^{-2} s^{-1}). From the table, it is clear that most of the acoustic properties of the PVA gel samples match those of human tissue, barring attenuation of samples from method I.

2.4 Phantom fabrication

The PVA gel prepared by method II was chosen to simulate the tumor site tissue.
To obtain required optical absorption coefficient the suitable amounts of the dye, EcolineTM 700 black watercolour (Royal Talens, Apeldoorn), was added to the solution. An empirical formula was used to determine the amount of dye required for various absorption coefficients (μ_a), from the best fit to the experimentally derived graph of absorption versus concentration

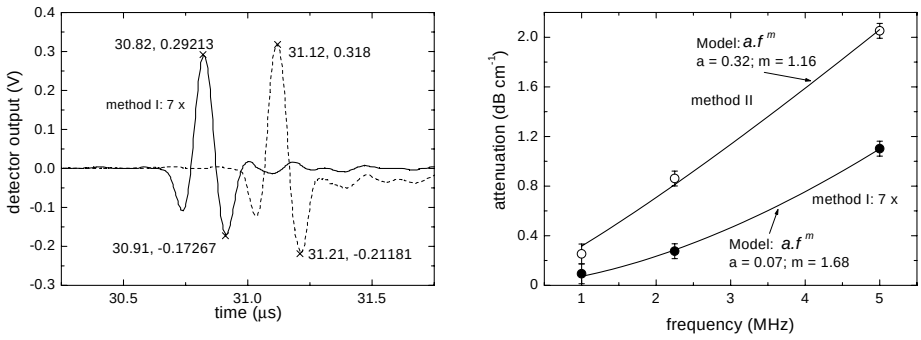

(a) (b)

Figure 2.5: (a) Original water-path ultrasound pulse juxtaposed with the shifted, attenuated pulse following the insertion of the sample (method I: 7 cycles freeze-thawed). The 5 MHz transducer is used as the source. (b) Frequency dependence of mean acoustic attenuation coefficient (α_s), for (•) 7 cycles freeze-thawed gel, and (◦) gel prepared by method II. Each α_s is obtained as the mean value of measurements on 3 specimens of each series. The error bars are obtained as the scatter about the mean value

Table 2.2: Relevant average acoustic properties of samples from method I and method II. Only the 7 cycle freeze-thawed sample of method I is presented.

Sample	Density ρ ($\times 10^3$ kg m^{-3})	Velocity c_s ($\times 10^3$ m s^{-1})	Impedance z ($\times 10^6$ kg m^{-2} s^{-1})	Attenuation α (dB cm^{-1})
Method I	1.03 ± 0.02	1.56 ± 0.02	1.654 ± 0.05	0.19 ± 0.06 [a]
Method II	1.07 ± 0.02	1.58 ± 0.03	1.712 ± 0.064	0.62 ± 0.03 [a]
Tissue	1 - 1.07 [b]	1.425 - 1.575 [c]	1.425 - 1.685 [d]	0.5–1.1 [e]

[a] At 1.76 MHz from power law frequency dependence. See figure 2.5(b).

[b] From (Duck, 1990) p 137.

[c] From (Bamber, n.d.).

[d] Calculated from columns 1 and 2.

[e] Specified at 1.76 MHz from (Duck, 1990) p 103.

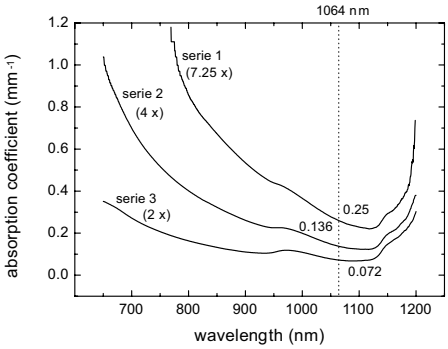

Figure 2.6: Wavelength dependence of the absorption coefficient of the melted-down dyed PVA gel samples

of the dye in water. The absorption of the dye in water had been previously ascertained, using a spectrophotometer, for varying concentrations at 1064 nm. The resulting rigid gel samples were then immersed in water to remove the organic solvent. The water was continuously agitated and regularly recharged to promote a thorough exchange of DMSO in the gel with water to yield the PVA hydrogels. During this process, there was also a release of the dye in the water by diffusion, as was observed by the discoloration of the water. The discharge of the dye reduces after a few days. Three series of gels with Ecoline concentration providing extra absorbance of 0.2, 0.1 and 0.05 mm^{-1} were prepared.

Since dye washing out was observed during removal of DMSO by water exchange, the resulting absorption coefficient of the prepared gel samples was examined.

The same procedure as was used for measurements of absorption coefficient of method I gel samples (see p. 31) was applied. The absorption contrast at 1064 nm for each series was calculated from the ratio of μ_a obtained with that obtained for samples of method I (see figure 2.3(e)), and is indicated against each curve in figure 2.6. Thus, series 1 comprised samples with a μ_a of 0.25 mm^{-1}, series 2 with a μ_a of 0.136 mm^{-1} and series 3 with μ_a of 0.072 mm^{-1} at 1064 nm; absorption contrasts of approximately 7, 4 and 2 respectively, with respect to the background.

The strategy to create the breast phantom with the embedded inhomogeneities was to suspend the earlier prepared dyed spheres using 80 μm nylon thread in a Perspex mould of size approximately (150×60×80) mm dimensions. The mould with its spheres was kept in a tank under water to keep the gels moist. The procedure for making the tissue component of the phantom (method I) was executed. The aqueous PVA solution was removed from the heat and allowed to stand for a while as it cooled. When the aver-

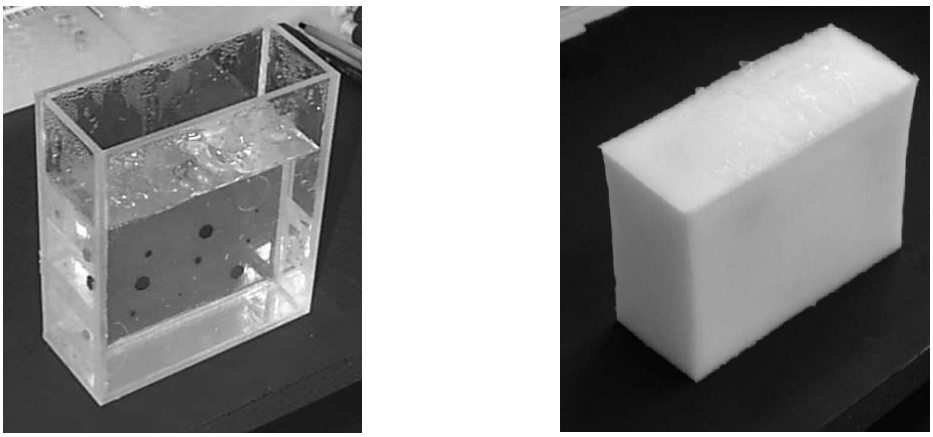

Figure 2.7: (a) The clear aqueous PVA solution in the Perspex mould, which carries the dyed, rigid PVA gel spheres suspended with nylon thread. The solution is allowed to stand at room temperature for a few hours to allow bubbles to rise to the surface, before it undergoes freezing and thawing cycles. (b) The resulting PVA gel breast phantom after submitting the solution to 4 freezing-thawing cycles.

age temperature had reached 45 ^{0}C, the solution was carefully poured into the mould along its sides, upto a height of 120 mm. It was necessary for the solution to be cool enough as to not soften the inhomogeneities (glass transition temperature Tg=60 ^{0}C) yet warm enough for the solution to be mobile enough to be poured. The solution in the mould shown figure 2.7(a) was then made to undergo 4 freezing and thawing cycles to realize the finished breast phantom as seen in figure 2.7(b). It is expected that the breast phantom has a reduced scattering coefficient $\mu_s' \approx 0.5$ mm^{-1} at 1064 nm, which is slightly lower than that which is typically quoted for breast tissue (0.6 – 1.1 mm^{-1}). However this value was chosen to simplify the first set of phantom measurements. Further the bulk absorption coefficient of the prepared phantom can be easily increased by simply subjecting it to further freezing-thawing cycles.

2.5 Discussion and conclusion

The number of cycles of freezing and thawing of the samples prepared by method I have been optimized to 7, to yield a scattering coefficient μ_s that lies in the range typically quoted for breast tissue. Henceforth, only these

samples are considered for the discussion. The data presented also shows that the μ_s of samples prepared by method II can be predicted theoretically, enabling a tailoring of the optical scattering to match that of breast tissue. The strong forward directed nature of scattering in tissue is also well reproduced in both types of samples. The refractive index of the samples was found to be close to that of water and soft tissue. The density and acoustic velocity, which may also be determined by water content, approximate the properties of water and that of soft tissue. The acoustic attenuation of method I samples however, is lower than that of tissue, but this can be corrected for in calculations of acoustic transport in the phantom. These results indicate that the PVA based hydrogels allow for the design of controlled breast tissue phantoms for use in photoacoustic imaging investigations. The use of these materials is not particularly restrictive to this field and they can be applied to the earlier mentioned hybrid techniques. The most salient advantage of these materials as phantoms, over those based on gelatin, agarose and polyacrylamide (Tuchin, 2000) (pp 99-108), is their superior mechanical properties. PVA based gels are rubbery with a high modulus of elasticity. Conventional gels are fragile; they rupture during handling especially for larger sized phantoms and can disintegrate under pressure.

Method II of preparing samples involves the use of scattering additives to the transparent base material and has the advantage that the light scattering behaviour is adjustable. However, the use of well-defined microspheres entails prohibitive expense for large phantoms mimicking whole organs such as the mamma. Method I on the other hand has no such problems since the turbidity is intrinsic to the procedure of rigidifying the gel by physical processing. It is therefore preferable in the fabrication of large volume phantoms. A caveat in the preparation of such phantoms is that the rates of freezing and thawing are crucial in determining the properties. It is recommended therefore, that the optical properties be verified for the rates available for preparation, and that the procedures be followed consistently to obtain reproducibility in properties. That expectation is based on observation of slight visual difference of gel homogeneity on the surface and in the center of the sample with total thickness of 6 cm. An extended study of reasons causing this difference was not performed due to fact that the measured difference of optical attenuation in the central and surface part of sample was not higher than the standard deviation of this from different samples. However one of the reason could be the difference of freezing rate which can be slowed down for the central volume of the large sample by means of increased pressure provided by shell of frozen gel. This effect is expected to result in a higher difference for larger samples.

Regarding the issue of stability, PVA based hydrogels undergo desiccation when exposed to air, causing degradation in the properties. For this reason it is imperative that the gels are stored under water. To prevent dehydration during imaging experiments, several waterproof coatings such as silicone rubber were experimented with, with no success owing mostly to corrosion of the gel by the curing agents required to harden the rubber. Finally, it was decided to employ a layer of ultrasound gel around the sample to retain moisture. PVA gels are also susceptible to proliferation of fungal growth. This can be avoided by storing the phantoms in a 0.01 % solution of sodium azide.[2] Interestingly the samples prepared by method II were resistant to fungus, possibly due to remnant DMSO which may possess fungicidal properties.

A breast phantom was fabricated using method I, by casting the aqueous PVA solution in a cubical Perspex mould of dimensions (150×60×180) mm in which were suspended tumor simulating spheres. Nine 'tumors' of diameters 2, 5 and 10 mm were cut from gel samples with absorption coefficients 0.07, 0.13 and 0.25 mm^{-1} (approximately 2, 4 and 7.5 times that of background) prepared by method II using added absorbers, but without the glass microspheres. The absorber used was Ecoline^{TM} 700 black watercolour (Royal Talens, Apeldoorn) which was added to the DMSO solution at the time of dissolving the PVA. An empirical formula was used for determining the amount of dye required for various μ_a, from the best fit to the experimentally derived graph of absorption versus concentration of the dye in water. There was a small discharge of the dye during the process of DMSO exchange with water, but μ_a measured from the samples after a few weeks in water, matched the values they were designed for. The spheres were suspended using nylon thread at different locations in the mould. The aqueous PVA solution was then poured in carefully, having been cooled from 95 ^{0}C to 45 ^{0}C, so as to not soften/melt the inhomogeneities while still remaining mobile enough to be poured. The mould and its contents were put through the freeze-thaw cycles. Various aspects of photoacoustic imaging techniques relevant to mammography are currently being studied using this breast phantom.

[2]Sodium azide is injurious to human health, and adequate precautions must be taken while handling the solution.

Chapter 3

Performance characteristics of the ultrasound detector matrix

Abstract

[1]The performance characteristics of the planar ultrasound detector matrix intended to be used in the first photoacoustic mammography prototype prototype were studied. Performance studies of the ultrasound detector are presented in terms of sensitivity, frequency response and resolution. The frequency transfer function of an element was measured using an impulsive wave method. The detection frequency band is quoted as from 0.45 to 1.78 MHz. The maximum sensitivity is at 1 MHz. A sensitivity curve and minimum detectable pressure are measured as 94 μV/Pa and 100 Pa, respectively. The lateral size of the point-spread-function of the ultrasound detector in combination with the image reconstruction algorithm has been found as 3.1 mm. Based on the obtained results matrix considered was found to be suitable to study feasibility of photoacoustic detection and localization of breast cancer tumors. The maximum achievable depth for the detection of tumors with 2 times absorption contrast with respect to the healthy breast tissue was estimated based on the value of the minimum detectable pressure found. Basic aspects of the continuous and digital wavelet transform are presented. Results of the manual and automatized wavelet noise reduction are presented and discussed.

[1]Part of results of this chapter are in press as:
Manohar, S., Kharine, A., van Hespen, J. C. G., Steenbergen, W., & van Leeuwen, T. G. 2005. The Twente Photoacoustic Mammoscope: System overview and performance. *Phys. Med. Biol.*

3.1 Introduction

In the photoacoustic (PA) technique an image of the absorbing inhomogeneities in tissue is reconstructed from pressure transients recorded at the surface of the tissue. Therefore the performance of the detection scheme in combination with image reconstruction algorithms defines the quality of the obtained images. The detector sensitivity, frequency transfer function and detection geometry are the key parameters here.

The frequency content of the generated pressure transient is defined by the size and shape of the source. The desire to detect optical inhomogeneities of a wide size range leads to the demand of a wide detection frequency band.

The accuracy of the body interior image reconstruction is defined by the size and shape of the image of the the 3-D point spread function (PSF). The depth spreading of the PSF is defined by the upper limit of the detection frequency band. The lateral spreading is defined by the range of viewing angle to the object. The latter depends on the spatial sampling by detectors on the surface and on the opening angle of each detector. Moreover, the fidelity of the reconstructed image also depends on the chosen image reconstruction algorithm.

The sensitivity of single elements defines the imaging depth. Since the energy fluence of incident light on the human body is limited by safety standards (IEC 60825-1) the amplitude of pressure pulse arriving to the body surface cannot be indefinitely increased by means of increasing the energy of the excitation radiation.

The main limitation of detector sensitivity is its own noise level. This may be reduced by, for example the use of low noise amplifiers in the electrical circuit of the detector, or the use of low temperature detectors leading to a reduction of the detector thermal noise *etc.* Another way to increase sensitivity is to find a method to suppress the noise already contained in the recorded signal. The most common ways are signal averaging and bandpass Fourier filtering. However depending on the characteristic of the signal to be detected other methods of noise reduction can be utilized.

To obtain three-dimensional PA images, pressure transients generated inside tissue have to be measured from a number of locations distributed over the object surface. This can be achieved by scanning a single detector over the body surface or by use of a detector matrix. The first method is flexible due to the opportunity to change the spacing between neighbouring detector positions according to requirements. On the other hand scanning entails additional time. In addition, there could be an acoustic coupling problem with regular repositioning of a detector. Use of a two-dimensional

detector matrix eliminates these complications. When the matrix surface is sufficiently large, repositioning is not required. Moreover the use of multichannel acquisition can significantly reduce the measurement time.

It was decided to acquire and test a two-dimensional large area detector array for various characteristics relevant to photoacoustics, and explore its suitability for use in mammography. This chapter deals with the 590 element detector matrix from General Electric and its characterization in terms of sensitivity, frequency response and resolution. Methods used for determination of these characteristics are described. Based on the findings is was decided to incorporate this device into a clinical prototype of the PA mammograph.
A limitation of the imaging depth is the most significant problem of the PA technique that probes tissue by NIR light. This can be improved by reduction of noise level in recorded signals. Since structures of interest, like single vessels and regions with increased blood content, are space-limited, the generated pressure transients are limited in time. Wavelet analysis is an efficient mathematical technique for the examination of nonperiodic signals. The utilization of the wavelet denoising technique was considered for increasing the imaging depth by reduction of noise level in recorded signals.

3.2 The Ultrasound Detector Matrix

The large-area two-dimensional ultrasound detector array intended for use in mammography was developed by Lunar Corporation, General Electric (Wisconsin, Madison) for use as a receiver in an ultrasonic bone densitometer, the Achilles InSight^{TM}.

The detector was based on a 110 μm thick polyvinylidene fluoride (PVDF) sheet for piezoelectric transduction. Thin gold electrodes were deposited on the front and rear faces of the PVDF sheet by vacuum metallization. These square electrodes, with dimensions of 2×2 mm^2, are arranged with a center-center spacing of 3.175 mm in a rectangular grid with a circular outer edge of 90 mm diameter. To impart the piezoelectric activity to regions sandwiched by the electrods, the PVDF film was polarized by the application of an external electrical field to the electrodes. The spatially selective polarization also reduced the acoustic crosstalk between the 590 elements.

The PVDF film was supported at the front face by an 18.6 mm thick layer of a proprietary material, with acoustic properties matching tissue, which also served as a protective layer. The electrical contacts to the inner face electrodes were obtained by spring-loading conductive pins against the

film. The conductive pins were mounted as a 590 element grid on a printed circuit board (PCB), and connected to signal processing and multiplexing electronics. Control line inputs to the multiplexer on the PCB allowed only one element to be activated at a time. The entire unit with its electronics was enclosed in a chassis.

3.2.1 Element sensitivity

The sensitivity of an arbitrary element was measured with a substitution method using a calibrated hydrophone system. The hydrophone system from Precision Acoustics Ltd. (Dorchester) comprised a Ø 0.2 mm needle hydrophone (HPM 02/1), a submersible integrated preamplifier (HP1) and a DC coupler (DC2). The ultrasound (US) source was a Videoscan immersion transducer (Panametrics, Waltham) with a centre frequency of 1 MHz and a focal length of 20 mm.

The detector matrix was sealed through an aperture at the bottom of a Perspex imaging tank so that the surface of the detector unit was at the same height position with the floor of the tank, as shown in figure 3.1(a). The tank was filled with degassed and deionized water. To position the element plane in the focus of the transducer, the transducer was mounted on an XY scanning stage at 1.5 mm from the surface of the detector, and positioned at the centre of the detector. The transducer was excited with a 1 cycle burst of a 1 MHz sine wave, with a peak-peak voltage of 0.5 V, and repetition rate 1 kHz, using a function generator (Model 33250A, Agilent Technologies, Palo Alto).

Positioning of the US source to focus onto the center of element was hampered by the fact that the elements were hidden by the opaque protective layer. A random element was activated and signals received were monitored using the digitizer. The transducer was then scanned in steps of 0.5 mm around its initial position till the acquired signal intensity obtained as the peak-peak voltage was maximal, indicating that the element was in the focus of the transducer.

Under this condition the excitation to the transducer was reduced from a high value to the point where the received ultrasound pulse was still discernible with a signal-to-noise ratio (SNR) of 2. Signals were acquired by averaging 128 times.

To obtain the detector transfer function this procedure was repeated after substituting the ultrasound detector array with the hydrophone system. With a knowledge of the sensitivity of the hydrophone system from the calibration curve as 36.9 mV/MPa (uncertainty 14%) at 1 MHz, an

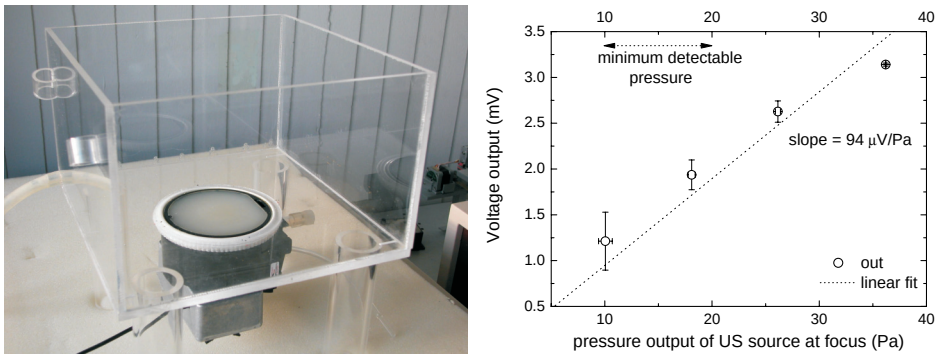

(a) (b)

Figure 3.1: (a) For characterization and phantom experiments, the ultrasound detector matrix was mounted through an aperture in the imaging tank, (b) Sensitivity curve and minimum detectable pressure of the central element of the detector array, obtained using an ultrasound source of known transfer function.

approximate source transfer function was obtained in pressure units versus excitation input. From this, the end-of-cable sensitivity (including signal processing electronics) of the detection element was estimated from the voltage output versus the pressure incident on the element, as shown in figure 3.1(b). An end-of-cable sensitivity of 95 μV/Pa and an approximate minimum detectable pressure of 10 Pa at 1 MHz can be ascertained from the graph.

Please note that this method was approximate since the US source possesses a finite bandwidth, and the calibration curve of the hydrophone system is specified at discrete frequencies. A more accurate measurement of sensitivity is possible using a nonlinear wave propagation substitution procedure (Smith and Bacon 1990). However, this method requires a water bath of several meters long and therefore can only be implemented in a specially designed laboratory.

3.2.2 Inter-element performance

In order to ascertain the element-element variations in sensitivity, a tandem method of measurement was undertaken. Again, after the position of the US source above the central element of the matrix was established as described in section 3.2.1, the source was mechanically scanned in the x and y directions in steps of 3.175 mm (the inter-element spacing). At each

position of the source the appropriate element (if present) in the focus was activated and the signal was recorded. To obtain a map of element positions,

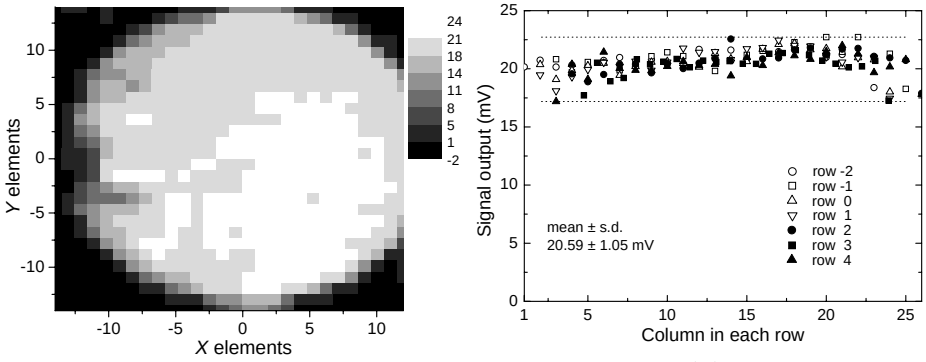

(a) (b)

Figure 3.2: (a) An ultrasound source was scanned above the detector in steps equal to the inter-element spacing. A map of element positions in the detector matrix is obtained as those points where finite peak-peak values are recorded. A circular arrangement of the elements is clearly seen. (b) Value of the peak-peak voltages from a random selection of rows in the matrix. The apparent variation in sensitivity is largely due to difficulties in accurately positioning the source above the elements since these are hidden below the opaque protective layer.

the peak-peak value of the recorded signals was plotted as a B-scan image in figure 3.2(a). Please note that the roughly circular arrangement of the elements was merged by the positions where finite peak-peak signals were recorded. Variations between 7 rows of the matrix as shown in figure 3.2(b), was measured to be $\pm 10\%$. This method, though useful for ascertaining the quality of the elements, was plagued by difficulties in accurately positioning the US source above each element. Barring a few elements which were defective, the inter-element variation in sensitivity could be attributed to slightly out-of-focus elements.

3.2.3 Frequency response

Ultrasound pulses generated photoacoustically from spherical absorbers are bipolar with a positive (compressive) peak and a negative (rarefaction) peak. The duration of the pulse is related to the size of the absorber, with the

peak-peak time (Sigrist & Kneubühl, 1978):

$$\tau_{pp} = \sqrt{2}\frac{r_0}{v}, \tag{3.1}$$

where r_0 is the radius of the absorber, and v the acoustic velocity.

The Fourier spectrum of a bipolar PA pulse reveals that the major portion of the acoustic energy is concentrated in a bandwidth (Oraevsky *et al.* , 1999), (Andreev *et al.* , 2003) given by:

$$f_b = 0.75\frac{v}{r_0}. \tag{3.2}$$

Thus, it is obvious then that the ability of an ultrasound detector to faithfully represent PA transients of absorbers over a range of sizes is determined by the frequency bandwidth of its elements.

Measurements of the frequency response of an element were performed using an impulsive wave method. If the optical penetration depth (δ) in an absorber is smaller than the laser pulse duration dictated resolution, the PA transient produced can be expressed as:

$$\delta = \frac{1}{\mu_a} < \tau_l \; v, \tag{3.3}$$

where μ_a is the absorption coefficient, and τ_l the laser pulse duration.

India Ink (Royal Talens, Apeldoorn), characterized for its absorption coefficient using a spectrophotometer (Shimadzu UV–3101 PC, Tokyo), was used as the absorber. A dilution of 50% India ink in water (μ_a of 214 mm^{-1} at 1064 nm) was used. A Perspex plate of 5 mm thickness was used to sandwich 30 mm of the ink solution against the detector surface. A Q-switched Nd:YAG laser with a pulse width of 9 ns (Quanta Ray PDL-2, Spectra Physics, California) and a beam diameter of 8 mm was used for illumination. Signals were recorded from an element directly beneath the impinging laser beam. Under these experimental conditions the signal represents the end-of-cable impulse response of the element including the characteristics of the electronics. Figure 3.3(a) is a typical signal trace for a fluence rate of 25 mJ/cm^2 at the surface. The Fourier transform of the transient (figure 3.3(b))depicted the broadband nature of the system, with the -6dB bandwidth extending from 450 kHz to 1.78 MHz. From this experiments, we could also determine that the maximum frequency detectable with the system was around 2.5 MHz.

This maximum frequency was important because it determined the minimal radius of a sphere that could be registered by an element. Using the

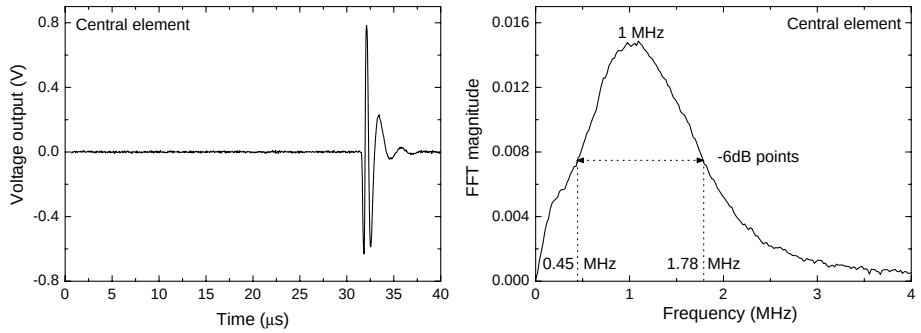

(a) (b)

Figure 3.3: (a) Signal trace depicting the end-of-cable impulse response of the detector element, recorded from the central element of the detector matrix following photoacoustic generation in India Ink solution. (b) Frequency response of the detector element obtained by Fourier transforming the photoacoustic transient. The -6dB bandwidth was approximately 130 % of the central frequency.

relation (Andreev *et al.* , 2003):

$$r_{O\min} = 1.5\frac{v}{f_{\max}}, \tag{3.4}$$

we concluded that the minimum diameter of a sphere that can be resolved by a single element was 1.8 mm.

3.2.4 Resolution

The spatial resolution of an ultrasound detector array is known to depend upon the number of detector elements, inter-element spacing, distance between detector and ultrasound source, and frequency response of the elements (Oraevsky *et al.* , 1999), (Xu & Wang, 2003), (Andreev *et al.* , 2003). In this section, the resolution of our matrix detector was determined based on two methods.

First, the single point definition of resolution was measured as the FWHM (full width at half maximum) of the point spread function (PSF). Secondly, the two-point definition given by the Rayleigh criterion defined as that distance between 2 points at which the peak of one PSF was at the position of which the second PSF was zero, was determined.

We undertook measurements based on both these criteria. Dyed poly(vinyl alcohol) gel spheres without scattering and with an absorption coefficient

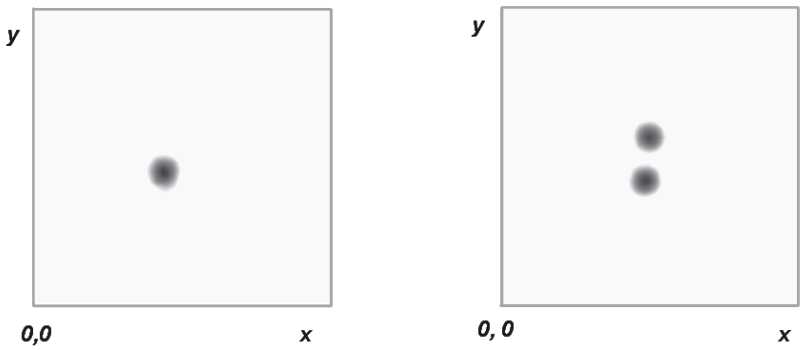

(a) (b)

Figure 3.4: Top view maximum intensity projections (MIPs) of reconstructed data from (a) a single 2 mm diameter absorbing sphere, and (b) two 2 mm diameter absorbing spheres with a separation of 5.5 mm, in low scattering (μ_s=0.3 mm^{-1}) Intralipid. The detector-sphere(s) distance in both cases was 30 mm.

(μ_a) of 0.25 mm^{-1} (Kharine *et al.* , 2003), (Manohar *et al.* , 2004) were fashioned with a scalpel to obtain approximately 2 mm diameter spheres. One or two spheres, depending on whether a single- or two-PSF experiment was being performed, were suspended using a nylon thread (80 μm diameter) in the imaging tank. The spheres were positioned approximately in the centre of the detector matrix. The tank was filled with 4% Intralipid 10% stock solution (Fresenius Kabi, Bad Homburg) so that the spheres were 10 mm below the surface. This solution possesses a low scattering coefficient of 0.3 mm^{-1} at 1064 nm (van Staveren *et al.* , 1991). Photoacoustic signals, which were induced by a Nd-YAG laser (pulse energy 50 mJ, beam diameter 1 cm, repetition rate 10Hz) delivered at the surface of the intralipid solution, were detected successively by the elements in a square area of 52 mm $\times$52 mm area.

The signal traces from each element acquired by the digitizer were saved in the PC to form the inputs to the image reconstruction program based on the delay-and-sum beamforming algorithm (Hoelen and De Mul 2000). This method applies the phase-array approach to algorithmically focus the sensitivity of the detectors in a planar matrix to single voxels or focii, into which the investigated bulk volume is assumed to be divided. The signal

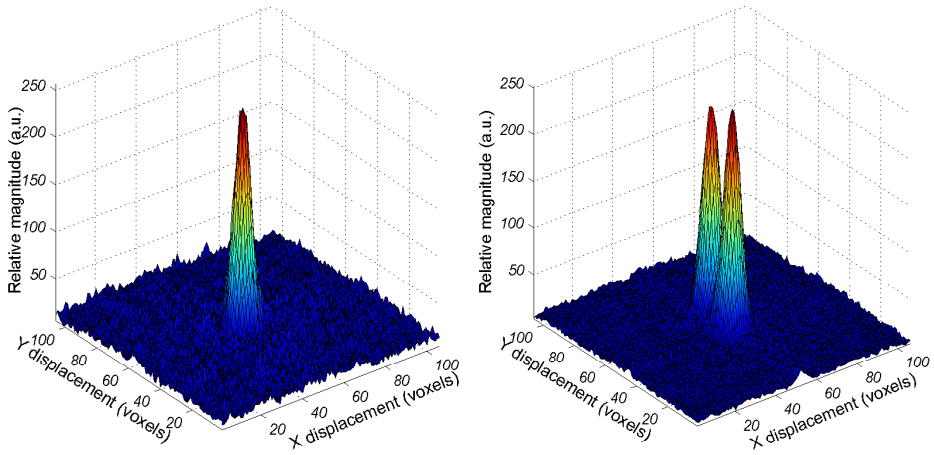

(a) (b)

Figure 3.5: Surface plots of slices through the reconstructed spheres for the two cases in figure 3.4. The x and y axes cover 52 mm since the voxel sizes in the reconstruction were chosen to be 0.5 mm.

from each voxel of the imaged volume is expressed as,

$$S^f(t) = \frac{\sum_i^M w_i^f S_i(t + \tau_i^f)}{M} \tag{3.5}$$

where $S_f(t)$ is the signal from f^{th} focus; $S_i(t)$ is the signal from i^{th} detector; τ_i^f is the time delay of the f^{th} focus to the i^{th} detector; w_i^f is the weightfactor of f^{th} focus to i^{th} detector; M is the number of detectors. The weightfactor in equation 3.5 is the directional sensitivity of the detector for pulsed signals. The result of the focus scanning over the imaged volume is a back projection of the pressure waves measured over the detector matrix area into the object volume. Then the initial pressure distribution is estimated by taking the peak-to-peak value of the backprojected signals within the limited window sliding along the signal length.
The strong PA signals generated from the surface were excluded in the reconstructions. The voxel sizes chosen were 0.5 mm in the x, y and z directions.

The reconstructions are available as 2-D slices of data with the x and y axes corresponding to the area covered and each slice separated by 0.5 mm in the z direction. The data set is normalized to the highest intensity in the data matrix and scaled to 256.

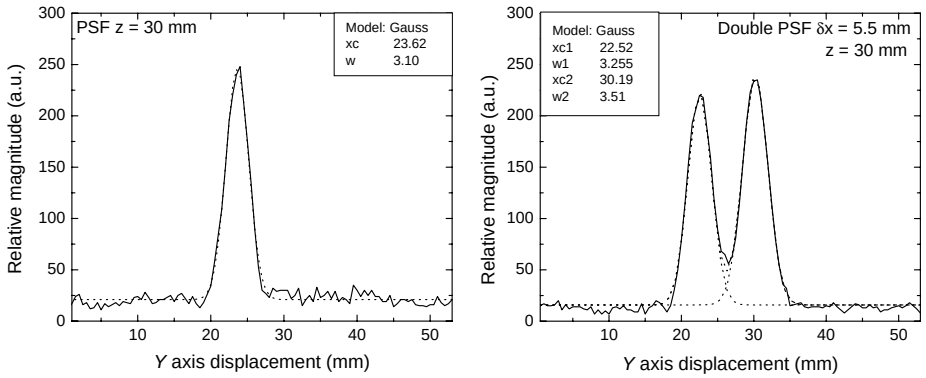

Figure 3.6: Profiles through the point-spread functions (PSFs) for the two cases in figure 3.5. The data has been fitted to the Gaussian distributions. The relevant parameters of the fit are shown in inset; 'xc' the mean, estimates the centre of the PSF; 'w' twice the standard deviation estimates the width of the PSF.

Figures 3.4(a) and (b) show representative top-view maximum intensity projections (MIPs) of single- and two-PSFs for a detector-spheres distance of 30 mm. Figures 3.5(a) and (b) show the surface plots of slices through the centers of the spheres in the XY plane. Gaussians were fitted to the PSFs in both x and y directions through the centers of the spheres in such slices. Figures 3.6(a) and (b) show the fitted data along y directions for the slices. From the single-PSF analysis, the lateral resolution could be ascertained as twice the standard deviation of the PSF's Gaussian fit. Axial resolution was estimated in a similar manner by considering the appropriate slices through the PSFs in XZ and YZ planes, with fitting along the z direction.

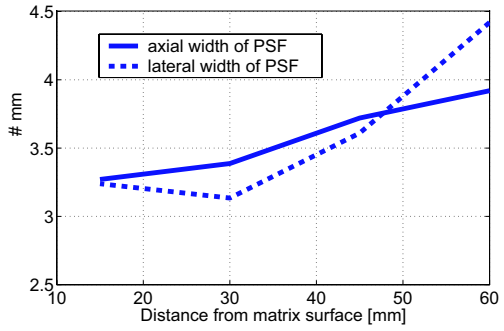

Figure 3.7: Dependence of lateral and axial width at level $1/e$ of maximum of single PSF on distance between the detector matrix surface and absorber.

As seem from figure 3.6 the two-PSF showed no interference between peaks and was a superposition of two single-PSFs. Therefore in further study of dependence of resolution on the depth of inhomogeneities we considered the single PSF only.

Figure 3.7 shows the dependence of the width of a single PSF on distance from the surface of the detector matrix to absorber.

From these studies it could be concluded that the lateral resolution of the system (including the utilized image reconstruction algorithm) was equal to 3.1 mm; the axial resolution - 3.2 mm.

The size of the PSF increased with the increase of depth of the object due to the narrowing of the viewing angle. It is expected that reconstruction of images from, data-sets recorded from a larger surface area should lead to constant sizes of PSFs. However this may lead also to unacceptably long measurement times.

3.3 Estimation of maximum detectable depth

The maximum imaging depth achievable with our ultrasound detector matrix was theoretically estimated. For sufficiently short laser pulse the amplitude of a PA pulse from a spherical body detected at distance z can be expressed as (Hoelen & de Mul, 1999):

$$P_{max}(r) = \frac{\Gamma E_a}{(2\pi)^{3/2}\sqrt{e}zr_0^2}\exp(-\mu_{ac}r) \tag{3.6}$$

where E_a is the light energy absorbed, Γ is the thermo-acoustic efficiency or Grüneisen coefficient ($\Gamma = \frac{\beta v_l^2}{C_p}$), r_0 is the PA source radius, r is the distance from the source to the detector, μ_{ac} is the acoustic attenuation. Let us assume that the measurements are performed in the backward detection mode hence ultrasound detectors are located at the illuminated surface of object. When the size of the absorber is much smaller then the distance from the illumination point to the absorber, and the size of absorber is mach smaller than its inverse absorption coefficient ($a << 1/\mu_a$), the absorbed energy can be expressed as:

$$E_a(z) = \mu_a V_{sp}\Phi(z) \tag{3.7}$$

where z is the distance from the illuminated surface to the absorber, μ_a is the light absorption coefficient of the absorber, V_{sp} is the absorber volume, and $\Phi(z)$ is the laser energy fluence at the distance z from the illuminated

surface.
For a wide uniform laser beam, the energy fluence at depth z can be estimated as (Profio, 1989):

$$\Phi(z) = \Phi_0 \exp(-\mu_{eff}(z)) \tag{3.8}$$

where Φ_0 is the energy fluence at the tissue surface, μ_{eff} is the effective optical attenuation. First we considered that the measurements are performed in backward detection mode (ultrasound detectors located at the illuminated surface of object). Substitution of equation 3.7 and 3.8 into equation 3.6 with $r = z$ results in an expression for the generated pressure

$$P(z) = \frac{2\Gamma\mu_a a\Phi_0}{z\sqrt{2\pi e}} \exp(-(\mu_{eff} + \mu_{ac})z) \tag{3.9}$$

From equation 3.9, we simulated the amplitude of the pressure pulse generated by spherical sources of 2 and 5 mm diameter as a function of depth for a radiant exposure at the tissue surface of 20 mJ/cm^2. The parameters Γ for

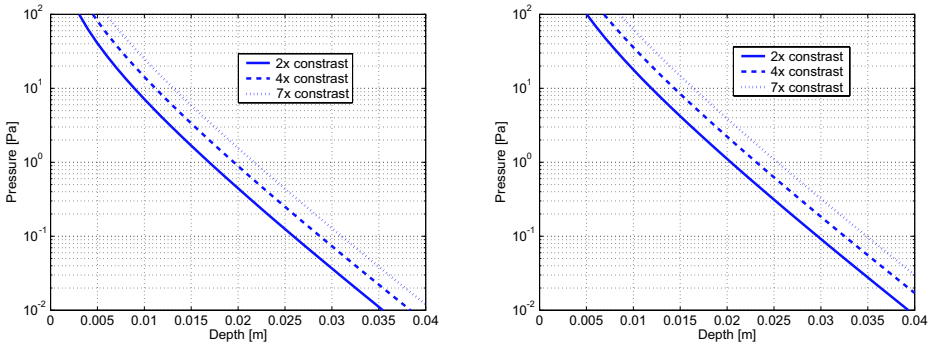

(a) (b)

Figure 3.8: Expected pressure amlitudes as function of the depth of the absorbing spheres with different contrast. (a) - 2 mm diameter sphere, (b) - 5 mm diameter sphere

live biological tissues at the temperature of 37 °C varies in the range 0.45–0.85, being maximal in fatty tissue. Since female breast after menopause consists of mainly fatty tissue (Spinelli *et al.* , 2004) it is reasonable to assume Γ=0.8 for our estimation.
Optical properties of surrounding tissue were taken equal to the PVA gel phantom optical properties i.e μ_{eff}=2.2 cm^{-1}, μ_a=0.35 cm^{-1}. For absorption inhomogeneities of 2x, 4x and 7x contrast the estimated pressure amplitudes are depicted in figure 3.8, while the acoustic attenuation (μ_{ac}) was

set to 0.08 cm^{-1} (Duck, 1990) at a frequency of 1 MHz.

The expected maximal imaging depth can be deduced. Given a minimal detectable pressure of 100 Pa, a single element from the detector matrix e.g. is able to detect a 2 mm diameter sphere of 2 times absorption contrast located at the depth of 4 mm in the case of a single shot measurement. For mammography, this maximal detection depth is unsuitable. Two approaches to increase the maximal imaging depth by decreasing the minimal detection limit can be utilized. First, averaging over N number of recorded signal traces results in increasing of SNR by factor of $\sqrt{N}$. Thus averaging over 100 pulses increases the SNR with a factor of 10. Secondly, the image reconstruction involves summing up of signals from a number of detectors (for more details see Chapter 5). Again, a noise reduction proportional to the square root of the number of detectors involved can be expected.
Consequently, imaging by 100 detectors utilizing averaging over 100 pulses should reduce detection limit by factor of 100. Therefore in example above considered the maximal imaging depth can reach 17 mm. For inhomogeneities with higher contrast or with larger dimensions, the maximal imaging depth will be larger: e.g. a 5 mm sphere with a 7x contrast will be detectable at a depth of 26 mm.

For the estimation of the imaging depth achievable in forward detection mode (ultrasound detectors located opposite to the illuminated surface of the object) the thickness of tissue was set to 6 cm which is the expected thickness of the flattened breast. At such thicknesses the attenuation of pressure transients propagating back to the illuminated surface and forward to the detection surface is negligible. Therefore the achievable imaging depth does not differ much from that presented in figure 3.8.

Thus, averaging of signals will allow the imaging of deeper lying inhomogeneities or smaller inhomogeneities with less contrast. However, this method will increase the measurement time by a factor equal to number of averages.

3.4 Wavelet analysis for PA signal denoising

As an additional noise suppression mathematical methods can be used. Potentially a software denoising can replace hardware methods, for instance signal averaging, and allow performance of several cycles of data processing to optimize used settings. Replacement of signal averaging can significantly reduce total patient contact time. However usage of software denoising

methods does not necessary abolish usage of hardware methods but rather supplements them.

Wavelet analysis is an efficient mathematical technique that is already applied for many fields. Wavelets are used in those cases when the result of the analysis of a particular signal should contain not only a list of its typical frequencies but also knowledge of the definite time or location where these properties are important. Thus, the analysis and processing of different classes of nonperiodic signals (in time or space) is the main field of application of wavelet analysis.

3.4.1 Basis theory of wavelet transform

Continuous wavelet transform (CWT)
The continuous wavelet transform, similar to the short-time Fourier transform which is also known as Gabor transform (Teolis, 1998), maps a function, $s(t)$, into a two-dimensional domain (the time-scale plane) $W_s(a,b)$ given by

$$W_s(a,b) = \frac{1}{\sqrt{a}} \int_{-\infty}^{+\infty} s(t) h^* \left(\frac{t-b}{a} \right) dt = \int_{-\infty}^{+\infty} s(t) h_{ab}^*(t) \tag{3.10}$$

where $h(t)$ is in general called the *mother wavelet*, and the basic functions of the transform, called daughter wavelets, are given by

$$h_{ab}(t) = \frac{1}{\sqrt{a}} h \left(\frac{t-b}{a} \right) \tag{3.11}$$

$h_{ab}(t)$ is a set of basic functions obtained from the mother wavelet $h(t)$ by compression or dilation using a scaling parameter a and temporal translation using a shift parameter b. It is to be noted that

$$h(t) = h_{10}(t) \tag{3.12}$$

The scaling parameter a is positive and varies from 0 to ∞. The signal $s(t)$ can be recovered from the wavelet coefficients $W_s(a,b)$ by the inverse wavelet transform which is expressed as

$$s(t) = \frac{1}{c} \int_{-\infty}^{+\infty} \int_{0}^{+\infty} W_s(a,b) h \left(\frac{t-b}{a} \right) \frac{da}{a^2} db \tag{3.13}$$

where the constant c is found as

$$c = \int_{-\infty}^{+\infty} \frac{|H(\omega)|^2}{\omega} d\omega \tag{3.14}$$

where $H(\omega) = \mathscr{F}\{h(t)\}$ is the Fourier transform of the mother wavelet. Equation (3.13) is also referred to as the reconstruction formula, inverse transform, or synthesis, and equation (3.14) is generally known as the admissibility condition. Any function can be chosen as a mother wavelet as long as the admissibility condition ($c < \infty$) is satisfied.

Digital wavelet transform for PA signal denoising

There are a couple of deficiencies in applying the CWT to real signals. Firstly, CWT can be seen as operators that project the signal $s(t)$ from the one-dimensional time domain into the two-dimensional time-frequency plane. Since no new information can be created by this transform, the same information contained in the signal $s(t)$ with $t \in \mathbb{R}$ is available with the CWT. The increase in complexity from $t \in \mathbb{R}$ to $(a, b) \in (\mathbb{R}^+)^2$ results only in a redundant representation in the signal. This redundancy can be reduced by discretizing the transform parameters (a, b), while taking care that exact reconstruction of the signal still can be achieved. Secondly, in practice we do not have a continuous signal $s(t)$ but a discrete signal.

For computational efficiency, in the digital wavelet transform (DWT) $a_0 = 2$ and $b_0 = 1$ are commonly used so that results lead to a binary dilation of 2^{-m} and a dyadic translation of $n2^m$, where both m and n are real integer numbers. Therefore, a practical sampling lattice is a $a = 2^m$ and $b = n2^m$. Then for the mother wavelet $h_0(t)$, the daughter wavelets are given by

$$h_{nm}(t) = 2^{-m/2} h(2^{-m}t - n) \tag{3.15}$$

An efficient way to implement this scheme using filters was developed in 1988 by Mallat (Mallat, 1989). The Mallat algorithm is in fact a classical scheme known in the signal processing community as a two-channel subband coder. The calculation of wavelet coefficients is nothing but finding the correlation between a chosen wavelet and the considered signal. The calculation of correlation between two signals in the time domain is equivalent to the multiplication of the Fourier spectrum of those. When scaling parameter a is taken as power series of 2, the frequency contents of wavelets in the series do not overlap (see figure 3.9). This allows the use of filters for wavelet decomposition. The filtering of the initial signal into two subbands by high-pass and low-pass filters having equal cut-off frequency is equivalent to one a level wavelet decomposition.

In wavelet analysis, we often speak of approximations and details. The approximations are the high-scale, low-frequency components of the signal. The details are the low-scale, high-frequency components.

The filtering process, at its most basic level, is presented in figure 3.10(a):

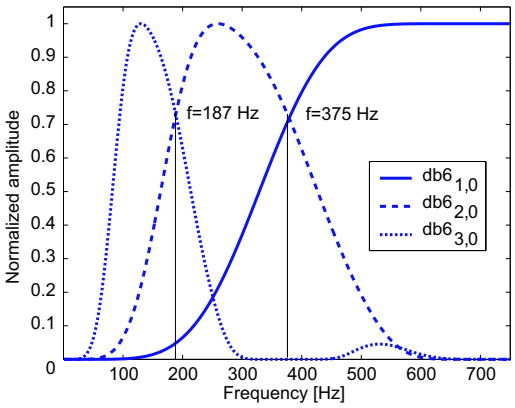

Figure 3.9: Normalized frequency content of Daubechies family 6^{-th} wavelet. $db6_{1,0}$ is scaled by 1 (i.e. mother wavelet), $db6_{2,0}$ is scaled by 2 and $db6_{3,0}$ is scaled by 3

The original signal, S, passes through two complementary filters and emerges

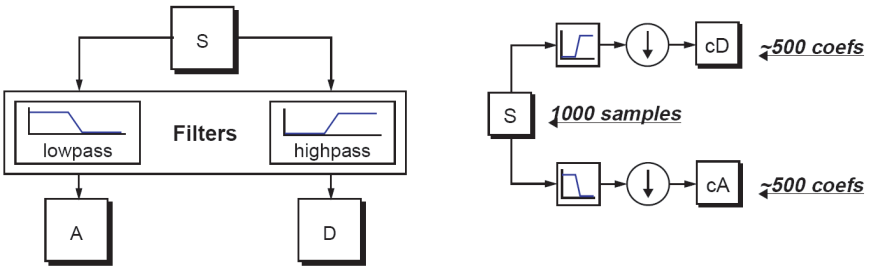

(a) (b)

Figure 3.10: Signal filtering. (a) - a two-channel filtering provides doubling of data, (b) - the filtering with subsequent downsampling of the resulting filtered signals provides output data size equal to input one

as two signals: the approximations (A) and the details (D). The actual performance of this operation leads to doubling of the data-size i.e. if the original signal S consists of 1000 samples, then the resulting signals will each have 1000 samples, for a total of 2000. This can be eliminated applying downsampling[2] of the resulting filtered signals (see figure 3.10(b)). Then the total size of output data is equal to the size of input data. This procedure is referred as one level decomposition.

Multilevel decomposition is iteration of the decomposition process with successive approximations being decomposed in turn, so that one signal is

[2]shortening of signal by removing each second data sample

broken down into many lower resolution components.

The reconstruction of the initial signal is an inverse procedure. Where wavelet analysis involves filtering and downsampling, the wavelet reconstruction process consists of upsampling[3] and filtering.

3.4.2 Noise reduction

Noise reduction involves representation or transformation of the initial signal in such a manner that the signal and noise are easily separated.

Compared to the widely used Fourier smoothing, the main advantage of wavelets lies in the additional "temporal" resolution of the transformed signal. Whereas Fourier filtering affects all data points in the same manner, wavelets allow different parts in the signal frequency spectrum to be filtered individually. This, in principle, promises a considerably more refined and improved treatment of the problem.

Seminal work in this subject has been developed by Donoho (Donoho, 1992) at Stanford University. This approach begins with computing the discrete wavelet transform of the noisy signal. The basic idea behind selective wavelet reconstruction is the following: virtually any time-limited signal can be represented by a small number of wavelet components at the various resolution levels of the wavelet decomposition, whereas the noise has components that cover the complete range.

By choosing a proper wavelet, for example, one that well correlates with the signal to be detected, large wavelet coefficients values are obtained when there is signal, and much smaller coefficients when there is mostly noise. This is the fundamental principle behind the Donoho and Johnstone (Donoho & Johnstone, 1991) idea of wavelet thresholding, in which the signal reconstruction is achieved using only wavelet coefficients whose magnitude are above a specified threshold value λ.

Using the threshold function $\delta_\lambda(s)$, we can thus write the reconstruction formula equation 3.13:

$$s[k] = \sum_{m=0}^{M} \sum_{n=0}^{2^m-1} \delta_\lambda(W_{nm}) h_{nm}[k], \qquad k = 1..K \tag{3.16}$$

where K is the length of the original signal, and $\delta_\lambda(W_{nm})$ is the wavelet coefficient thresholding by λ in general case expressed as:

$$\delta_\lambda(W_{nm}) = \begin{cases} W_{nm} & if \quad W_{nm} \geq \lambda \\ 0 & if \quad W_{nm} < \lambda \end{cases} \tag{3.17}$$

[3] lengthening a signal by inserting zeros between samples

Thus the last question is: How is the value of threshold λ to be determined? The minimax thresholding (Donoho & Johnstone, 1991) or Stein's unbiased risk estimation (SURE) (Steins, 1981) are widely used for this purpose.

3.4.3 Manual wavelet denoising of measured signals

An example of manual wavelet denoising of a measured signal from a dyed PVA gel sphere suspended in an Intralipid (IL) solution is presented in figure 3.11. The signal was randomly taken from a data-set used for the single-PSF study. The distance between the detector matrix surface and absorbing sphere was 30 mm. To reduce the initial noise level individual signals were acquired by averaging 128 times.
The SNR of the original signal (see figure 3.11 (top)) is approximately 2. The frequency band of noise left after averaging is the same as the desired signal. This is confirmed by results of bandpass Fourier filtering. In this denoising procedure all frequency components not corresponding with the desired signal were suppressed. The remaining signal is presented in figure 3.11 (bottom). The result of manual wavelet noise reduction is presented in figure 3.11 (middle). The denoising procedure involved decomposition of the initial signal by Daubechies family 4^{-th} wavelet. The decomposition depth was equal to 6. The heuristic version of SURE was applied for estimation of the threshold level for wavelet coefficients of each decomposition level. Hard thresholding of wavelet coefficients was applied. Manual selection of the wavelet and the thresholding method was performed based on visual

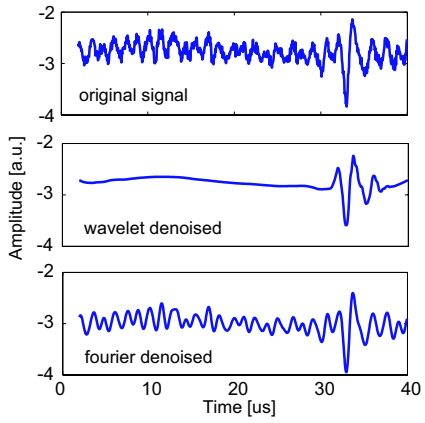

Figure 3.11: Example of noise reduction. (top) - measured signal, (middle) - result provided by wavelet denoising, (bottom) - result provided by Fourier smoothing

analysis of denoising results.

This result of wavelet noise reduction in a single recorded signal is incomparably better than the result of Fourier bandpass filtering. However this is not a representative case for a random experimental signal. The selection of a particular wavelet and thresholding method were based on visual analysis. In turn this analysis was partly based on pre-knowledge about the imaged structure, those are the number of absorbers, their shape and approximate depth.

3.4.4 Automated wavelet denoising using manually found settings

In the real situation, manual denoising of a large data-set using individual parameters for each signal is not feasible due to the large amount of time required for this procedure and the absence of pre-knowledge about the imaged structure.

It can be expected that the best results of noise reduction can be achieved utilizing the wavelet with a shape closest to the theoretically predicted shape of the PA generated pressure transient, for instance an N-shaped pulse. However the shape of the generated pressure transient is defined by a shape of the absorption structure which is not necessarily spherical.

Let us consider quasi manual noise reduction, that involves the usage of settings[4] found from manual analysis of a single signal randomly selected from the data-set to be processed. Figure 3.12 shows results of wavelet denoising of five signals randomly taken from the data-set using settings found earlier (see p.63).

As seen the first out of the five presented signals is heavily distorted by the applied denoising procedure. The amplitude and shape of the pressure pulse which is likely to be a detected PA signal (see figure 3.12 (top) solid line circle) have been changed. A second peak of comparable shape and amplitude has appeared.
Nevertheless the noise of the other four signals has been efficiently suppressed.

[4] these are the choice of the wavelet name and number, and methods to estimate threshold and perform thresholding

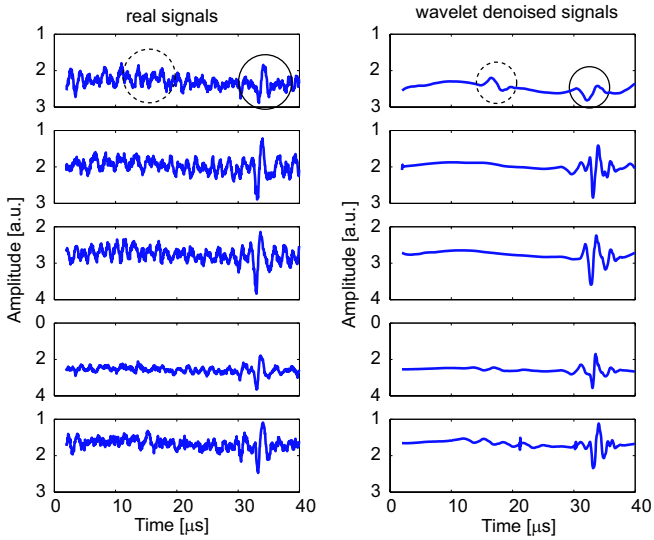

Figure 3.12: Noise reduction of five signal fragments randomly taken from measured data-set (left) by automated procedure involving signal decomposition by the 4^{-th} wavelet of the Daubechies family till depth 6. Hard thresholding has been applied.

3.5 Conclusion

We have studied the performance characteristics of the ultrasound detector matrix. The detection limit of a single element from the detector matrix was measured as 100 Pa. The detection frequency band is from 0.45 to 1.78 MHz, yielding a diameter of 1.8 mm as the smallest sphere that can be axially resolved by an individual detector. The lateral and axial resolutions provided by the studied detector matrix including the image reconstruction algorithm were estimated from analysis of single-PSFs. These were found to be equal to 3.1 mm and 3.2 mm, respectively. The decrease of the final axial resolution of the reconstructed image compared to the one that can be provided by the single element of the detector matrix is caused by the blurring of image by the utilized image reconstruction algorithm.
The area of 52×52 mm allows resolutions between 3–3.5 mm to be achieved, assuming that the absorber lies in the center of the scanning area.

The considered acoustic detector matrix was found to be suitable to study the feasibility of PA breast cancer tumor detection. Axial and spatial resolutions provided by this detector matrix are sufficient to detect and localize tumors with diameter of down to 3 mm. However, for tumors of this size angiogenesis should already occur (Fang *et al.* , 2000). This means the mentioned spatial resolution is not sufficient to determine the threshold size of angiogenic switch from *in situ* to malignant stage. Therefore the

detector matrix used here should be replaced by improved one for future studies.

As to the imaging depth, it was found that optical inhomogeneities of 2 to 7 times absorption contrast can be detected by a single element in single shot measurements at the depth of a few millimeters. To increase the imaging depth to the desired value of 20-30 mm averaging over a number of records is required. These requirements in combination with access to only one element at the time, lead to a rather long measurement time. For instance the time required to image a tissue volume with 45×45 mm surface area is 45 minutes. Thus the long measurement time is the main disadvantage of the detector matrix used in this study.

Use of wavelet analysis for reduction of noise in recorded signals was considered. A comparison of results provided by wavelet noise reduction and widely used Fourier smoothing is presented. The "temporal" resolution of the transformed signal is the main advantage of the wavelets. Unlike Fourier filtering, which affects all data points in the same manner, wavelets allow different parts in the signal frequency spectrum to be filtered individually. It has been shown that the use of wavelets allows a considerably more advanced reduction of noise and the treatment of transients that are limited in time.

Although manual wavelet analysis provided very good reduction of noise, the results of automatized denoising of large data-sets can be more unpredictable. In particular, the shape of some signals can be heavily distorted by the applied denoising procedure. Therefore, to avoid losing and distortion of valuable image information the automatized wavelet denoising is not recommended to be used in basic signal processing procedures set but rather as an optional procedure.

Chapter 4

The Photoacoustic Mammoscope: System overview

Abstract

[1]We present the first prototype Photoacoustic Mammoscope (PAM), intended for initial retrospective clinical studies on subjects with breast tumours. A parallel plate geometry was adopted and the breast is gently compressed between a glass plate and a flat ultrasound detector matrix. Pulsed light (5 ns) from an Nd:YAG laser impinges on the breast through the glass plate in the regions of interest; an appropriate number of the 590 elements of the detector matrix were activated in succession to record photoacoustic signals. 3-D image reconstruction employs a delay-and-sum beamforming algorithm. We discuss various instrumental aspects and the proposed imaging protocol. Details of the patient-instrument interface are provided. Electrical safety aspects of the instrument to be used in the clinic are considered.

[1]Part of results of this chapter are in print as:
Manohar, S., Kharine, A., van Hespen, J. C. G., Steenbergen, W., & van Leeuwen, T. G. 2005. The Twente Photoacoustic Mammoscope: System overview and performance. *Phys. Med. Biol.*

4.1 Introduction

Two instruments for breast imaging using the photoacoustic effect[2] have been reported earlier. The thermoacoustic computed tomography (TCT) scanner comprises a 128 element hemispherically shaped array and utilizes incident radiation of 434 MHz, excitation frequency (Kruger *et al.* , 1999b). It maps the concentration of ionic water (not hemoglobin) in the breast, which is expected to be enhanced at a tumour site due to angiogenesis. Another system, called the laser optoacoustic imaging system (LOIS), uses NIR light pulses for excitation and an arc-shaped 32 element ultrawide frequency band transducer array (Oraevsky *et al.* , 2001). This system is capable of providing 2-D slice images of the breast. A limited number of patient measurements have been reported using both instruments. There have been as yet no large clinical trials and the technique is as yet in its incipient stages.

In this chapter, a new version of a mammography system is presented. The developed instrument is based on the photoacoustic (PA) principle, also using NIR light at 1064 nm. The Photoacoustic Mammoscope (PAM) uses a flat ultrasound detector matrix in a parallel plate configuration. The design of the instrument is based on our experience with a laboratory prototype reported recently (Manohar *et al.* , 2004). Various instrumental aspects and details of the patient–instrument interface are discussed.

4.2 The Photoacoustic Mammoscope

A scheme of the PAM prototype is presented in figure 4.1. The breast is mildly compressed between a glass window and a flat detector matrix. The light source is a Q-switched Nd:YAG laser (Brilliant-B, Quantel, Paris) with a pulse duration of 5 ns and a repetition rate of 10 Hz. The pulse width of the laser is chosen to fulfil the conditions of temperature and stress confinement. The choice of laser wavelength is dictated by the fact that mammography involves imaging through large volumes of tissue; light penetration depth in breast tissue is expected to be maximum in the 1000 to 1100 nm region (Tromberg *et al.* , 2000). The light beam is coupled into a light delivery system and transported to the breast surface. A scanning system translates the output of a light delivery system (LDS) in 2-dimensions to locally illuminate the surface of the breast through the glass window. PA generated

[2]In this article we refer to thermoelastic photo-generation of ultrasound as photoacoustics, whether the photons lie in the microwave, radiowave or optical range of the electromagnetic spectrum.

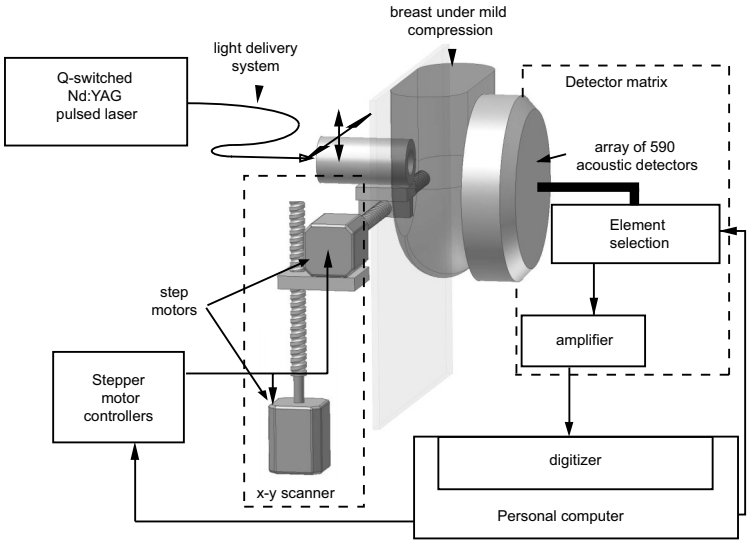

Figure 4.1: Schematic of the Photoacoustic Mammoscope.

ultrasound propagates through the breast to be recorded by the ultrasound detector matrix at the opposite side. A number of detectors appropriate to the desired scanning area are read out. The control lines of the device are controlled via a digital input-output card in the PC. The data line is fed to 1 channel of a dual channel 100 MHz, 100 MS/s, 8 bit digitizer (NI-5112, National Instruments, Austin) card in the PC. The PC runs a LABView program that controls the scanning system, the detector array, and digitizer. Three-dimensional images are reconstructed using a delay-and-sum beam-focusing algorithm (Hoelen & de Mul, 2000). A volume of 50 mm x 50 mm x 60 mm is reconstructed on a 50 x 50 x 60 grid in 2 minutes. The main building blocks of the mammoscope are the light delivery system, the ultrasound detector, and the patient-instrument interface.

4.2.1 Ultrasound detector matrix

The heart of the PAM is a large-area two-dimensional ultrasound detector array developed by Lunar Corporation, General Electric (Wisconsin, Madison). The study of the detector's performance has been considered in detail in Chapter 3. The summary of the study is presented in table 4.1 .

The axial and lateral resolutions of the detector matrix in combination

Table 4.1: The specifications of the ultrasound detector matrix.

Parameter		value/description
Active area shape and size	-	circle of 90 cm diameter
Number of elements	-	590
Single element shape and size	-	square element 2×2 mm
Center-to-center element spacing	-	3.175 mm
Active material	-	polyvinylidene fluoride (PVDF)
Film thickness	-	110 μm
Noise equivalent pressure	-	100 Pa
Frequency band	-	0.45 - 1.78 MHz
Central frequency	-	1 MHz

with the delay-and-sum image reconstruction method (see chapter 5) were measured as 3.2 and 3.1 mm respectively.
The electronic scheme of the matrix only allows access to one element at a time. In combination with the mentioned average sensitivity of the detectors, which necessitates upto 128 signal averages, thus takes 45 minutes to obtain deeper images of a tissue volume with a 45×45 mm surface area. Thus, the long measurement time is the main disadvantage of the detector matrix.

4.2.2 Light delivery system (LDS)

The choice of an appropriate mechanism to deliver light to the breast surface was guided by a combination of two factors: the maximum permissible exposure (MPE) to light on human tissue, and the energy required to perform deep (30+ mm) imaging in phantoms. A high light energy is desirable, since a higher energy available at the absorber yields a higher PA signal and thus higher imaging depths and signal-to-noise ratios (SNR). The MPE for the class of laser used is specified as 30 mJ/cm^2 per pulse. It was also found that at least 50 mJ of light distributed over 2.5 cm^2 at 1064 nm was required to perform deep imaging. Thus, it was decided to look for a mechanism that would permit energies of this order and higher to be transported; and with an additional facility for beam expansion at the output.

Several delivery systems were considered for this application. Silica core single fibres with diameters of several micrometers and fibre bundles with diameter up to several millimeters are most commonly used for delivery of visible and NIR light (Verdaasdonk & van Swol, 1997) and have been well studied. Another alternative is liquid light guides (LLGs) which are efficient in transporting light and also permit easy coupling due to their large

diameters (up to 10 mm). However there are no reports in the literature regarding their power handling capacities.

The use of single silica fibres (up to 0.8 mm in diameter) and liquid light guides (up to 10 mm in diameter) for transporting light was investigated. It was possible to transport only up to 20 mJ of 6 ns NIR laser pulses through a single fibre of 0.6 mm diameter which agrees with earlier reported values (Hand *et al.* , 1999). LLGs were capable of transporting upto 50 mJ pulses, but their prolonged usage was discovered to lead to the formation of bubbles due to thermal decomposition of the liquid which affected the transmission of light. Beyond this, thermal decomposition quickly worsened with use to the point that the liquid became highly discolored and the LLG unsuitable.

As an alternative to the use of light guides, an articulated arm was considered. These usually consist of six to eight mirrors mounted on rotating holders to provide steering in any direction. The holders are connected to each other by a set of rigid tubes. If properly aligned, the beam will exit the arm at the same position and angle independent of the position of the freely movable tubes.

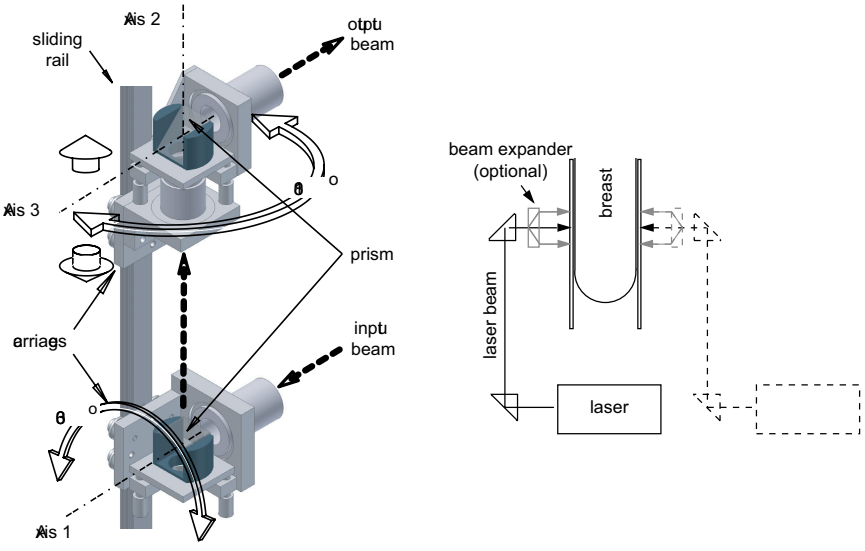

(a) (b)

Figure 4.2: The custom-designed light delivery system: (a) mechanical construction; the input is fitted to the laser, the output mounted on an XY scanning system, (b) possible modes of illumination of the breast

The planar measurement and scanning geometry adopted in PAM render an articulated arm superfluous in terms of the number of degrees of freedom. Therefore, it was decided to develop a custom-designed system specific to the mammoscope based on reflecting prisms. This light delivery system (LDS) is shown in figure 4.2(a). It comprises two mechanical joints and two optical elements and the assembly can provide the required degrees of freedom with appropriate positioning of the laser.

The mechanics of the system are based on linear guidance components (INA-Schaeffler, Germany). Prisms were favored over coated mirrors due to their higher power handling capability. The prisms are mounted on carriages which slide on a rail. The laser beam is coupled in along rotation axis 1 (see figure 4.2(a)). The output beam emerges parallel to the input at variable distances from it. The use of angular bearings allows rotation around axes 1, 2, and 3 (see figure 4.2). Two-dimensional scanning across the breast surface is possible by the rotation of the system around axes 1 and 3, assuming that the input prism holder is fixed to the laser, and the output prism holder mounted as payload on an XY scanning system.

It is also possible to illuminate one or the other surface of the compressed breast as shown in figure 4.2(b). This is made possible by rotation of the output prism around axis 2.

4.2.3 Scanning system

Since the onboard electronics of the detector matrix allow only one element to be read out at a time, illumination of the entire surface of the investigated volume is not required. The local illumination is provided by mechanical scanning of the LDS output over the tissue surface opposite to the activated detector element. The 2-D scanning system compartment used for this purpose is presented in figure 4.3. The scanner is built based on linear guidance systems and high precision ball screws. The total scanning area was chosen as 200x200 mm^2. The minimum scan step size is 25 μm and the positioning repeatability is 5 μm on average. The maximum speed provided by stepper motors is 0.61 cm/s. Further technical details are provided in (Gambini-Rossano, 2002).

4.2.4 Patient–Instrument interface

The instrument is built into a hospital bed as shown in figure 4.4. The subject lies prone on the bed with her breast pendant through the aperture (not shown) in the bed. The breast is mildly compressed between the de-

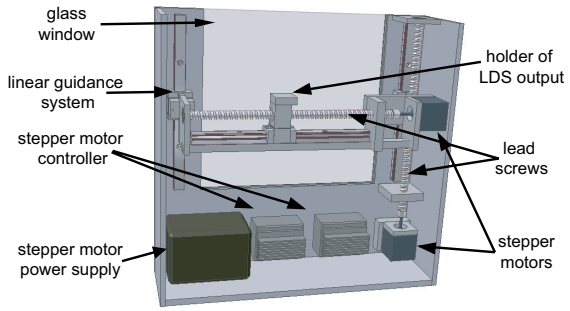

Figure 4.3: 2-D scanning system compartment

tector matrix and the glass plate of a compartment which carries an XY scanning system. Compression is required to obtain a uniform thickness of the breast and a good acoustic contact with the detector. This is achieved by manually turning the handwheel of the compression mechanism. The scanning system based on lead screws has as payload the output of the light delivery assembly. The measuring unit of the instrument consisting of the scanning system, detector matrix and compression mechanism, is mounted on carriages which run on the rails; depending on whether the symptomatic breast is the left one or right, the instrument can be slid accordingly.

The standard examination will comprise a craniocaudal (CC) examination, with illumination on the top surface of the breast, and detection at the bottom. Laboratory phantom studies (Manohar *et al.* , 2004) have revealed that imaging depth may be restricted to 30–35 mm, in which case for thicker breasts a second caudocranial (CC-FB from below) may be required, with the illumination-detection sides exchanged. The instrument base is mounted on an angular bearing which allows the measuring unit to be rotated on its vertical axis. After a CC scan, the breast is retracted, and the LDS detached at the beam output end. The instrument is then rotated through 180^{o}; the laser is slid backward (a linear guidance system is provided for this) and the LDS output reattached to the scanning system to permit a CC-FB scan. This is shown in figure 4.2(b).

4.2.5 Electrical safety

The equivalent electrical scheme of PAM prototype is presented in figure 4.5 The apparatus has a galvanic contact of enclosure to the skin of the patient but not to inner organs or mucous. It does not involve measurements of elec-

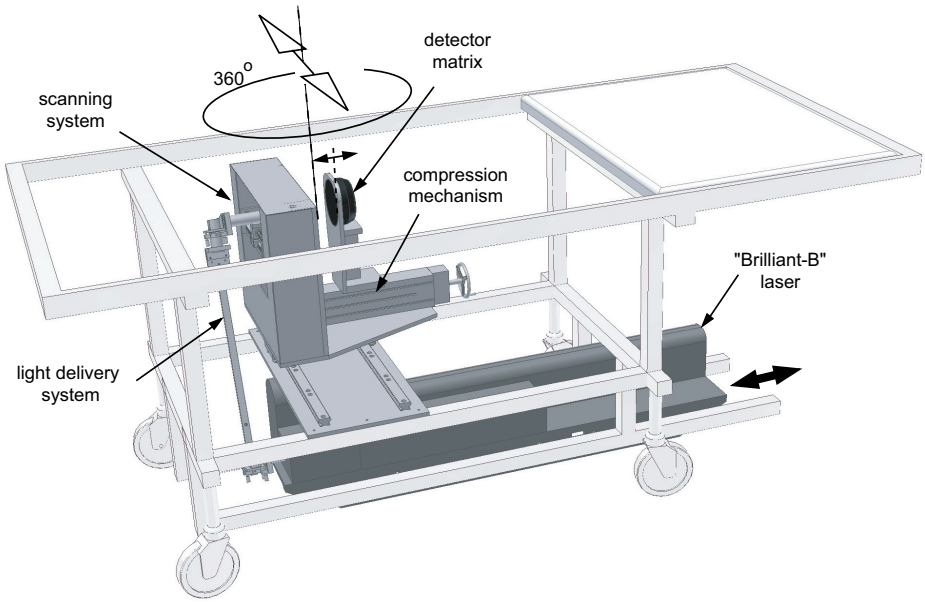

Figure 4.4: The Photoacoustic Mammoscope. The instrument is built into a hospital bed. The top plates of the bed are not shown.

trical signals propagating through the human body. Therefore, according to International Safety Standards (IEC 60101-1) the instrument is classified as an apparatus type "B" with "class 1". In this case the following parameters relating to a medical apparatus are to be measured:

- Mains leakage current — the current flowing from the mains through parts of the apparatus to ground (see figure 4.5, I2).
- Patient leakage current — the current flowing from enclosure or detector through the patient to the grounded part of the instrument or any other grounded objects around (see figure 4.5, I1)
- Mains isolation impedance — the impedance of isolation between mains and a ground line of the instrument or any surrounding objects connected to the ground (see figure 4.5, R1)
- Patient-interface grounding impedance — the electrical impedance between parts which have galvanic contact to patient and ground (see figure 4.5, R2)

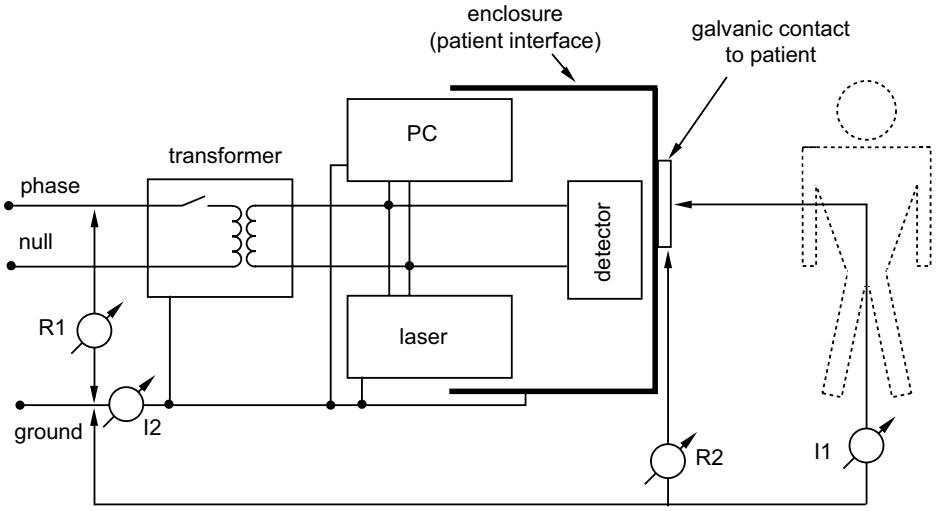

Figure 4.5: Equivalent electrical scheme of PAM prototype including electrical safety circuits

Electrical parameters were measured using a electrical safety analyzer Bio-Tek 601-PRO (Bio-Tek, Vermont, USA). Results are presented in table 4.2.

parameter	**measured value**	**allowed value maximum/minimum**
Mains leakage current	82.9 μA	500 μA
Patient leakage current	36.4 μA	500 μA
Mains isolation impedance	$>$ 20 MOhm	$\geq$ 2 MOhm
Patient interface grounding impedance	0.2 Ohm	0.2 Ohm

Table 4.2: Measured electrical parameters of the PAM prototype and their limit values for instruments type "B" with "class 1", according to the IEC 60601-1" standard

Measured values of the specified parameters showed that the PAM prototype satisfies the conditions required for this class. The grade of patient room where the PAM can be used is "S1". That prohibits the usage of this instrument in the intensive care department or other rooms with life supporting systems. Requirements for room "S1" are specified in the International Safety Standard IEC 60601-1, part NEN3134.

4.2.6 Image reconstruction and volume visualization

Images of the tissue interior are reconstructed utilizing the delay-and-sum beam focusing algorithm (see chapter 3). In short, each voxel of the investigated object is considered as an acoustic source. The signal from the voxel of the imaged volume is expressed as,

$$S^f(t) = \frac{\sum_i^M w_i^f S_i(t + \tau_i^f)}{M} \tag{4.1}$$

where $S_f(t)$ is the signal from f^{th} focus; $S_i(t)$ is the signal from i^{th} detector; τ_i^f is the time delay of the f^{th} focus to the i^{th} detector; w_i^f is the weightfactor of f^{th} focus to i^{th} detector; M is the number of detectors. The weightfactor is the directional sensitivity of the detector for pulsed signals.
To prevent obliteration of image details of the tissue interior by strong signals from illuminated surface these signals are replaced by the constant signal average value, prior to the image reconstruction.

The reconstruction of signals from the investigated volume yields volume data consisting of a collection of slices built through the 3 dimensional subvolume. The volume data is visualized using projections. This is the projection of the data values within the matrix onto a viewing plane. Each pixel stores the maximum value encountered through the voxels in all slices along the viewing ray. The method is called the maximum intensity projection (MIP). Projection visualization of data is commonly used to extract vascular data from medical MRI data sets.

MIP processing has proved to be a useful rendering technique for visualization of sparse objects. However this method may not be convenient to image the breast, which is highly heterogeneous and complex. In this case 3-D iso-surface rendering and composed iso-surface rendering can be used (Kaufman, 1998). The opaque 3-D surface connecting image points of a chosen magnitude, that is also referred to as threshold, is rendered in the first mentioned method. Composed surface rendering plots a number of semi-transparent surfaces each with its own threshold. The main disadvantage of these methods is that only the chosen threshold contours are shown. The threshold value would be desired to correspond to the range boundary of the blood concentration of healthy tissue or boundaries between tissues. However due to heavy light attenuation the PA signal magnitude that will be reconstructed will depend on depth, being much greater near the illuminated tissue surface, and diminishing with depth. That makes it impossible to define a threshold value for the entire imaged volume.

4.3 Mammoscope performance evaluation with solid phantom

The capacity of presented PA imager to detect deeply embedded tumor is of critical parameters to conclude on the feasibility of the PA breast tumor detection.

The performance of the developed PAM prototype was evaluated by imaging of absorption inserts in a solid phantom. The phantom mimics the optical and acoustic properties of breast tissue. The tissue component of the phantom was composed of poly(vinyl alcohol) (PVA) gel. The exact procedure for the phantom preparation has been detailed earlier (see chapter 2). In short, the gel was prepared by submitting a 20% solution of PVA in water to 4 cycles of freezing to -20^{o}C and thawing. Such a procedure imparts the gel with a reduced scattering coefficient ($\mu_s^{'}$) of 0.5 mm^{-1} at 1064 nm. The absorption coefficient (μ_a) of the gel is 0.035 mm^{-1} at 1064 nm. The effective attenuation coefficient $\mu_e = [3\mu_a(\mu_a + \mu_s^{'})]^{1/2}$ is calculated as 0.24 mm^{-1} which is close to values typically quoted for breast tissue in the NIR (Tromberg *et al.* , 2000), (Suzuki *et al.* , 1996). Absorbing gels were also prepared by dissolving PVA in dye solutions at the time of formation. Spheres of these gels were embedded in the phantom to simulate tumors (Manohar *et al.* , 2004).

The solid phantom was placed between the detector matrix and the output of the light delivery system as shown in figure 4.1. Light from the laser was allowed to illuminate the phantom at regions where the inserts were expected. For a certain position of the light, an area of approximately 37×31 mm^2 was covered by reading out signals from a set of 120 elements: 12 in the x direction and 10 in the y direction. Figures 4.6(a) and (b) show maximum intensity projections in side view (i.e projection on the XZ plane) and top view (i.e projection on the XY plane) of the 3D reconstructed data of a selected volume of interest (VOI) in the phantom. The light incident on the phantom was 50 mJ per pulse and signals were acquired after averaging 128 times. The laser beam diameter was adjusted to provide a laser fluence at the phantom surface of around 20 mJ/cm^2.

Three solid phantom optical absorption inserts were measured. The VOI 1 contained a 10 mm sized sphere with an absorption contrast of 2, at a depth of 15 mm from the surface. VOI 2 and VOI 3 contained a 2 mm sized sphere with an absorption contrast of 4, at a depth of 15 mm and a 10 mm sized sphere with an absorption contrast 7 at a depth of 30 mm, respectively. The dimensions of each VOI were 37×31×63 mm^3.

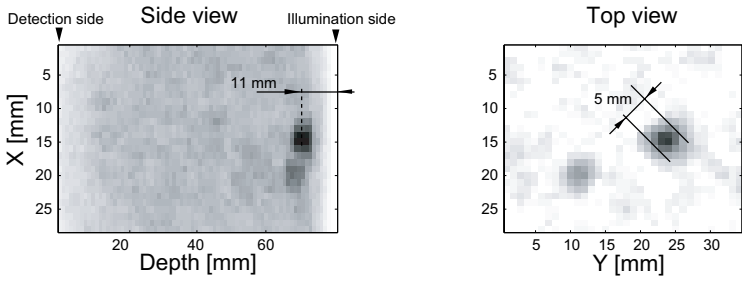

(a) VOI 1. 10 mm sized sphere with an absorption contrast of 2

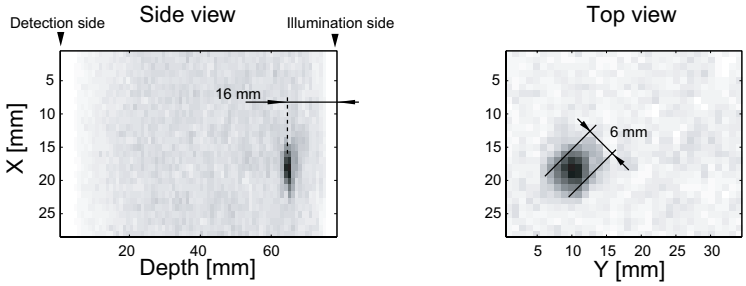

(b) VOI 2. 2 mm sized sphere with an absorption contrast of 4

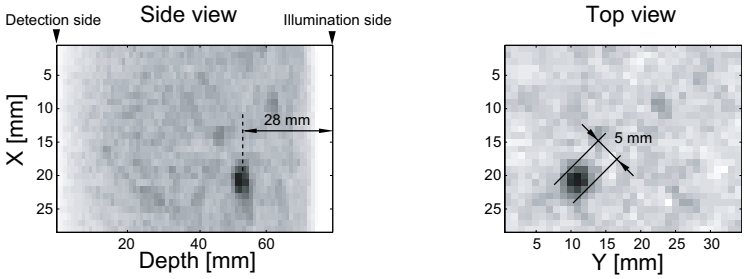

(c) VOI 1. 10 mm sized sphere with an absorption contrast of 7

Figure 4.6: Maximum intensity projections (MIPs) in side view (projection to XZ-plane), and top view (projection to XY-plane) of the 3-D reconstructed data of three volumes of interest (VOI) in the phantom showing a 10,2 and 10 mm diameter sphere of absorption contrast 2, 4 and 7, at a depth of 15, 15 and 30 mm from the phantom surface, respectively

The reconstructions of the presented images were performed using a window size corresponding to the radius of expected inhomogeneities. This explains the proper determination of the object's axial size.

The presence of absorbtion inhomogeneities was unambiguously detected. The distance from the illuminated surface was in good agreement with the expected value. The fact that the found depth of 10 mm sized spheres was smaller than expected (see figures 4.6(a), 4.6(c)), likely suggests that the reconstructed absorbtion peak is not the center of the sphere but part of the sphere surface which is illuminated stronger.
It was shown earlier that the lateral resolution capacity of the detector matrix used in this study in combination with delay-and-sum image reconstruction ranges from 3 to 3.5 mm (see chapter 3). Here the lateral profiles obtained of the 2 mm sized insert has a 6 mm width at half maximum. This widening is explained by narrowing of the viewing angle of the absorber from 56 to 25 degree. The angle narrowing is caused by the reduction of the total transient detection area from 52 mm to 31 mm and the increasing of the distance from the detector's plane to the absorber site.
Recorded signals from deep lying absorber (VOI 3) and the low contrast absorber (VOI 1) have a low SNR. Therefore the base of the reconstructed absorption peaks can be hidden by noise. This results in the shrinkage of reconstructed lateral sizes of absorbers. This effect can observed in images of absorbers located in VOI 1 and 3.

4.4 Discussion and Conclusion

We have developed Photoacoustic Mammoscope and presented the relevant technical details, characterization studies of the detector, a description of the patient-instrument interface, and an imaging example on a solid phantom.

The PAM prototype is capable of imaging inhomogeneities of absorption contrast 7, down to 30 mm depth, and inhomogeneities of absorption contrast 2, down to 15 mm depth in well characterized phantoms. The laser fluences at the surface used in these measurements conformed to the Maximum Permissible Exposure (MPE) threshold for the specifications of the light pulses used. In order to achieve deep (30+ mm) imaging with reasonable signal-to-noise ratios (SNR) it was found necessary to average the individual element signals upto 100 times. Additionally only one element can be accessed at a time. These two factors coupled with the 10 Hz laser pulse repetition rate ultimately set a ceiling to the number of elements that can be scanned in a practical period of time. This is the duration of time

that a human subject can remain immobile with her breast in the scanner without distress. This period is highly subject-dependent but will depend on the patient-instrument interface. This has been the rationale behind the choice of the interface where the patient lies prone on a bed rather then sitting or staying upright.

Based on healthy volunteer feedback, we have decided to limit the measuring time to 45 minutes, which permits an area of 52×52 mm to be scanned with signal averaging of 100, and a pulse repetition rate of 10 Hz. Though this period of time is long for routine clinical examinations, it is admissible for the first human subject tests. The area of scanning with respect to the tumor size should be adequate to obtain sufficient cancerous and healthy tissue in the examination region to establish figures of contrast.

Technological improvements for the developed instrument are being explored, especially with regard to reducing long measurement times. The use of a laser with a higher repetition rate is being considered. A subject of ongoing work is hardware and software modifications required to implement a multi output detector matrix.

Chapter 5

Comparison of image reconstruction algorithms for photoacoustic imaging

Abstract

A comparative performance study is presented for two algorithms for reconstruction of absorbing bodies from a number of cone-beam projections of photoacoustic signals to point detectors distributed on an exterior plane. A frequency-domain algorithm and a time domain delay-and-sum beam-focusing algorithms are considered.
It was quantitatively shown that reconstructions performed using a Fourier transform approach were faster than the corresponding time domain reconstruction but were limited by the detector matrix inter-element spacing. Fast reconstruction with lower resolution may be interesting for rough determination of the volume of interest. It was found that the lateral resolution could be improved by a spatial upsampling of the input data-set for the Fourier transform based algorithm to a density higher than the detector matrix inter-element spacing, but this procedure leads to increased computational requirements.
In the time domain integration of backprojected signals was proposed for reconstruction of the initial pressure distribution. In comparison to the calculation of the peak-to-peak value, the proposed method does not require prior knowledge about the imaged structure.
Both methods provide fairly equal quality of the reconstructed image. The availability of the Fast Fourier Transform (FFT) makes the Fourier transform method favorable for reconstructions. However its higher memory usage can be a serious complication in some configurations.

5.1 Introduction

Photoacoustic (PA) imaging is a technique that probes the optical absorption contrast to NIR light exhibited by biological tissue, without having the problem associated with scattering. Optical absorption contrast between, for instance, tumors and healthy tissue (Tromberg *et al.* , 2000), (Suzuki *et al.* , 1996), (Pogue *et al.* , 2001) on the one hand, and low scattering of ultrasound in breast tissue (Mast, 2000) on the other, are brought together in this hybrid technique (Hoelen *et al.* , 1998). Since the technique does not "look" for photons and the resulting ultrasound propagates with low scattering through tissue, photoacoustics yields a higher resolution than purely optical techniques.

In PA, ultrasound waves are generated internally by absorbing sites illuminated with short pulses of laser light. The time-of-flight, amplitude and duration of the pressure transient generated under irradiation conditions of temporal pressure and thermal confinement[1] provide information regarding the location, strength and dimensions of the acoustic source, thereby permitting reconstruction of the absorber distribution. The choice of an algorithm for reconstruction is partly governed by the configuration of the measurement setup. A number of algorithms have been reported in the literature for various measurement geometries (Hoelen & de Mul, 2000), (Kostli *et al.* , 2001), (Xu *et al.* , 2002), (Andreev *et al.* , 2001), (Xu *et al.* , 2003), (Kruger *et al.* , 1999b). Although the mathematical formulation of those methods differs, all of them consider pressure waves in an isotropic nondispersive acoustically homogeneous medium.

So far, a comparison of various image reconstruction algorithms has not been reported. However, the increasing number of applications of the PA effect and efforts to improve existing imagers make a comparative study of computational requirements and the output image quality of various algorithms under equal operational conditions desirable. The main outcome of such a study should be a selection of the most efficient algorithm for a particular imaging requirement and setup configuration.

In this work we address this question to two computational algorithms developed for a planar detector geometry. The first algorithm is known as the "delay-and-sum (DNS) beamforming algorithm" (Hoelen & de Mul, 2000). In this method signals are projected back into the object space in the time domain. The distribution of PA sources can be found from backpro-

[1] meaning that the pressure and temperature relaxation during the time scale of the laser (heating) pulse duration is negligible

jected signals. In the second algorithm known as Fourier transform based (FT) backward projection algorithm (Kostli *et al.* , 2001), the source geometry is actually recalculated in the Fourier domain and then transformed into the object space. Theoretically, this method should yield an exact reconstruction of the initial pressure distribution.
Images reconstructed by both algorithms under equal computational condition are presented and discussed.

5.2 Methods

5.2.1 Simulated signals and configuration of experimental setup

A straightforward technical definition of "image quality" is based on the answer to the question: How much does an image deviate from the original object? This is called the *fidelity* of the image or "technical image quality" (Pommert & Hohne, 2002). To compare the fidelity of the images reconstructed with the two image reconstruction algorithms, a set of simulated signals from a defined structure has been used.

Figure 5.1 shows the simulated configuration. The detector matrix inter-element spacing has been chosen equal to rounded parameters of the detection unit used in the mammoscope (Manohar *et al.* , 2005). Absorbing structures are in the depth range expected in the real situation.

Pressure transients from the PA sources in water are measured by the

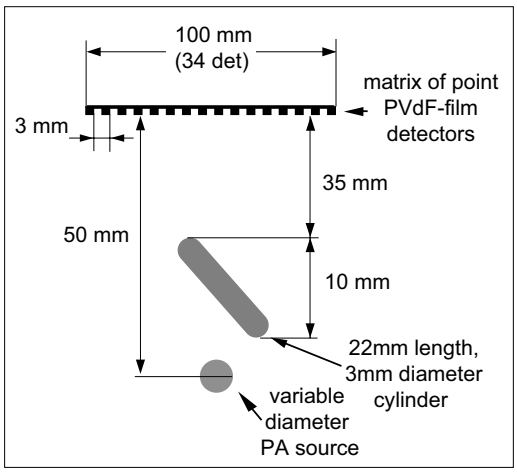

Figure 5.1: example of a simulated configuration. It is assumed that sources are uniformly illuminated.

detector matrix of 34-by-34 elements with 3 mm spacing (see figure 5.1).

Point detectors based on polyvinyldifluoride (PVdF) are simulated to avoid calculation of surface interference of acoustic waves. This implies that the detectors are omnidirectional. Since the critical angle at the water-PVdF interface is 43 degrees, a viewing angle of 86 degrees is obtained. The distance from the detector matrix surface to the deepest PA source is 50 mm. Therefore the detection of signals was limited to within this critical angle.

The theory of photoacoustic wave generation (Sigrist, 1986), (Hoelen & de Mul, 1999) predicts that a spherical body with a Gaussian distribution of absorption exposed to a short light pulse, generates a bipolar ("N-shaped") pressure transient described by the following expression:

$$P(r,t) = -P_{max}\left[\frac{v}{r_0}\left(t-\frac{r}{v}\right)\right]\exp\left(-\left[\frac{v}{r_0}\left(t-\frac{r}{v}\right)\right]^2\right) \qquad (5.1)$$

In the above, $\tau_{pp} = \sqrt{2}r_0/v$ is the time between negative and positive maxima, v is the speed of sound, r is the distance to a field point, r_0 is the radius of source and is equal to half width at the $1/e$ part of maximum amplitude of the initial pressure distribution. The propagating pressure transient is the first derivative of the initial pressure distribution (see figure 5.2) that reflects the distribution of the absorption coefficient.

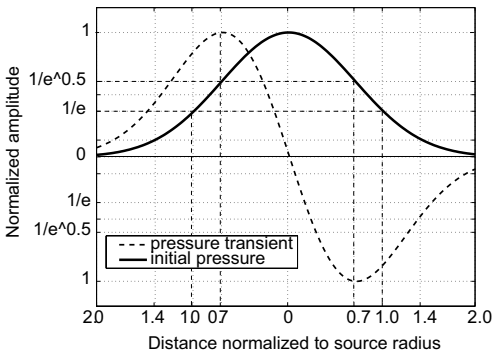

Figure 5.2: Normalized initial pressure distribution and pressure transient propagating to the left

A three-steps study was performed. At first, a data-set of PA signals from single spherical sources of diameters varying from 1 to 12 mm (see figure 5.1) were generated using equation 5.1. The sampling frequency was set to 20 MHz, which is the same as in our experimental setup.
In reality, absorbing bodies are not as simple as single absorbing spheres surrounded by a scattering medium that consists of multiple objects of dif-

ferent size and shape. In this situation, the resolution of the imaging system[2] becomes more important than the definition of the single object size.

The second step then consisted of a multiple source study. To estimate the resolution of an image reconstruction algorithm based on the simulated setup configuration, a data-set sequence of PA signals from two spheres was generated. Sources were 1 mm in diameter with a center-to-center lateral or depth spacing from 1 to 6 mm, with steps of 1 mm. Spheres were either located in the same XY plane and were equally shifted from the setup symmetry axis (laterally spaced) or were located on the setup symmetry axis and were shifted in depth (axially spaced). Random noise with an amplitude standard deviation two times less than the signal amplitude was added, and reconstructions were performed.
The third set of generated data consists of signals from a sphere and a 25 mm length tilted cylinder (see figure 5.1). Both objects were 3 mm in diameter. The signal from the cylinder was generated as a superposition of signals from overlapping spherical sources. The maximum amplitude of the PA signal from the cylinder was taken as twice the amplitude of the spherical source. This corresponds to an absorption coefficient for the cylinder about 10-fold lower than for the sphere. Random noise was added to the data-set. The noise had an amplitude standard deviation equal to the amplitude of the cylindrical source. An image reconstructed from this data-set should represent the efficiency of the reconstruction methods in the presence of noise and multiple PA source structures.

5.2.2 Image reconstruction algorithms

The basic task of image reconstruction is to find the initial pressure distribution from the pressure transients detected in the detector plane. Since in soft tissue, the variation of optical absorption is much higher than the small variation of acoustic impedance, the medium is assumed to be acoustically homogeneous, nondispersive and isotropic.

Fourier transform based backward projection algorithm
A complete derivation of the Fourier transform based backward projection image reconstruction algorithm (Kostli *et al.* , 2001) and application for the two-dimensional situation (Kostli & Beard, 2003) were reported earlier. In this method the three-dimensional matrix of ultrasound signals measured in

[2]Resolution of the instrument or method is the minimal distance between two objects at which these still can be distinguished

a detector plane is transformed into Fourier space:

$$p(x, y, t)|_{z=0} \Rightarrow \mathbb{F}^{+} \Rightarrow P(k_x, k_y, \omega) \tag{5.2}$$

where x, y and z are Cartesian coordinates, k_x and k_y are spatial frequencies, ω is the angular frequency, and $p(x, y, t)|_{z=0}$ is a pressure transient measured by a detector at position (x, y) in plane $z = 0$. The direct 3-D Fourier transform is assigned as $\mathbb{F}^{+}$.
Then using the relation between the angular frequency and all three spatial frequencies,

$$\omega = +c\sqrt{k_x^2 + k_y^2 + k_z^2} \tag{5.3}$$

the data-set dependence on the angular frequency is transformed to the dependence on the third spatial frequency k_z

$$P(k_x, k_y, \underline{\omega}) \Rightarrow P(k_x, k_y, \underline{k_z}) \tag{5.4}$$

The obtained data-set $P(k_x, k_y, k_z)$ is the Fourier space image of the initial pressure distribution which is now expressed as:

$$P(k_x, k_y, k_z) \Rightarrow \mathbb{F}^{-} \Rightarrow p(x, y, z)|_{t=0} \tag{5.5}$$

where $\mathbb{F}^{-}$ is the inverse 3-D Fourier transform.

It is worth mentioning here that the utilization of Fourier transforms inevitably leads to mirroring of images and subsequently to doubling of the data-set size.

The utilization of a Fast Fourier Transform (FFT) subroutine in the described algorithm requires some preprocessing of the input data-set. Firstly, the depth location of the imaged object is restricted to half of the lateral size of the detector matrix. In this case padding of the input data-set by zero detector positions allow the reconstruction of the image from a larger depth. Secondly, the voxel[3] size of the image reconstructed with this algorithm is determined by the parameters of the input data-set. The axial resolution is equal to the time signal sampling interval multiplied by the speed of sound. Since the time sampling interval is the prior chosen parameter, the axial resolution can be varied.
In the MATLAB routine used the size of the output image is equal to the size of input matrix. Therefore, the lateral resolution provided by direct reconstruction is limited by the detector matrix inter-element spacing.

[3] voxel is (by analogy with "pixel") volume element

However, the lateral resolution is defined by properties of the single detector and the viewing angle to the imaged object. This can be estimated as (Oraevsky *et al.* , 1999):

$$\delta = \frac{\lambda_{a,c}}{L} l \tag{5.6}$$

where δ is the resolution, L is the lateral size of the array, l is the distance from the array to the object, and $\lambda_{a,c}$ is the wavelength of the acoustic transient generated by the object. In the configuration considered here the resolution is limited to 1.5 times the size of the imaged object bigger than 0.2 millimeters in diameter. The limitation is defined by the chosen detection sampling rate. Thus the data necessary for reconstruction of high resolution image is already present in the measured signals, but has to be projected back (equation 5.4) to a higher sampling frequency space matrix. This can be achieved by lateral upsampling[4] of the input data-set. Physically this is equivalent to the insertion of phantom detectors[5] in between detectors providing nonzero signals, either measured or simulated.

Insertion of phantom detectors leads physically to the following: first, it reduces the density of the acoustic wave energy received by each detector in the matrix. Therefore such a matrix extension homogeneously reduces the image amplitude proportionally to the ratio of nonzero signals to the total number of detectors in the matrix. Second, the signal-to-noise ratio (SNR) of images reconstructed from noisy data is expected to be reduced as well.

To eliminate these negative consequences, the reconstruction of signals from real detectors is desired instead of the insertion of phantom detectors. However exact reconstruction taking into account generation and propagation of acoustic waves is complicated and time consuming. For this a purpose three-dimensional cubic spline interpolation was used. This algorithm does not take into account the physics of the processes but is expected to reconstruct its geometrical non-linearity. The results of reconstruction from upsampled and interpolated data-sets have to be compared. An increase of the input data-set size directly leads to increasing computational requirements.

Based on the simulated setup configuration, direct reconstruction from the generated data-set is expected to result in images with a lateral resolution of 3 mm. Since sources smaller than 3 mm are simulated, a higher resolution is required. To obtain 1 mm lateral resolution two phantom detectors should be inserted between two non-zero detectors. This means that

[4]insertion of a zero sample between each two samples of the original signal

[5]detectors which measure zeros

the size of the two-dimensional data-set is increased by a factor of 9 with a consequent proportional increase in computational requirements. To check the effect of zero filling, reconstruction results of both direct and expanded input are analyzed. The direct reconstruction and that from a data-set up-sampled by zeros are denoted as "Fourier Method 1" and "Fourier Method 2" respectively. In order to be compared, the reconstructions from the two data-sets should be presented in grid with the same voxel size. A three-dimensional cubic spline interpolation to lateral voxel size 1×1 mm, was applied to the image reconstructed by Fourier method 1. The results of the reconstruction from the data-set expanded by cubic spline interpolation will be considered shortly.

Delay-and-Sum beamforming algorithm

The delay-and-sum beamforming algorithm (Hoelen *et al.* , 1998), (Hoelen & de Mul, 2000) applies the phase-array approach to algorithmically focus the sensitivity of the detectors in a planar matrix to single voxels or focii into which the investigated bulk volume is assumed to be divided. The signal from each voxel of the imaged volume is expressed as,

$$S^f(t) = \frac{\sum_i^M w_i^f S_i(t + \tau_i^f)}{M} \tag{5.7}$$

where $S_f(t)$ is the signal from f^{th} focus; $S_i(t)$ is the signal from i^{th} detector; τ_i^f is the time delay of the f^{th} focus to the i^{th} detector; w_i^f is the weightfactor of f^{th} focus to i^{th} detector; M is the number of detectors. The weightfactor in equation 5.7 is the directional sensitivity of the detector for pulsed signals. The time delay is found from the relation

$$t = v^{-1}|\vec{r}| = v^{-1}\sqrt{x^2 + y^2 + z^2} \tag{5.8}$$

The result of the focus scanning over the imaged volume is a back projection of the pressure waves measured over the detector matrix area into the object volume. Then the initial pressure distribution must be reconstructed.
Summing up the backward projection by calculation of peak-to-peak[6] values within a window sliding along the signal trace yields an inexact reconstruction (see figure 5.3(middle)). In spite of its approximate nature this method can provide a detection of the position of absorption maxima and was successfully applied before (Hoelen *et al.* , 2001), (Pilatou *et al.* , 2003), (Manohar *et al.* , 2004). Since the propagating pressure transient is the

[6]In case of an ideal bipolar signal the difference between positive and negative peaks (peak-to-peak value) is proportional to the strength of the acoustic source

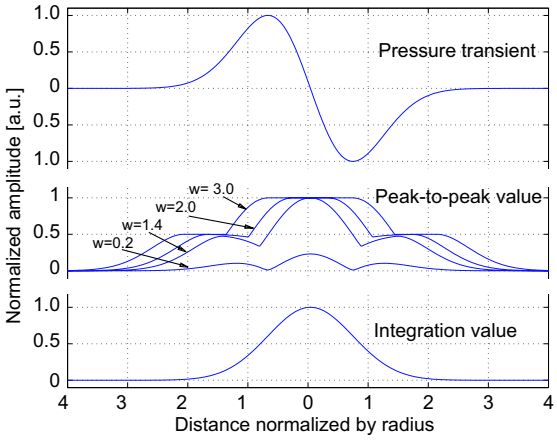

Figure 5.3: A pressure transient (top) and results of its reconstruction from back projection calculated by: (middle) taking the peak-to-peak value within differently sized windows (w) and (bottom) integrating over distance

derivative of the initial pressure distribution (see figure 5.2) the latter can be obtained by integration of the backprojected signal (see figure 5.3(bottom)). In this method, no manually chosen parameter is used and therefore prior knowledge about the imaged structure is not required.

DNS signal backprojection by calculation of peak-to-peak values and integration of backprojected signals were evaluated. These methods are denoted as "DNS Method 1" and "DNS Method 2", respectively.

5.3 Results and Discussion

5.3.1 Single source study

Images of simulated spherical objects with diameters from 1 to 12 mm were reconstructed using the above described methods. The dimensions of reconstructed objects were defined at various threshold levels such as $1/e$ of the maximum intensity. Results are presented in figure 5.4.
The window size for DNS method 1 (see figure 5.4(c)) was taken equal to the depth of one voxel, i.e 1 mm.

The results showed that in all cases, excluding DNS method 1, estimation of dimensions with thresholding at level of $1/e$ of the maximum yielded unequal lateral and axial (depth) dimensions. This difference can be predicted from the estimation of the lateral and axial focus size of the planar detector array, the characteristics of the array and setup configuration. (Oraevsky *et al.* , 1999). All methods exhibited an increased lateral size of images at an $1/e$ threshold by a factor of at least two, although the expected focus

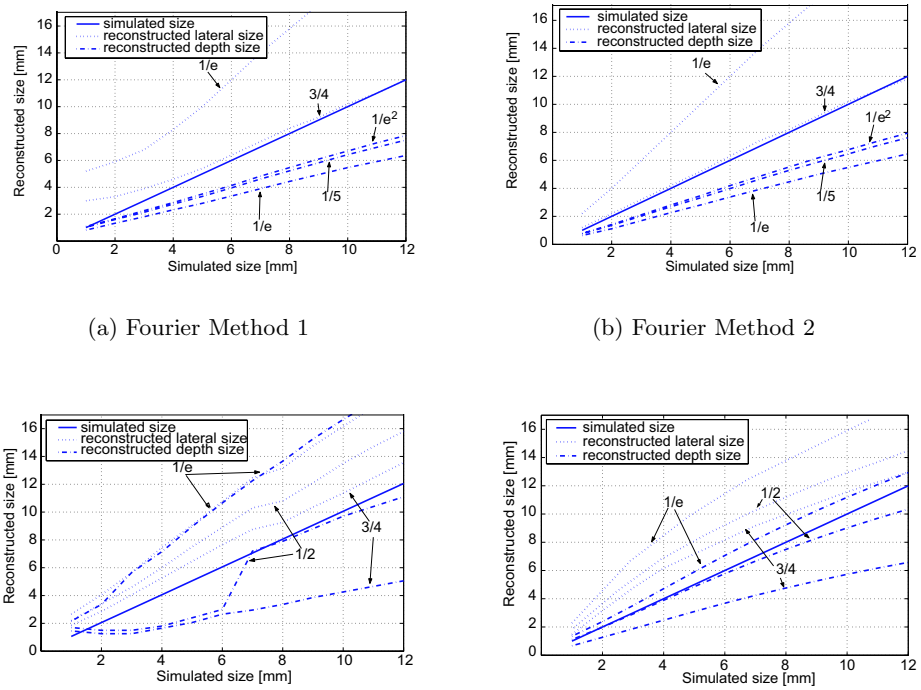

(a) Fourier Method 1

(b) Fourier Method 2

(c) DNS Method 1 algorithm

(d) DNS Method 2 algorithm

Figure 5.4: Comparison of lateral and depth sizes of reconstructed objects with simulated (i.e."real") parameters

size is 1.5 times the diameter of the object. As expected, Fourier method 1 is incapable of correctly reconstructing the lateral size of objects smaller than the inter-element spacing of the detector matrix (in our case 3 mm). In the reconstruction of objects with a size much larger than the matrix inter-element spacing Fourier method 1 and method 2 provided identical results.

The axial size of objects reconstructed by both Fourier transform methods, even at a rather low threshold level, i.e. $1/e^2$, was smaller than the simulated object sizes. Object axial sizes from DNS backprojected signals with peak-to-peak value summation, did not have a fixed dependence on the simulated size. Integration of DNS backprojected signals provided the best definition of the axial size of imaged objects.

To prove that for large objects the insertion of phantom detectors does

not change the results of reconstruction apart from a proportional reduction of the image amplitude, reconstructions of various size objects by the two Fourier transform based methods were analyzed. The maximum value (I_m) in the reconstructed image as a function of simulated object size is plotted in figure 5.5(a). Figure 5.5(b) shows the ratio of the maximum value (I_m) and RMS value of the entire image. The predicted 9 times difference in image

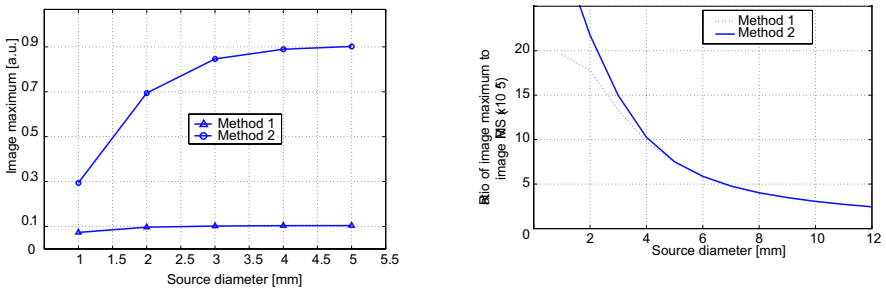

(a) (b)

Figure 5.5: Dependence of maximum value I_m of images, reconstructed by Fourier transform based algorithms, on size of initial object - (a), and ratio of image maximum to the RMS value of the entire image - (b)

amplitude was observed for simulated object sizes larger than the detector matrix inter-element spacing, which is in this study equal to 3 mm. At a smaller object size, the maximum of the image reconstructed using Fourier method 1 decreases due to the effective averaging of the source amplitude over the volume of a voxel which is larger than the source volume in this region.
The observed equality of the ratio of the image maximum to the image RMS value (see figure 5.5(b)) proves that the amplitude of each image point is reduced homogeneously for objects larger than the inter-element spacing.

The amplitude of signals of simulated data-sets was normalized. Therefore the maximum amplitude of reconstructed images remains constant, apart from the region of spheres diameter smaller than 3 mm. Since the RMS value of ideally reconstructed images should be proportional to the volume of the reconstructed object, the ratio of the image maximum to the image RMS value decreases with increasing simulated object size (see figure 5.5(b)).

Figure 5.6 shows a comparison of the object lateral size defined from images reconstructed in three different ways: direct reconstruction from the simulated data-set; reconstruction from the data-set upsampled by zeros,

and reconstruction from the data-set expanded by three-dimensional cubic spline interpolation.

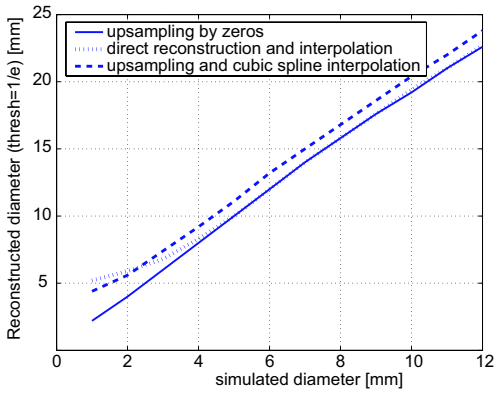

Figure 5.6: The comparison of lateral size of objects reconstructed from upsampled, interpolated and unchanged (direct) simulated data-set with inter-element spacing of 3 mm

It is seen that the curve obtained from images reconstructed from the interpolated data-set is linearly shifted up from the result of reconstruction from the data-set upsampled by zeros. This can indicate only that the used interpolation method cannot correctly reconstruct signals from inserted phantom detectors in the considered configuration.

The development of an algorithm for reconstruction of missed signals to the upsampled data-set is beyond the scope of this study. Therefore the image reconstruction by Fourier method from the data-set expanded by not measured but reconstructed signals is not considered.

5.3.2 Multiple source study

To study the performance of image reconstruction algorithms in conditions closer to the real images were reconstructed from noisy data-sets. Analyzing results of the reconstruction it was found that in some cases extra denoising of the output image can improve image SNR.

The output images of Fourier method 2 (see figure 5.7(a)) contain a high frequency noise that can be regarded as similar to shot noise, i.e. some single voxels have much higher amplitude than their neighborhood. To suppress such kind of noise, median filtering (Pitas, 2000) can effectively be applied. When performing median filtering, each voxel is determined by the median value of all voxels in a selected window.

A result of lateral two-dimensional median filtering with a window size of 4 voxels, presented in figure 5.7(b), shows an increase of the image SNR

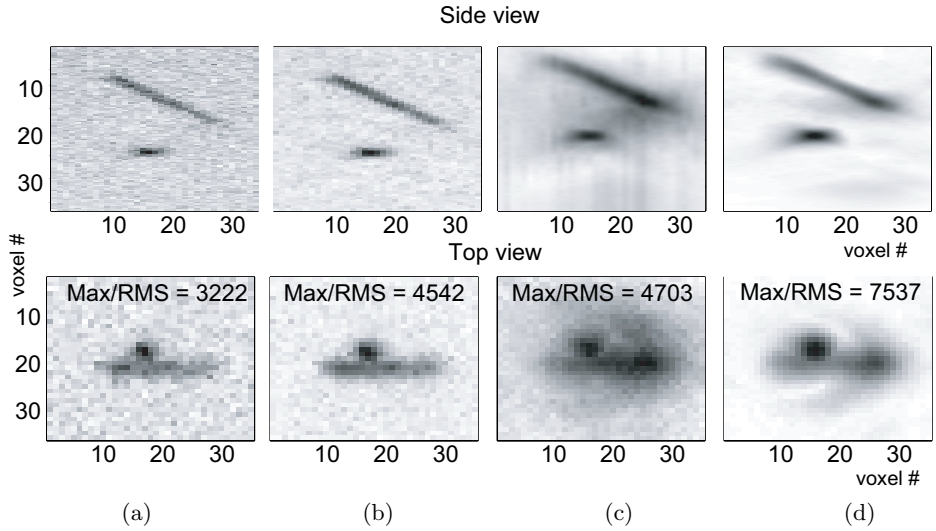

Figure 5.7: Example results of extra denoising applied to rough outputs of image reconstruction algorithms. (a) - rough output image of Fourier method 2; (b) - the same image after lateral two-dimensional median filtering with window size of 4x4 millimeters; (c) - rough output of DNS method 2; and (d) - image obtained after low frequency filtering.

by a factor of 1.5. This is due to the effect of the homogenization of the noise background with consequent amplitude reduction of spike-like isolated voxels.

After back projection to the object space, the spatial mean value of the signals found is set to zero. However the mean value of a fragment of this signal can differ from zero, especially if noise was present. Therefore integration in depth of such signal results in a low frequency noisy background, that can be seen in figure 5.7(c). This noisy background can be effectively reduced by filtering out low frequency content of the obtained image, in the same direction as the integration was applied. To avoid losing image details, the spatial cut off frequency has been taken to correspond to the axial object size of more than 7 mm which is twice the axial size of reconstructed objects which can be found already from the rough image. The result of filtering presented in figure 5.7(d) shows a decreasing of the noise background level by a factor of 1.6.

Application of median filtering and low frequency filtering to output

images from the other considered methods does not result in any noticeable changes of the image quality. In view of this the above mentioned noise reduction procedures were included in two image reconstruction procedures. This means that from now on Fourier method 1 is supplemented by median filtering, and DNS method 2 is supplemented by low frequency filtering.

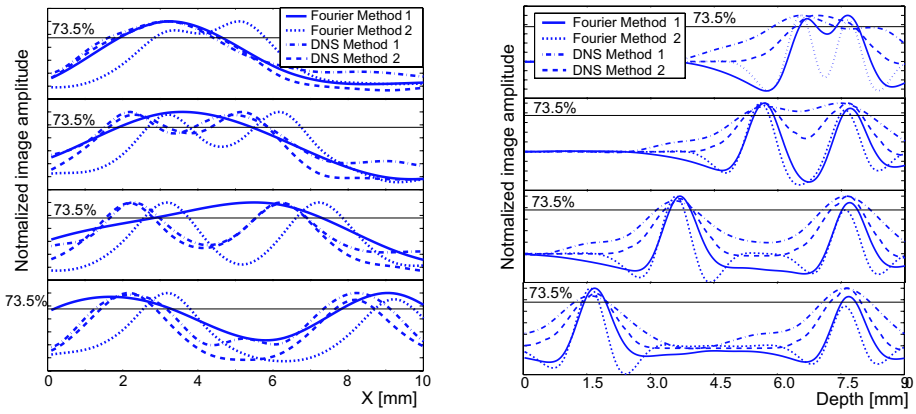

(a) (b)

Figure 5.8: Lateral and axial resolution of four reconstructions of two spherical sources of 1 mm diameter. Top panel contains side view, bottom panel - top view. (a) - The reconstructed lateral profile, center-to-center spacing is 2 mm (top), 3, 4 and 6 mm (bottom); (b) - the reconstructed axial profile, center-to-center spacing is 1 mm (top), 2,4 and 6 mm (bottom).

To find axial and lateral resolutions from each method, image reconstructions from the second data-set (see page 85) were performed. Figure 5.8 shows a number of single lines from reconstructed 3-D images of the different center-to-center sphere spacings. The results have been spline interpolated to a 10 times smaller space step than reconstructed images, i.e. the space sampling frequency in figure 5.8 is 0.1 mm.

Since photoacoustic signals from multiple object structures can be presented as a superposition of signals from spherical sources, the reconstructed image is also expected to be a superposition of images from spherical sources. If this is valid, then following Sparrow's criterion (Sparrow, 1916) two peaks are distinguishable when the dip between maxima is less than half of the peaks amplitude. In our case this means that the distance between two spheres should be equal to or more than the object diameter at 1/4 of maximum, as can be found from a single source study.

Figure 5.8 presents a particular case with 1 mm diameter objects. As

expected, distances at which the dip between two maxima has the amplitude less then 73.5%[7] of the maxima have a good agreement with the size of objects at level of $1/e$ of the maximum, presented in figure 5.4. Therefore results of a single source study can be used to find resolution of image reconstruction of methods.

The performance of algorithms in the situation close to reality was evaluated from the reconstruction of multiple objects from a noisy data-set (see p. 85). When a noisy background is present, the ratio of the image maximum to RMS value is a measure of the signal-to-noise (SNR) ratio.

Images reconstructed from the noisy data-set by the four considered methods are presented in figure 5.9.

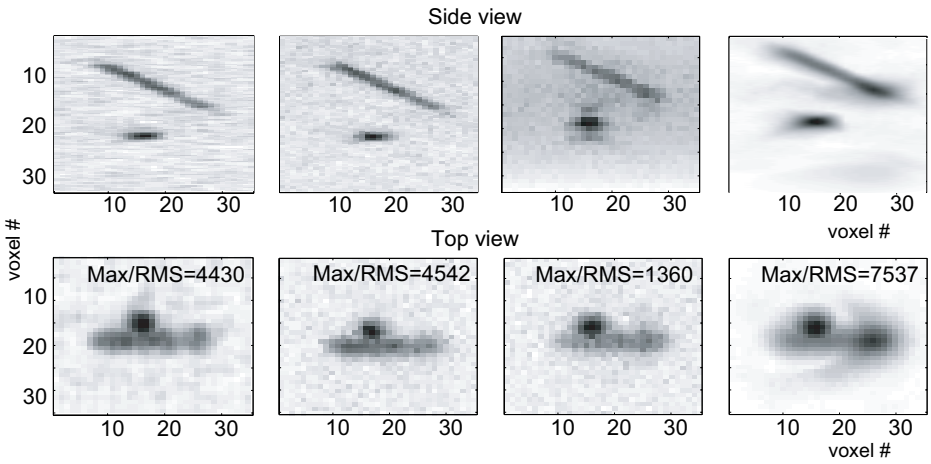

Figure 5.9: Images of tilted cylinder and sphere reconstructed by different methods from the randomly noised data-set. (a) and (b) - Fourier transform based method 1 and method 2 with extra median filtering respectively; (c) and (d) - DNS backprojection method 1 and method 2 with extra low-frequency filtering respectively

The obtained images are visually rather identical. The relative size and position of the imaged spherical and cylindrical absorbers can be fairly well depicted from any obtained image. The artifacts of DNS reconstruction method 1 are almost hidden by background noise. DNS method 2 with low frequency filtering provides an approximately two times better SNR

[7] 1/e+1/e=0.735

than other methods. Images of the cylindrical object have a variation of amplitude of 30 % over the object length.

It is worth mentioning that Fourier method 1 with spline interpolation and Fourier method 2 with median filtering have produced images with equal SNR. Nevertheless the resolution of Fourier method 2 is still higher.

5.3.3 Computational requirements

As mentioned earlier, the computational time and amount of memory required for calculation are important aspects in the choice of an image reconstruction algorithm. In table 5.1 computational requirements are presented for comparison.

Table 5.1: Comparative computational requirements of four image reconstruction algorithms implemented in MATLAB version 6.5 Release 13.

Algorithm	Fourier Method 1	Fourier Method 2	DNS Method 1	DNS Method 2
Computational time[a] (*sec.*)	11	109	1557	1630
Memory usage[b] at least	67kB×8/n[c]	67kB ×8	67kB	67kB

[a] - calculation was performed on Athlon64+ 2.5 GHz based PC system.

[b] - this parameter does not show the total amount of used memory but the minimum required amount only

[c] - n is the ratio of the total number of detectors to the number of nonzero detectors

The Fourier transform based high resolution reconstruction requires one order of magnitude less time than time domain backprojection methods. However, the memory usage is almost one order of magnitude higher. This is explained by the nature of the Fourier transform i.e. the necessity to operate with complex variables and mirroring of the data-set. Besides, in the considered configuration, to get the desired resolution the size of input data-set was extended to the size of output image in the desired resolution. This is not required in the time-domain computation.

Use of the Hartley transform (Brigham, 1999) which is equivalent to the Fourier transform but produces real output, can reduce memory requirements by a factor of two.

5.3.4 Image reconstruction from measured signals

The final step of this comparison study is the reconstruction of images of the solid phantom embedded with tumor simulating inserts (see chapter 2). A data-set obtained from the evaluation study of the PA mammoscope

prototype was used (see chapter 4). The chosen volume of interest (VOI) contained a 2 mm sized sphere with an absorption contrast of 4, at a depth of 15 mm from the surface. Images reconstructed by the four considered methods are presented in figure 5.10.

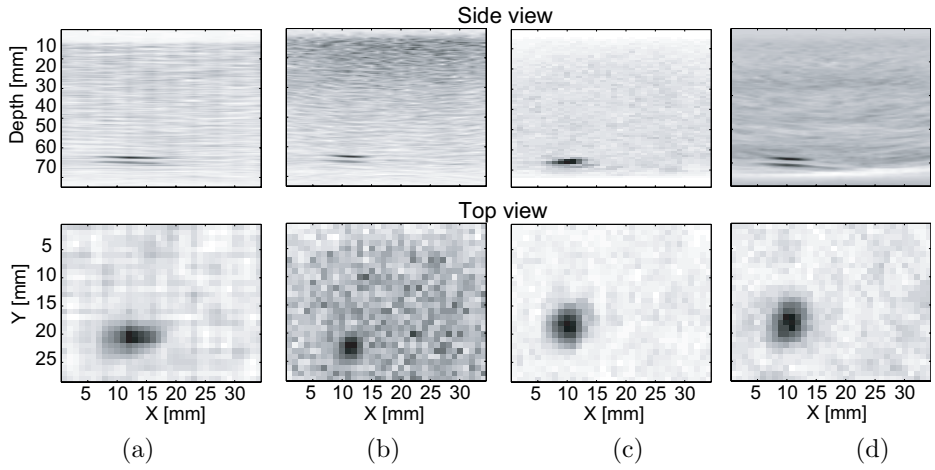

Figure 5.10: The image of the solid phantom absorbing insert. VOI contains 2 mm sized sphere with an absorption contrast of 4, at depth of 15 mm from illuminated surface. (a) and (b) - Fourier method 1 and 2, respectively; (c) and (d) - DNS method 1 and method 2, respectively

Although the quality of images is still comparable, the results differ from those obtained from the study on simulated signals (see figure 5.9). In particular: DNS method 1 has provided the best image clarity; the image reconstructed by Fourier method 2 is contaminated by noise, that decreases with increasing distance from the detector plane.

The results (see figure 5.10 side view) show that the axial profile of the reconstructed insert does not correspond to its real axial profile. Double peaks were observed in three of four reconstructed images, instead of an expected single peak. The fact that the DNS method 1 output image has a single peak axial profile likely proves that with chosen size of window the DNS method 1 provided a poorer axial resolution than the other considered methods.

Investigation of reasons causing image doubling lies beyond the scope of this chapter. However it is likely to be a lack of low frequency components in the recorded PA signal. This can, in turn, be explained by a mismatch of the

detection frequency band of the detector matrix and the frequency content of the generated signal.

5.4 Conclusion

The performance of Fourier transform based and Delay-and-sum image reconstruction algorithms has been compared numerically on data-sets simulating measured signals from a setup based on a planar rectangular detector matrix, and on a measured data-set. Two modifications of each method were studied. Based on the obtained results the following conclusions are drawn.

Fourier method 1 has shown the highest calculation speed. The lateral resolution of images reconstructed by Fourier method 1 is limited by detector matrix inter-element spacing. In the considered configuration direct reconstruction can be used for a fast, rough determination of the "volume of interest" i.e. an area of increased optical absorption.

Fourier method 2 reconstructed the image of the simulated structure slower than Fourier method 1 since it has to process larger data-set. Compared to Fourier method 1, Fourier method 2 provides better lateral resolution of objects smaller than the matrix inter-element spacing. The main disadvantage of this method is that one requires a larger amount of memory.

The depth size of objects reconstructed by both Fourier transform based methods, even at a rather low threshold level of $1/e^2$, was smaller than simulated object sizes.

DNS method 1 does not provide a correct reconstruction of the shape of the initial pressure distribution but still holds the abilty to detect the position of absorbers. With this method prior knowledge about the imaged structure is required. Axial sizes of objects reconstructed by DNS method 1 did not have a fixed dependence on the simulated size.

DNS method 2 utilizes an integration of backprojected signals for reconstruction of initial pressure distributions. This method does not require any prior knowledge about the imaged absorbing structure. DNS method 2 provided the best definition of the depth size of imaged objects.

All considered methods showed an increase of the lateral size of objects at $1/e$ threshold by a factor of at least two, although the expected focus size is 1.5 times the size of the object.
The compared methods provide a fairly equal quality of images reconstructed from noisy data. In all four cases the SNR was in the same order of magnitude.

The DNS method 1 provided best SNR of the image reconstructed from the experimentally recorded data-set.

Fourier transform based methods are favored for reconstruction of absorber structure from PA signals when the much shorter calculation time is essential. However additional investigation is required to study reasons of the observed thinning of the absorber. Compared to time domain reconstruction, the memory usage of Fourier transform based method is approximately eight times higher.

The reconstruction of an image from the upsampled and recovered dataset is expected to provide the same resolution as reconstruction from a dataset upsampled by zeros without having a problem with reduction of the image amplitude and SNR. However the reconstruction of signals from phantom detectors can be rather complicated and much more time consuming than image reconstruction by Fourier transform based backward projection algorithms. Further study is required to estimate the efficacy advisability of this procedure.

Chapter 6

Conclusion and prospects

6.1 Conclusion

The purpose of the present work was to study and develop a photoacoustic mammograph (PAM) and to perform a laboratory study of the feasibility of photoacoustic breast tumor detection. This consisted of laboratory testing of instrument parts, of development of a solid phantom mimicking optical and acoustic properties of breast tissue, and of design of a clinical prototype of the PAM. Finally, the performance characteristics of the developed PAM prototype were determined from the phantom measurements.

New materials for solid breast phantoms intended for use in photoacoustics, based on poly(vinyl alcohol) (PVA) hydrogels were presented in chapter 2. These are the only available phantoms mimicking both optical and acoustic properties of tissue. To realize the optical properties of tissue, one approach was to optimize the number of freezing and thawing cycles of aqueous poly(vinyl alcohol) solutions, a procedure which increases the turbidity of the gel while rigidifying it. The second approach concentrated on forming a clear matrix of the rigid poly(vinyl alcohol) gel without any scattering, so that appropriate amounts of optical scatterers could be added extraneously at the time of formation, to achieve tunability of optical properties as per requirement. The optical and acoustic properties relevant to photoacoustic studies of such samples were measured to be close to the average properties of human breast tissue. Tumor simulating gel samples of suitable absorption levels were created by adding appropriate quantities of dye at the time of formation; the samples were then cut into spheres.

A breast phantom embedded with absorbing inserts was developed for studying the applicability of photoacoustics in mammography. The PVA

gel prepared in the first method was utilized to simulate bulk breast tissue. The reason to choose this method was that optical properties of the phantom can be adjusted by changing the number of freeze-thaw cycles, and no extra scatterers are required.

The performance of the ultrasound detector matrix intended to be used in the first prototype of the PAM was studied in chapter 3. The detection frequency band is quoted as from 0.45 to 1.78 MHz with a maximum sensitivity at 1 MHz. The sensitivity and minimum detectable pressure were measured as 94 μV/Pa and 100 Pa, respectively. The lateral size of the point-spread-function of the ultrasound detector in combination with the image reconstruction algorithm was found to be 3.1 mm. Based on these findings the considered acoustic detector matrix used was found to be suitable to study the feasibility of PA breast cancer tumor detection.

The first prototype PAM operating in the parallel plate geometry was presented in chapter 4. This instrument is intended for initial retrospective clinical studies on subjects with breast tumors. The envisaged investigation procedure is the following:
- the subject lies prone on the bed with her breast pendant through the aperture to the measuring unit. The breast is mildly compressed between detection and illumination compartments. Compression is required to obtain a uniform thickness of the breast and a good acoustic contact with the detector. Therefore this procedure is not expected to be painful.
- pulsed NIR light from an Nd:YAG laser impinges on the breast through the glass plate in regions of interest. The utilization of NIR light below the safety threshold implies that the investigation procedure should be risk-free.
- generated pressure transients are detected by an appropriate number of elements of the detector matrix activated in succession to record photoacoustic signals.
- recorded signals are acquired by a PC and images of the tissue absorption are reconstructed.

The developed PAM prototype is capable of imaging inhomogeneities of absorption contrast 7, down to 30 mm depth, and inhomogeneities of absorption contrast 2, down to 15 mm depth in well characterized phantoms, using laser fluences at the surface conforming to the Maximum Permissible Exposure threshold for the specifications of the light used.

In order to achieve deep imaging with reasonable signal-to-noise ratios it was found necessary to average the individual element signals upto 100 times. Additionally only one element can be accessed at a time. These two factors in the combination with the laser pulse repetition rate lead to

a rather long patient contact time[1] required to image the chosen volume of interest. We have set the maximum acceptable measuring time to 45 minutes, which permits an area of 52×52 mm to be scanned with averaging of 100 signals and a pulse repetition rate of 10 Hz. Though this time is long for routine clinical examinations, it is admissible for the first human subject tests.

The patient acceptance of this period is highly subjective but will depend on the quality of the patient-instrument interface. This has been the rationale behind the choice of the interface where the patient lies prone on a bed with the scanner beneath.

A comparative performance study of two image reconstruction algorithms is presented in chapter 5. A frequency-domain algorithm and a time domain delay-and-sum beam-focusing algorithm are considered.
It was quantitatively shown that reconstructions performed using the Fourier transform approach were at least 10 times faster than the corresponding time domain reconstruction but were limited in resolution by the detector matrix inter-element spacing. It was found that the lateral resolution could be improved by a spatial upsampling of the input data-set for the Fourier transform based algorithm, but this procedure leads to increased computational requirements.
Both methods provide fairly equal quality of the reconstructed image. The availability of the Fast Fourier Transform (FFT) makes the Fourier transform based method favorable for reconstructions. However its higher memory usage can be a serious complication in some configurations.

6.2 Healthy volunteer measurements

In preparation for the intended clinical trials, measurements on the breasts of two healthy volunteers were conducted using the instrument. The aims of this exercise were:
- to obtain feedback from the volunteers regarding comfort aspects of the patient-instrument interface, and solicit suggestions for improvements;
- to test the imaging protocol designed for the proposed clinical measurements;
- to generally obtain breast images.

It must be mentioned here that since the volunteers were not imaged using any conventional imaging techniques for comparison, the quality of the images provided by the PAM cannot be evaluated from these measurements.

[1] time required to position the measuring unit of PAM and perform imaging

The purpose of the measurements was rather to see if optical absorption inhomogeneities, for instance blood vessels, which are expected to be present in the breast could be recognized in images obtained.

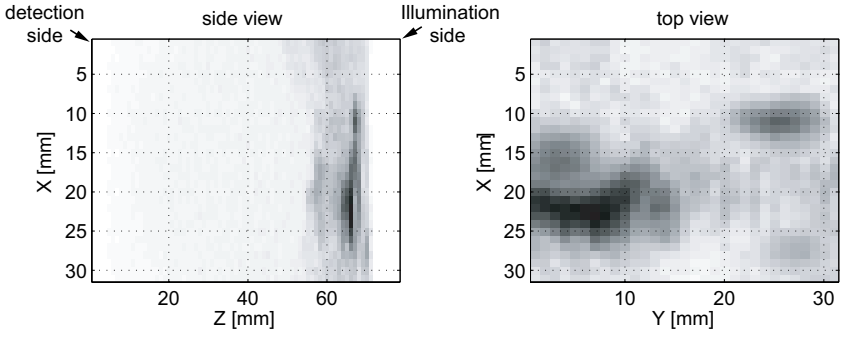

(a)

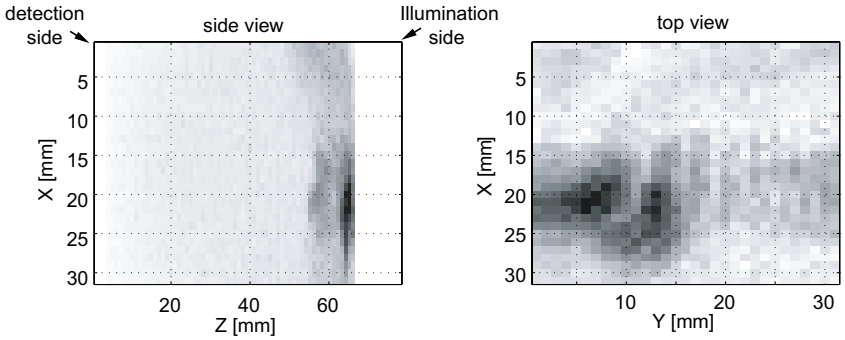

(b)

Figure 6.1: PA images of a randomly chosen breast volume of the healthy volunteer: (a) reconstructed from the data-set with signals from the surface and the top 5 mm tissue set to zero; (b) reconstructed from data-set with signals from the surface and the top 8 mm tissue set to zero;

Two healthy volunteers participated in this study. For each volunteer a randomly chosen breast volume with a surface area of 35×35 cm^2 was imaged. This surface area was defined by the chosen measurement time limit of 25 minutes. This is less than the imaging time of 45 minutes proposed for the clinical trials. Generated acoustic transients were measured over the square region defined by 11×11 detectors. signals from each detector were averaged 128 times.
The illumination beam diameter was 16 mm. The total pulse energy was 65

mJ/pulse, yielding an exposure equal to the maximum permissible exposure (IEC 60825-1) of 30 mJ/pulse/cm^2.

In figure 6.1 two sets of images from one volunteer are presented. From these images an absorbing structure, presumably a large blood vessel can be identified at depth of 5 to 10 mm within measured volume. The large signal arising from the surface and top layer of tissue was masked in reconstructions; inclusion of this signal otherwise results in the deterioration of deeper lying structures.
The measurement results, allow us to conclude that the developed PAM prototype can image an absorption inhomogeneity of the breast. As expected, due to unequal illumination the superficial and low depth absorbers generate much higher signals. Therefore, to reconstruct images of deeper located absorbers signals from the surface and low depth structures have to be set to zero.

Feedback from volunteers revealed that the experience was not uncomfortable. Recommendations for a few minor changes were incorporated into the final version of the mammoscope and the design of the imaging protocol (Sterenborg *et al.* , 2004).

6.3 Prospects for future works

6.3.1 Clinical pilot study

A pilot study is the next step of this ongoing research. The aims of this pilot study, are:
- to evaluate the feasibility of the PA technique to detect breast tumors in subjects with diagnosed lesions and later in subjects with suspected lesions.
- to understand the correspondence between PA images and tumor features, by comparison of findings of conventional techniques with PA images.
The aim of the next clinical phase is to define whether the PA technique detects a lethal phenotype of a tumor only. This assumption is based on the fact that the PA technique "looks" for the angiogenic signature that is typical for an invasive tumor (Folkman, 2000).

6.3.2 Equipment improvements

To become a widely used tool for breast cancer detection the technique is desired to be inexpensive, compact and capable of providing a real time high-resolution monitoring of the medium of interest distributed over the investigated body.

Dependent on the use for detection or diagnosis different variations of the PA imager can be of interest. The use of photoacoustics for detecting suspect lesions would require an imaging system capable of providing a high-resolution image of the entire breast. For this purpose a short patient contact time is desired. However the total size of the system is not strongly limited.
An imaging system capable of providing high-resolution 3-D images of a limited volume or 2-D images of tissue slices, like conventional ultrasound equipment, may be required in the stage of profound investigation of suspicious cases.

The capabilities of the realized first PAM clinical prototype realized in this work are sufficient to study the feasibility of PA breast tumor detection. Some parameters of the developed instrument have been dictated by component availability rather than by most efficient performance. Following generations of the PAM can be significantly improved based on the experience obtained from the performed laboratory and initial clinical study.

Total measurement time

The presented PAM prototype requires an acquisition time of 20 minutes for imaging an object volume with a surface area of 30×30 mm. This is dictated by characteristics of the ultrasound detector matrix: the ability to only read out one element at a time and the high level of noise equivalent pressure of a single element compared to the amplitude of generated acoustic transients.

Potentially PA imaging can be performed in "one shot". To achieve this the entire investigated volume has to be illuminated at once and then generated acoustic transients have to be recorded simultaneously from a sufficient number of surface positions to reconstruct the initial pressure distribution.

An increase of illuminated area demands a higher total excitation radiation energy. Since the maximum permissible exposure for repetitious pulsed NIR light is 30 mJ/pulse/cm^2 (IEC 60825-1) a total pulse energy of 3 J would be required to illuminate the surface area of 10×10 cm^2. Such lasers are not easily available yet. However the fact that the optical absorption of blood predominates over that of bloodless tissue in a wide wavelength range allows the use a wide band light sources. Thus, besids high power laser systems pulsed sources of incoherent light can be also of interest for PA imaging.
Beside the generation of high energy pulses the delivery of light to the surface of the investigated object can be complicated. Taking this into account, increasing the sensitivity of acoustic detectors can be more advantageous for

improving the sensitivity. Firstly, this allow avoiding signal averaging over a big number of records. For instance, utilization of 10 times more sensitive detectors allow obtaining the same results as presented in this work but 100 times faster. In practice, even a higher increase of the sensitivity is feasible (Esenaliev *et al.* , 1999). Secondly, use of highly-sensitive detectors allows either imaging of absorbers from larger depth at constant pulse energy of the excitation radiation, or reduction of the pulse energy for a constant imaging depth.

Reading out a number of elements from the detector matrix at a time is required to record the acoustic transient simultaneously from a number of surface positions. The detector matrix used in this study allow to access only one element at a time. However this can be modified, and up to 10 elements at a time can be read out simultaneously (Molenaar, 2005).

Measurement geometry

The parallel plane geometry adopted for the developed PAM was chosen to be able to compare breast interior images which would be obtained with PA technique to images provided by conventional X-ray mammography systems and optical mammographs being developed elsewhere (Grosenick *et al.* , 1999). This would allow to define the accuracy of detection. The main disadvantage in this geometry is that the spatial resolution of the imager is limited by the lateral size of the detector and the critical angle for the tissue - detector material interface. This can be eliminated by use of a detector array of arc (Andreev *et al.* , 2000), cylindrical or hemispherical shape (Kruger *et al.* , 1999b). In these geometries the viewing angle to the object can reach 180 degree without having a problem with acoustic interference over the detector surface, and then the lateral resolution will be defined by the frequency band of the individual detector.

As mentioned earlier, it is rather complicated to manufacture a piezoelectric detector with a wide uniform frequency response. It means that the range of correctly detectable object sizes will be limited. However, implementation of a detector matrix consisting of several overlapping sets of detectors with different thicknesses of the active element and therefore having different central frequencies, is one of the ways to widen the detectable object size range. In this case images with different resolution will be reconstructed from sets of data acquired from various sets of detectors.

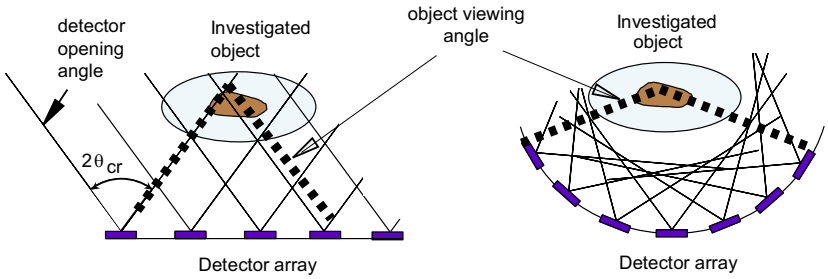

Figure 6.2: Limitation of the opening angle in different detection geometries

Wavelength of excitation radiation

The presented instrument has adopted an optical excitation wavelength of 1064 nm. All relevant parameters were studied at this wavelength. However the wavelength range from 690 to 800 can also be of interest for PA imaging due to low light attenuation by soft tissue (Spinelli *et al.* , 2004).

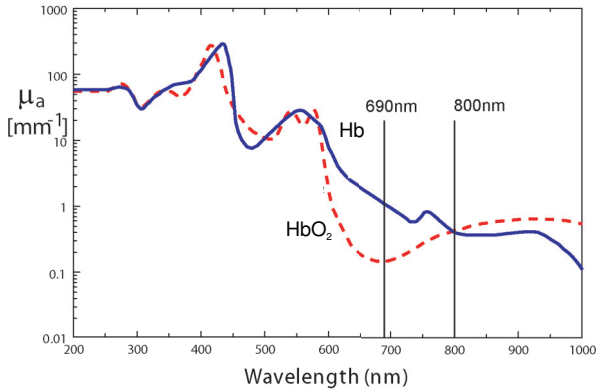

Figure 6.3: Optical absorption of oxygenated and deoxygenated blood

Beside tumor detection PA technique may ba able to diagnose malignancy of tumors. It has been shown (van Veen *et al.* , 2005) that the oxygen saturation of blood in malignant tissue differs from healthy tissue, and therefore this may be used as an additional criterion for tumor diagnosis. The difference in absorption coefficients of oxygenated and deoxygenated blood in the above mentioned wavelength region (see figure 6.3) allows the mapping of blood oxygenation. For this purpose the imaging procedure should consist of two steps. At first, imaging at a wavelength of equal absorption of

oxygenated and deoxygenated blood is performed. The outcome of the first step is a 3-D map of the absorbed energy. Second, imaging at a wavelength of maximum difference between light absorption of oxygenated and deoxygenated blood (i.e 690 nm, see figure 6.3) has to be performed resulting in a saturation dependent map of absorbed energy. Since at this wavelength deoxygenated blood has a higher absorbance a ratio of the images obtained from first and second steps will highlight regions of predominantly oxygenated blood. Finally, regions with abnormal distribution and increased concentration of deoxygenated blood are highly suspicious to be a malignant tumor host.

Light sources

To reduce the market price of PA imaging systems the utilization of other light sources has to be considered. In this regard, relatively low cost semiconductor sources emitting in the above mentioned wavelength range are of interest. The output energy of the available single laser diodes is in the range of tens of microjoules. This relatively low pulse energy can be compensated combining: 1 - the utilization of laser diode arrays, 2 - the pulse repetition rate of semiconductor can reach a kilohertz range, therefore signal-to-noise ratio can be increased by averaging over larger number of single records, without facing a problem of unacceptably long measurements time. For instance an imager based on laser diode array consisting of 100 elements providing pulses with a peak power of 200 W, pulse duration of 100 ns and duty cycle of 0.1 % should provide the same quality of images as one based on a laser providing pulses with pulse energy of 50mJ and the repetition rate of 10 Hz. The numbers mentioned above present the current state of the art in high power pulsed laser diode technology. Although, at the moment the price of such semiconductor light sources can be still rather high due to the low production numbers and a custom design, this is expected to be significantly reduced by mass production.

References

2004. *Breast cancer. Facts & figures 2003-2004.* Tech. rept. American Cancer Society.

Allen, M.W., Hendi, P., Bassett, L., & Phelps, M.E. 1999. A study on the cost effectiveness of sestamibi scintimammography for the screening women this dense breast for breast cancer. *Breast Cancer Res. Treat.*, **55**, 243–58.

Andreev, V. G., Karabutov, A. A., Solomatin, S. V., Savateeva, E. V., Aleynikov, V., Zhulina, Y. V., Fleming, R. D., & Oraevsky, A. A. 2000. Opto-acoustic tomography of breast cancer with arc-array-transducer. *Pages 36–47 of:* Oraevsky, A. A. (ed), *Biomedical Optoacoustics*. Proc. Soc. Photo-Opt. Instrum. Engg. (SPIE), vol. 3916.

Andreev, V. G., Popov, D. V., Sushko, D. V., Karabutov, A. A., & Oraevsky, A. A. 2001 (June). Inverse Radon transform for optoacoustic imaging. *Pages 119–29 of:* Oraevsky, A. A. (ed), *Biomedical Optoacoustics II*, vol. 4256. Int. Soc. Opt. Engg. (SPIE).

Andreev, V. G., Karabutov, A. A., & Oraevsky, A. A. 2003. Detection of ultrawide-band ultrasound pulses in optoacoustic tomography. *Pages 1383–90 of: IEEE Trans. Ultrason. Ferroelectr. Freq. Control*, vol. 50. IEEE.

Bamber, J. C. *Encyclopedia of Acoustics*. New York: Wiley. Chap. 141, pages 1703–26.

Basset, L. W. 2000. *Imaging the breast. In:*(Holland *et al.* , 2000). Chap. 30F, pages 420–7.

Bertero, M., Miyakawa, M., Boccacci, P., Conte, F., Orikasa, K., & M.Furutani. 2000. Image restoration in chirp-pulse microwave CT (CP-MCT). *IEEE Trans. Biomed. Eng.*, **47**(May), 690–9.

Bolt, R. A., & de Mul, F. F. M. 2002. Goniometric instrument for light scattering measurement of biological tissues and phantoms. *Rev. Sci. Instrum.*, **73**, 2211–3.

Brigham, E. 1999. *Fast Fourier Transform and Its Applications*. Englewood Cliffs, NJ : Prentice Hall.

Carmeliet, P., & Jain, R. K. 2000. Angiogenesis in cancer and other diseases. *Nature*, **407**, 249–57.

Cheong, W. F., Prahl, S. A., & Welch, J. A. 1990. Review of the optical properties of biological tissues. *IEEE J. Quantum Electron.*, **26**, 2166–85.

Clarke, J. 1994. SQUIDS. *Scientific American*, **26**, 291–302.

Colak, S. B., van der Mark, M. B., 't Hooft, G. W., Hoogenraad, J. H., van der Linden, E. S., & Kuijpers, F. A. 1999. Clinical Optical Tomography and NIR Spectroscopy for Breast Cancer Detection. *IEEE J. Select. Topics Quantum Electron.*, **5**, 1143–58.

Cuzick, J., Holland, R., Volker, B., Davies, R., Faupel, M., Fentiman, I.S., Frischbier, H.J., LaMarque, J.L., Merson, M., Sacchini, V., & Veronesi, D.V.U. 1998. Electropotential measurements as a new diagnostic modality for breast cancer. *The Lancet*, **352**(9125), 359–363.

Daviest, S. J., Edwards, C., Taylor, G. S., & Palmer, S. B. 1993. Laser-geberated ultrasound: its properties, mechanisms and multifarious applications. *J. Phys. D: Appl. Phys.*, **26**, 329–40.

de Mul, F. F. M., Koelink, M. H., Kok, M. L., Harmsma, P. J., Greve, J., Graaff, R., & Aarnoudse, J. G. 1995. Laser doppler velocimetry and Monte Carlo simulations on models for blood perfusion in tissue. *Appl. Opt.*, **34**, 6595–611.

Diebold, G. J., & Sun, T. 1994. Properties of photoacoustic waves in one, two and three dimensions. *Acustica*, **80**, 339–351.

Donoho, D. 1992. *De-noising via soft-thresholding.* Technical report 409. Dept. of Statistics, Stanford University.

Donoho, D., & Johnstone, I. 1991. *Minimax estimation via wavelet shrinkage.* Technical report. Dept. of Statistics, Stanford University.

Duck, F. A. 1990. *Physical properties of Tissue: A Comprehensive Reference Book.* London: Academic Press.

Duijm, L.E., Guit, G.L., Zaat, J.O., Koomen, A.R., & Willebrand, D. 1997. Sensitivity, specificity and predictive values of breast imaging in detection of cancer. *Br. J. Cancer*, **76**, 377–81.

Edel, S.L., & Eisen, M.D. 1999. Current imaging modalities for the diagnosis of breast cancer. *Del. Med. J.*, **71**, 377–82.

Esenaliev, R. O., Karabutov, A. A., & Oraevsky, A. A. 1999. Sensitivity of laser optoacoustic imaging in detection of small deeply embedded tumours. *IEEE J. Select. Topics Quantum Electron.*, **5**, 981–988.

Fang, J., Shing, Y., Wiederschain, D., & et al. 2000 (Apr). Matrix metalloproteinase-2 (MMP-2) is required for the switch to the angiogenic phenotype in a novel tumor model. *Pages 3884–9 of: Proc Natl Acad Sci U S A.*, vol. 97.

Fantini, S., Moesta, K. T., Franceschini, M. A., Jess, H., Erdl, H., Gratton, E., Schlag, P. M., & Kaschke, M. 1997. Instrumentation and clinical applications in frequency-domain optical mammography. *Pages 2741–4 of: Proc. 19th Ann. Intl. Conf. IEEE Engg. Med. Biol. Soc.* Piscataway: IEEE Press, for IEEE.

Faupel, M., Vanelb, D., Volker, B., adn I.S. Fentimarf, R. Davie, Holland, R., Lamarqueg, J.L., Sacchinih, V., & Schreer, I. 1997. Electropotential evaluation as a new technique for diagnosing breast lesions. *Eur. J. Radiol.*, **24**, 33–8.

Fear, E.C., Li, Xu, Hagness, S.C., & Stuchly, M.A. 2002. Confocal Microwave Imaging for Breast Cancer Detection: Localization of Tumors in Three Dimensions. *IEEE Transactions on biomedical engineering.*, **49**(8), 812–22.

Folkman, J. 2000. *Cancer Medicine. In:*(Holland *et al.* , 2000). Chap. 9. Tumour angiogenesis, pages 132–52.

Foster, K. R. 1998. Thermographic detection of breast cancer. *IEEE Eng. Med. Biol. Mag.*, **17**, 10–14.

Gambini-Rossano, L. 2002. *Non-invasive biomedical optics: Photoacoustic mammography.* M.Phil. thesis, University of Twente.

Gao, L., Parker, K. J., Lerner, R. M., & Levinson, S. F. 1996. Imaging of the elastic properties of tissue–a review. *Ultrasound Med. Biol.*, **22**(8), 959–77.

Ghosh, N., Mohanty, S. K., Majumder, S. K., & Gupta, P. K. 2001. Measurement of optical properties of normal and malignant human breast tissue. *Appl. Opt.*, **40**, 176–84.

Greenspan, M. 1972. *American Institute of Physics (AIP) Handbook.* 3rd edn. New York: McGraw-Hill. Chap. Acoustic properties of liquids, pages (3)–87.

Grosenick, D., Wabnitz, H., Rinneberg, H. H., Moesta, K. T., & Schlag, P. M. 1999. Development of a time-domain optical mammograph and first *in vivo* applications. *Appl. Opt.*, **38**, 2927–43.

Grosenick, D., Moesta, K.T., Wabnitz, H., Mucke, J., Stroszczynski, C., Macdonald, R., Schlag, P.M., & Rinneberg, H. 2003. Time-domain optical mammography: initial clinical results on detection and characterization of breast tumors. *Appl. Opt*, **42**(16), 3170–86.

Gusev, V. E., & Karabutov, A. A. 1993. *Laser Optoacoustic.* American Institute of Physics, New York.

Hand, D. P., Entwistle, J. D., Maier, R. R. J., Kuhn, A., Greated, C. A., & Jones, J. D. C. 1999. Fibre optic beam delivery system for high peak power laser PIV illumination. *Meas. Sci. Technol.*, **10**, 23945.

Hassan, C. M., & Peppas, N. A. 2000. Structure and applications of poly(vinyl alcohol) hydrogels produced by conventional crosslinking or by freezing/thawing methods. *Adv. Polymer Sci.*, **153**, 37–65.

Hebden, J. C., Veenstra, H., Dehghani, H., Hillman, E. M. C., Schweiger, M., Arridge, S. R., & Delpy, D. T. 2001. Three-dimensional time-resolved optical tomography of a conical breast phantom. *Appl. Opt.*, **40**, 3278–87.

Helbich, T. H. 2000. Contrast-enhanced magnetic resonance imaging of the breast. *Eur. J. Radiol.*, **34**, 208–19.

Hisaka, M., Sugiura, T., & Kawata, S. 2001. Optical cross-sectional imaging with pulse ultrasound wave assistance. *J. Opt. Soc. Am. A*, **18**, 1531–4.

Hoelen, C. G. A. 1998. *3-D photoacoustic tissue imaging.* Ph.D. thesis, University of Twente.

Hoelen, C. G. A., & de Mul, F. F. M. 1999. A new theoretical approach to photoacoustic signal generation. *J. Acoust. Soc. Am.*, **106**, 695–706.

Hoelen, C. G. A., & de Mul, F. F. M. 2000. Image reconstruction for photoacoustic scanning of tissue structures. *Appl. Opt.*, **39**, 5872–83.

Hoelen, C. G. A., de Mul, F. F. M., Pongers, R., & Dekker, A. 1998. Three-dimensional photoacoustic imaging of blood vessels in tissue. *Opt. Lett.*, **23**, 648–50.

Hoelen, C. G. A., Dekker, A., & de Mul, F. F. M. 2001. Detection of photoacoustic transients originating from microstructures in optically diffuse media such as biological tissue. *IEEE Trans. Ultrason. Ferroelect. Freq. Contr.*, **48**, 37–47.

Holland, J. F., Frei III, E., Bast jr., R. C., & Gansler, T. S. (eds). 2000. *Cancer Medicine.* 5 edn. Hamilton: B. C. Decker Inc.

Holmgren, L., OReilly, M.S., & Folkman, J. 1995. Dormancy of micrometastases: balanced proliferation and apoptosis in the presence of angiogenesis suppression. *Nature Med*, **1**, 149–153.

Hyon, S. H., & Ikada, Y. 1987. Porous and transparent poly(vinyl alcohol) gel and method of manufacturing the same. *US Patent*, **4,663,358**.

Hyon, S. H., Cha, W. I., & Ikada, Y. 1989. Preparation of transparent poly(vinyl alcohol) hydrogel. *Polymer Bull.*, **22**, 119–22.

Hyon, S. H., Cha, W. I., Ikada, Y., Kita, M., Ogura, Y., & Honda, Y. 1994. Poly(vinyl alcohol) as soft contact lens material. *J. Biomater. Sci. Polymer Edn.*, **5**, 397–406.

Jacques, S. L., Alter, C. A., & Prahl, S. A. 1987. Angular dependence of HeNe laser light scattering by human dermis. *Lasers Life Sci.*, **1**, 309–33.

Jatoi, I. 1999. Breast cancer screening. *Am. J. Surg.*, **177**, 518–24.

Kane, S. M. 2003. *Introduction to physics in modern medicine.* Taylor & Francis.

Kaufman, A. E. 1998. Volume Visualization: Principles and Advances. *Course Note.*

Kharine, A., Manohar, S., Seeton, R., Kolkman, R. G. M., Bolt, R. A., Steenbergen, W., & de Mul, F. F. M. 2003. Poly(vinyl alcohol) gels for use as tissue phantoms in photoacoustic mammography. *Phys. Med. Biol.*, **48**, 357–70.

Kleiner, M. 1999. More gain, less pain. *New Scientist.*

Kossoff, G. 1976. The Effect of Backing and Matching on the Perfomance of Piezoelectric Ceramic Transducer. *IEEE Trans on Sonic and Ultrasonics*, **SU-13**(1), 20–30.

Kostli, K. P., & Beard, P. C. 2003. Two-Dimensional Photoacoustic Imaging by Use of Fourier-Transform Image Reconstruction and a Detector with an Anisotropic Response. *Appl. Opt.*, **42**(10), 1899–908.

Kostli, K. P., Frenz, M., Bebie, H., & Weber, H. P. 2001. Temporal backward projection of optoacoustic pressure transients using Fourier transform methods. *Phys. Med. Biol.*, **46**, 1863–72.

Kruger, R. A., Kiser Jr., W. L., Reinecke, D. R., & Kruger, G. A. 1999a. Application of thermoacoustic computed tomography to breast imaging. *Pages 426–30 of:* Boone, J. M., & Dobbins III, J. T. (eds), *Physics of Medical Imaging.* Proc. Soc. Photo-Opt. Instrum. Engg. (SPIE), vol. 3659.

Kruger, R. A., Reinecke, D. R., & Kruger, G. A. 1999b. Thermoacoustic computed tomography–technical considerations. *Med. Phys.*, **26**, 1832–7.

Lorenzen, J., Sinkus, R., Lorenzen, M., Dargatz, M., Leussler, C., Roschmann, P., & Adam, G. 2002. MR elastography of the breast:preliminary clinical results. *Rofo Fortschr Geb Rontgenstr Neuen Bildgeb Verfahr*, **174(7)**(Jun), 830–4.

Lubbers, J., & Graaff, R. 1998. A simple and accurate formula for the sound velocity in water. *Ultrasound Med. Biol.*, **24**, 1065–8.

Madsen, E. L., Kelly-Fry, E., & Frank, G. R. 1988. Anthropomorphic phantoms for assessing system used in ultrasound imaging of the compressed breast. *Ultrasound Med. Biol.*, **14**, 183.

Mallat, S. 1989. A theory for multiresolution signal decomposition: the wavelet representation. *IEEE Pattern Anal. and Machine Intell.*, **11**(7), 674–693.

Manohar, S., Kharine, A., Steenbergen, W., & van Leeuwen, T. G. 2004. Photoacoustic mammoscopy laboratory prototype: studies on breast tissue phantoms. *J. Biomed. Opt.*, **9**, 1177–81.

Manohar, S., Kharine, A., van Hespen, J. C. G., Steenbergen, W., & van Leeuwen, T. G. 2005. The Twente Photoacoustic Mammoscope: System overview and performance. *Phys. Med. Biol.*

Mast, T. Douglas. 2000. Empirical relationships between acoustic parameters in human soft tissues. *Acoustics Research Letters Online*, **1**(1), 37–42.

McBride, T.O., Pogue, B. W., Jiang, S., Osterberg, U. L., Paulsen, K. D., & Poplack, S. P. 2001. Initial studies of *in vivo* absorbing and scattering heterogeneity in near-infrared tomographic breast imaging. *Opt. Lett.*, **26**, 822–4.

Meaney, P.M., Fanning, M.W., Li, D., Poplack, S.P., & Paulsen, K. D. 2000. A clinical prototype for active microwave imaging of the breast. *IEEE Trans. Microwave Theory Tech.*, **48**(Nov.), 1841–53.

Merchant, T.E. 1994. MR spectroscopy of the breast. *Magn. Reson. Imaging Clin. N. Am.*, **2**, 691–703.

Molenaar, R. 2005. *Speeding up the Twente Photoacoustic Mammoscope.* M.Phil. thesis, Saxion Hogeschool Enschede Instituut Industriale Technieken en Design Opleiding Technische Natuurkunde.

Moskowitz, M., D'Orsi, C.J., Bartrum, R.J., & Swets, J. 1989. *Breast Cancer Diagnosis by Lightscan. Final report.* Tech. rept. National Cancer Institute.

Moss, M.S. 1999. *Cancer screening: Theory and Practice.* New York: M. Dekker.

Mountford, C., Somorjai, R., Gluch, L., & et al. 2000 (June). *Magnetic Resonance Specroscopy Determines Patology, Vascularisation and Node Status. Era of Hope.* Tech. rept. Department of Defence Breast Cancer Research Programm Meeting, Atlanta, GA.

Mushlin, A. I., Kouides, R. W., & Shapiro, D. E. 1998. Estimating the accuracy of screening mammography: A meta-analysis. *Am. J. Prev. Med.*, **14**, 143–53.

Nambu, M., Watari, T., Sakamoto, T., & Akojima, K. 1990. Method for applying electromagnetic wave and ultrasonic wave therapies. *US Patent*, **4,958,626**.

Ntziachristos, V. M. X. H., & Chance, B. 1998. *Time correlated single photon counting for simultaneous magnetic resonance and nearinfrared mammography.* Tech. rept. Institute of Medicine, Washington, DC.

Oraevsky, A., Andreev, V. G., Karabutov, A. A., Solomatin, S. V., Savateeva, E. V., Fleming, R. D., Gatalica, Z., & Singh, H. 2001. Laser optoacoustic imaging of breast cancer *in vivo. Pages 81–94 of:* Oraevsky, A. A. (ed), *Biomedical Optoacoustics II.* Proc. Soc. Photo-Opt. Instrum. Engg. (SPIE), vol. 4256.

Oraevsky, A. A., Jacques, S. L., & Esenaliev, R. O. 1998. Optoacoustic Imaging for medical diagnosis. *US Patent*, **5,840,023**.

Oraevsky, A. A., Andreev, V. G., Karabutov, A. A., & Esenaliev, R. A. 1999. Two-dimensional opto-acoustic tomography transducer array and image reconstruction algorithm. *Pages 256–67 of:* Jacques, S. L. (ed), *Laser-Tissue Interaction X: Photochemical, Photothermal and Photomechanical.* Proc. SPIE, vol. 3601. SPIE.

Oraevsky, A. A., Savateeva, E. V., Solomatin, S. V., Karabutov, A. A., Andreev, V. G., Gatalica, Z., Khamapirad, T., & Henrichs, P. M. 2002. Optoacoustic imaging of blood for visualization and diagnostics of breast cancer. *Pages 81–94 of:* Oraevsky, A. A. (ed), *Biomedical Optoacoustics III*. Proc. Soc. Photo-Opt. Instrum. Engg. (SPIE), vol. 4618.

Peppas, N. A. 1975. Turbidimetric studies of aqueous poly(vinyl alcohol) solutions. *Makromol. Chem.*, **176**, 3433–40.

Phelps, M.E. 2000. PET: the merging of biology and imaging into molecular imaging. *J Nucl. Med.*, **41**, 661–81.

Pilatou, M.C., van Adrichem, L.N.A., Voogd, N.J., de Mul, F.F.M., & Steenbergena, W. 2003. Analysis of three-dimensional photoacoustic imaging of a vascular tree *in vitro*. *Review of Scientific Instruments*, **74**(10), 4495–9.

Pitas, I. 2000. *Digital image processing algorithms and applications*. John wiley & Sonc, Inc.

Plewes, D.B., Bishop, J., Samani, A., & Sciarretta, J. 2000. Visualization and quantification of breast cancer biomechanical properties with magnetic resonance elastography. *Phys. Med. Biol.*, **45**, 15911610.

Pogue, B. W., Testorf, M., McBride, T., Osterberg, U., & Paulsen, K. 1997. Instrumentation and design of a frequency-domain diffuse optical tomography imager for breast cancer detection. *Opt. Express*, **1**, 391403.

Pogue, B. W., Poplack, S. P., McBride, T. O., Wells, W. A., Osterman, K. S., Osterberg, U. L., & Paulsen, K. D. 2001. Quantitative hemoglobin tomography with diffuse near-infrared spectroscopy: pilot results in the breast. *Radiology*, **218**, 261.

Pommert, Andreas, & Hohne, Karl Heinz. 2002. Evaluation of Image Quality in Medical Volume Visualization: The State of the Art. *Medical Image Computing and Computer- Assisted Intervention, Proc. MICCAI 2002, Part II, Lecture Notes in Computer Science 2489*, 598–605.

Pravdin, A. B., Chernova, S. P., Papazoglou, T. G., & Tuchin, V. V. 2002. Tissue phantoms. *Chap. 5, pages 311–52 of:* Tuchin, V. V. (ed), *Handbook of Optical Biomedical Diagnostics*. Bellingham: SPIE Press: Soc. Photo-Opt. Instrum. Engg. (SPIE).

Profio, E. A. 1989. Light transport in tissue. *Applied Optics*, **28**, 2216–22.

Ristic, V. M. 1983. *Principles of Acoustic Devices*. New York: J. Wiley & Sons. Chap. 5.

Sabel, M., & Aichinger, H. 1996. Recent developments in breast imaging. *Phys. Med. Biol.*, **41**, 315–68.

Sarvazyan, A. 1995. Biophysical bases of elasticity imaging. *Acoust. Imag.*, **21**, 223–40.

Scruby, C. B., & Drain, L. E. 1990. *Laser Ultrasonics; Techniques and Apllications*.

Sigrist, M. W. 1986. Laser generation if acoustic waves in liquids and gases. *J. Appl. Phys.*, **60**, R83–R121.

Sigrist, M. W., & Kneubühl, F. K. 1978. Laser-generated stress waves in liquids. *J. Acoust. Soc. Am.*, **64**, 1652–63.

Sparrow, C. M. 1916. *Astrophys. J.*, **44**(76).

Spinelli, L., Torricelli, A., Pifferi, A., Taroni, P., Danesini, G. M., & Cubeddu, R. 2004. Bulk optical properties and tissue components in the female breast from multiwavelength time-resolved optical mammography. *J. Biomed. Optics*, **9**, 1137–42.

Steins, C.M. 1981. Estimation of the mean of a multivariate normal distribution. *Annals of Statistics*, **9**, 1135–1151.

Sterenborg, H.J.C.M., Menke, M., Bartels, C.C.M., Tilanus-Linthorst, M.M.A., Manohar, S., Kharine, A., & W.Steenbergen. 2004. *Pilot study if photoacoustic mammography by examinations of patients with symptomatic breast lesions.* Clinical protocol. Accepted by medical athecal committee of Daniel den Hoed oncologische Centrum. Rotterdam.

Stuntz, M.E., Khalkhali, I., Kakuda, J.T., Klein, S.R., & Vargas, H.I. 1999. Scitnimammography. *Seminar In Breast Disease*, **2**, 97–106.

Suzuki, K., Yamashita, Y., Ohta, K., Kaneko, M., Yoshida, M., & Chance, B. 1996. Quantitative measurement of optical parameters in normal breasts using time-resolved spectroscopy: *in vivo* results of 30 Japanese women. *J. Biomed. Opt.*, **1**, 330–4.

Teolis, A. 1998. *Computational signal processing with wavelet.* Hamilton Printing, Rensselear, NY.

Tromberg, B. J., Shah, N., Lanning, R., Cerussi, A., Espinoza, J., Pham, T., Svaasand, L., & Butler, J. 2000. Non-invasive *in vivo* characterization of breast tumours using photon migration spectroscopy. *Neoplasia*, **2**, 26–40.

Tuchin, V. V. 2000. Tissue Optics: Light Scattering Methods and Instruments for Medical Diagnosis. *Page 42 of:* O'Shea, D. C. (ed), *Tutorial Texts in Optical Engineering.* Intl. Soc. Opt. Engg., no. TT38. Bellingham, USA: SPIE Press: Soc. Photo-Opt. Instrum. Engg.

van Staveren, H. J., Moes, C. J. M., van Marle, J., Prahl, S. A., & van Gemert, M. J. C. 1991. Light scattering in Intralipid-10% in the wavelength range of 400-1100 nm. *Appl. Opt.*, **30**, 4507–14.

van Veen, R. L.P., Amelink, A., Menke-Pluymers, M., van der Pol, C., & Sterenborg, H. J.C.M. 2005. Optical biopsy of breast tissue using differential path-length spectroscopy. *Phys. Med. Biol.*, **in print**.

Verdaasdonk, R. M., & van Swol, C. F. P. 1997. Laser light delivery systems for medical applications. *Phys. Med. Biol.*, **42**, 86994.

Visser, O., Coebergh, J. W. W., van Dijck, J. A. A. A. M., & S. Siesling (editors). 2002 (July). *Incidence of cancer in the Netherlands 1998.* Tenth report of the Netherlands Cancer Registry, Vereniging van Integrale Kankercentra, Utrecht.

Visser, O., Siesling, S., & van Dijck (editors), J.A.A.A.M. 2003 (Dec.). *Incidence of cancer in the Netherlands 1999/2000.* Eleventh report of the Netherlands Cancer Registry, Vereniging van Integrale Kankercentra, Utrecht.

Wang, L., & Ku, G. 1998. Frequency-swept ultrasound-modulated optical tomography of scattering media. *Opt. Lett.*, **23**, 975–7.

Warren, S.L. 1930. *Am . J. Roentgenol. Rad. Ther.*, **24**, 113–24.

Wen, H., Shah, J., & Blaban, R.S. 1998. Hall efect imaging. *Pages 119–24 of: IEEE Trans. Biomed. Eng.*, vol. 45.

Xu, M., & Wang, L. V. 2003. Analytic explanation of spatial resolution related to bandwidth and detector aperture size in thermoacoustic or photoacoustic reconstruction. *Phys. Rev. E*, **67**, 1–15.

Xu, M., Xu, Y., & Wang, L. H. 2003. Time-Domain Reconstruction Algorithms and Numerical Simulations for Thermoacoustic Tomography in Various Geometries. *Pages 1086–99 of: IEEE Transactions on Biomedical Engineering*, vol. 50.

Xu, Y., Xu, M., & Wang, L.-H. V. 2002. Exact Frequency-Domain Reconstruction for Thermoacoustic TomographyII: Cylindrical Geometry. *IEEE Transaction on Medical Imaging*, **21**(7).

Zhu, Q., Sullivan, D., Chance, B., & Dambro, T. 1999. Combined ultrasound and near infrared diffused light imaging in a test object. *IEEE Trans. Ultrason. Ferroelect. Freq. Contr.*, **46**, 665–78.

Ziewacz, J.T., Neumann, D.P., & Weiner, R.E. 1999. The difficult breast. *Surg. Oncol. Clin. N. Am.*, **8**, 17–33.

Publications and conference participation

First author and equal contribution publications

A. Kharine, S. Manohar, R. Seeton, R.G.M. Kolkman, R.A. Bolt, W. Steenbergen and F.F.M. de Mul, "Poly(vinyl alcohol) gels for use as tissue phantoms for photoacoustic mammography", *Phys. Med. Biol.* **48**, 357-70 (2003).

S. Manohar, A. Kharine, J.C.G. van Hespen, W. Steenbergen and T.G. van Leeuwen, "The Twente Photoacoustic Mammoscope: System overview and performance" *Phys. Med. Biol.* In press (2005).

Coauthor publications

S. Manohar, A. Kharine, J. G. C. van Hespen, W. Steenbergen, Ton. G. C. van Leeuwen, "Photoacoustic mammography laboratory prototype: Imaging of breast tissue phantoms", *J. Biomed. Opt.* (Special Issue on "Optics in Breast Cancer") **9**, 1172-81 (2004).

Conference proceedings

A. Kharine, S. Manohar and W. Steenbergen, "Three-dimensional phantom Imaging for Photoacoustic Mammography", In Vargas H. (editor) International Conferences on Photoacoustic and Photothermal Phenomena (13th ICPPP) (Rio de Janeiro, Brazil) *J. Phys. IV,* In press. (2004).

S. Manohar, A. Kharine, J. G. C. van Hespen, W. Steenbergen, F. F. M. de Mul, Ton. G. C. van Leeuwen, "Photoacoustic imaging of embedded inhomogeneities in breast tissue phantoms", In Oraevsky A. A. (editor) *Biomedical Optoacoustics IV* (San Jose, USA) Proc. Soc. Photo-Opt. Instrum. Engg. (SPIE) **4960**, 64-75 (2003).

S. Manohar, A. Kharine, W. Steenbergen, Ton. G. C. van Leeuwen, Three-dimensional photoacoustic imaging of breast tissue phantoms", In Shcherbakov I. (editor) International Conference on Advanced Laser Technologies (ALT 03) (Cranfield, UK.) Proc. Soc. Photo-Opt. Instrum. Engg. (SPIE) **5486**,

247-251 (2004).

A. Kharine, S. Manohar, W. Steenbergen and F.F.M de Mul, "Photoacoustic technique for breast cancer tumor detection", Annual conference of institute of Bio Medical Engineering (iBME), In Proc, (Papendal, The Netherlands), 75-8 (2001).

A. Kharine, S. Manohar, W. Steenbergen and F.F.M de Mul, "Photoacoustic technique for breast tumor detection", Annual conference of institute of Bio Medical Engineering (iBME), In Proc, (Papendal, The Netherlands), 61-3 (2002).

A. Kharine, S. Manohar and W. Steenbergen, "Photoacoustic breast cancer detection: imaging of inhomogeneities in a phantom", Annual conference of institute of Bio Medical Engineering (iBME), In Proc, (Papendal, The Netherlands), 166-8 (2003).

A. Kharine, S. Manohar and W. Steenbergen, "Photoacoustic mammography. Study of imaging quality", Annual conference of institute of Bio Medical Engineering (iBME), In Proc, (Papendal, The Netherlands), 75-8 (2004).

Oral and poster conference contributions

13th International Conference on Photoacoustic and Photothermal Phenomena, July 3-8, 2004, Brazil. Oral presentation: "Three-dimensional phantom Imaging for Photoacoustic Mammography".

Gordon Research Conference on Photoacoustic and Photothermal Phenomena, June 8-13, 2003, US. Poster presentation: "Photoacoustic Breast cancer detection. Imaging of inhomogeneities in Phantom".

"Biophotonics" workshop, October 18-20, 2002, Crete, Greece. Poster presentation "Photoacoustic breast cancer detection".

Acknowledgements

The fact that I am writing this last page means that the concept of my thesis has been approved by the committee and I will be admitted for the public defence. I suppose it is high time to mention those without whose contributions and support this would have hardly become a reality. In particular, I cordially acknowledge:

Prof. Jan Greve who opened the door of the Biophysical Technique Group for me and gave me the opportunity to conduct this PhD research in the University of Twente.

My daily supervisor Wiendelt Steenbergen who picked me up behind that door and guided throughout all these four years. Wiendelt, I appreciate your constructive critics and remarks, your supervisory tact and unbelievable patience to correct my writing. . I think this page is the first and the only one I have written for these four years which has not been reviewed by you before becoming public :)

I do not forget Frits de Mull who started this project in our lab and really helped me to get in without wasting much time.

My promoter prof. Ton van Leeuwen for supporting me in this last and most important moment. In Russia we say “last step is the most difficult one". Prof. Vinod Subramaniam for the encouraging input at the final stages of our project and, frankly speaking, quite unexpected help in the preparation of my thesis. I do appreciate it a lot.

However, each of us knows that being guided and supervised is not more than only the top of the scientific life iceberg. The underwater part of this iceberg is the day-by-day laboratory routine. And all the best and worst moments of this I shared with my officemate and project colleague - Srirang Manohar. I wish everybody had such an open-minded neighbour and such an experienced and creative colleague working like a dog. Srirang, you are the person whom I actually owe this thesis.

A lot of our ideas would have existed in our minds but never on the experimental table without Johan van Hespen’s technical support. He did things in the best way before our clumsy hands could spoil them :). However some times we were faster :(. I thank Theo Pünt and Hans de Boer for the implementation of “heavy metal"part of PAM.

All present and former members of BMO group for their everyday support, ideas and help. In particular I should mention Roy Kolkman who ever knew where to find “these things". And all members of BFT and later BPE for pleasant, relaxing but never boring atmosphere in our group, and for coffee break talk about everything in- and beyond- this world.

Special thanks to our secretary Sylvia Winters for the infinite help and assistance. Sylvia, you saved a lot of my time and nerve cells which I would definitely have lost “fighting with paper"without you.

I would like to take this opportunity to express my thanks to all my Russian friends and colleagues for making me feel at home even so far from my motherland. I do not put the names because it would take too much space, but you know whom I am writing about.

И наконец, я хочу поблагодарить мою семью. Дорогие мои, без вашей любви, терпения и поддержки, я никогда не достиг бы всего того, что имею сейчас.